Metal Additive Manufacturing of Ti6Al4V from Blended Elemental Powders

LEKHETHO AMBITION RAMOSENA

Dissertation submitted in fulfilment of the requirements for the degree:

MASTER OF ENGINEERING

in

MECHANICAL ENGINEERING

in the

Department of Mechanical and Mechatronics Engineering

Faculty of Engineering, Built Environment, and Information Technology

at

Central University of Technology, Free State

Supervisor: Dr T. C. Dzogbewu, D-Eng, Pr Sci Nat

Co-supervisor: Prof. W. B. du Preez, PhD, Pr Sci Nat

BLOEMFONTEIN

December 2024

Declaration of independent work

DECLARATION WITH REGARD TO

INDEPENDENT WORK

I, Lekhetho Ambition Ramosena, identity number _____ and student number _____, hereby declare that this research project submitted to the Central University of Technology, Free State, for the degree MASTER OF ENGINEERING in MECHANICAL ENGINEERING, is my own original work, complies with the Code of Academic Integrity, as well as other relevant policies, procedures, rules and regulations of Central University of Technology, Free State, and has not been submitted before to any institution by myself or any other person in fulfilment (or partial fulfilment) of the requirements for the attainment of any qualification.

_____ **2024/12/12**

SIGNATURE OF STUDENT **DATE**

Dedicated to the memory of my father, Ramosena Kingsley Ramosena "Moetapele", and the birth of my daughter, Rethabile Leseli Ramosena. Kingsley, thank you for always believing in me, even when I had a hard time believing in myself….

Acknowledgments

Praise be to the God and Father of our Lord Jesus Christ!

I would like to thank my mother, Tlalane and my two siblings, Polotso and Mosena Ramosena for their unwavering support and encouragement throughout the duration of this study.

To my supervisors, Prof. W. B. du Preez and Dr T. C. Dzogbewu, thank you very much for your guidance. I am extremely appreciative of the patience that you had when it comes to me and my growth as a human being. This was a tough journey, but you never lost faith in me and my capabilities. Dr Thywill, thank you for showing care and always being a phone call away. Prof. Willie, you have taught me to always be ethical in everything that I seek to do and for that I thank you, and for the wisdom that I have gained from working with you. I am indeed fortunate to have worked with you. I would also like to acknowledge and express my gratitude to Dr Maina Maringa, you have been a listening ear in times of distress, providing nuggets of wisdom with every visit to your office and home. I wish to thank the Centre for Rapid Prototyping and Manufacturing for producing the experimental samples used for research in this study. Furthermore, I would like to thank Dave Hudson-Lamb and the South African Nuclear Energy Corporation as an entity for the compositional analysis of the produced samples. The Geology department of the University of the Free State through the assistance of Megan Purchase is also acknowledged for allowing me to use their scanning electron microscope for this research. Lastly, I would like to acknowledge the Collaborative Program in Additive Manufacturing, Contract no. CSIR-NLC-CPAM-21-MOA-CUT-01 for their financial support throughout this study.

A special thanks to my daughter, Rethabile Leseli Ramosena. Your presence in my life has encouraged me to work harder.

~Sabela malibizwi lgama lakho~

Abstract

Metal Additive Manufacturing (MAM) processes, such as the Direct Metal Laser Sintering (DMLS) process, have conventionally employed pre-alloyed (PA) metal powder to produce parts with excellent mechanical properties. In a PA powder feedstock, each individual powder particle has the target alloy composition that is required in the final part, therefore producing a part with a good elemental homogeneity, which in turn results in a part that possesses the best mechanical properties that the target alloy has to offer. The production of these PA powders involves a chain of processes, including conventional and modern atomisation processes, which often result in expensive PA powders. Since the nature of the DMLS process entails re-melting these PA powders to solidify them again into the bulk of the part being built, an alternative approach is the use of blended elemental (BE) powders. The term BE can be used in the context of any application wherein a powder blend consisting of purely elemental powders or of elemental and pre-alloyed (master alloy) powders is employed as feedstock. In this approach, in situ alloying of BE powders during DMLS occurs with the consequent elimination of the pre-alloying process, thus resulting in a more cost-effective production route.

The Ti6Al4V alloy is widely known as the workhorse of the titanium industry due to its unique combination of properties, which are high strength, lightweight and corrosion resistance [1]. This alloy is mostly used in medical and aerospace applications where its high cost can be justified by the benefits that the alloy offers. The production of parts in the DMLS process using PA Ti6Al4V powder as feedstock results in expensive parts, which makes them unjustifiable for use in common engineering applications. In comparison, the production of parts in the DMLS process through BE Ti6Al4V entails obtaining elemental powders of titanium (Ti), aluminium (Al) and vanadium (V), blending them into the correct ratio and then using them as feedstock for DMLS. This route has the potential to lower the cost of Ti6Al4V parts (and those of other Ti alloys) produced through the DMLS process.

Therefore, the aim of this study was to determine the feasibility of using the BE approach to produce the Ti6Al4V alloy through the DMLS process. To achieve this aim, a gradual approach, which entails first producing the Ti6Al4V alloy from the BE approach using a powder blend consisting of elemental Ti and Al-V master-alloy (MA) powders, was employed. This gradual approach was used in an attempt to reduce the complexity of the interaction between the DMLS system and the elemental powder blend to allow for insight into further optimisation and customisation of the DMLS process parameters and BE powders, thus paving the way for the production of the Ti6Al4V from the purely elemental powder blend. A hierarchal approach was employed to determine the feasibility of using these powder blends to produce high-quality Ti6Al4V parts [2]. Firstly, single tracks were produced to determine the process parameters that could be used to produce optimum single tracks (laser power, scanning speed and layer thickness). Secondly, these process parameters were then used to produce single and double layers to determine the optimum hatch distance. Lastly, once a full set of process parameters had been obtained from the range of process parameters investigated, 3D parts were then produced. These 3D parts were analysed to determine the type of microstructure produced and their mechanical properties (tensile tests). The results obtained from the two powder blends used in this study were compared with each other and with the known test values obtained from the wrought and DMLS PA production routes.

It was found that the as-built (AB) microstructures of the produced Ti6Al4V parts were similar to those of Ti6Al4V parts produced from the PA route. The mechanical properties of the parts produced from the blended powders were generally superior to the mechanical properties specified in the ASTM F2924-14 standard, which is intended to ensure the production of additively manufactured Ti6Al4V parts with mechanical properties that are comparable to the forged and wrought Ti6Al4V parts. The use of the Al-V MA powder in the powder blend generally offered a greater compositional control during in-situ alloying, thus yielding parts with a chemical composition that was closer to the intended chemical composition in comparison to that of the parts produced from the purely elemental powder blend. The results obtained suggest that in-situ alloying in the DMLS process can be employed to

produce high-quality Ti6Al4V parts from powder blends consisting of a combination of elemental and MA powders or purely elemental powders.

Publications Emanating from This Study

Peer-reviewed Journal Paper:

1. **Ramosena, L.A., Dzogbewu, T.C., Du Preez, W.B.** 2022. Direct Metal Laser Sintering of the Ti6Al4V alloy from a powder blend, *Materials. 15* (8193), pp. 1–20. https://www.mdpi.com/1996-1944/15/22/8193

Peer-reviewed Conference Papers:

1. **L.A. Ramosena, B.S. Parker, T.C. Dzogbewu, W.B. Du Preez, D.B. Blaine**. "Optimum Process Parameters for DMLS In-situ Alloying of a Ti-10(60Al40V) Powder Blend", in Pre-Conference Seminar: Design for Additive Manufacturing of Titanium Parts, Bloemfontein, 2019, pp. 78–93. https://site.rapdasa.org/past-proceedings-2019/rapdasa-2019-proceedings/78-ramosena/
2. **L.A. Ramosena, T.C. Dzogbewu, W.B. Du Preez.** "Direct Metal Laser Sintering Production of Ti6Al4V Parts from a Purely Elemental Powder Blend", in the 22nd Annual International RAPDASA Conference, Pretoria, 2021: pp. 51–62. https://site.rapdasa.org/wp-content/uploads/2022/07/2021-RAPDASA-PROCEEDINGS-ISBN-978-0-6397-0111-0.pdf

Table of Contents

List of Tables

List of Figures

Nomenclature, Abbreviations and Symbols

3D	Three Dimensional
AM	Additive Manufacturing
ASTM	American Society for Testing and Materials
CAD	Computer-Aided Design
CRPM	Centre for Rapid Prototyping and Manufacturing
CSIR	Council for Scientific and Industrial Research
CT	Computer Tomography
CUT	Central University of Technology, Free State
DMLS	Direct Metal Laser Sintering
EOS	Electro-Optical Systems GmbH
ELI	Extra-Low Interstitial
NECSA	South African Nuclear Energy Corporation
nm	Nanometre
PSD	Particle Size Distribution
SEM	Scanning Electron Microscope
STL	Standard Tessellation Language

SU	Stellenbosch University
UTS	Ultimate Tensile Strength
YS	Yield Strength
μm	Micrometre
wt.	Weight
σ	Stress
ε	Elongation at break
E	Young's Modulus

Chapter 1 Introduction

1.1 Background

Additive Manufacturing (AM) is a relatively new manufacturing technology that has the potential to replace the known conventional methods of manufacturing, such as forging and casting [3] [1]. The American Society of Testing and Materials (ASTM) has defined AM as “the process of joining materials to make objects from three-dimensional (3D) model data, usually layer upon layer, as opposed to subtractive manufacturing methodologies” [4]. Based on this definition, it can be said that any process that joins materials layer by layer until the part is produced can be classified as an AM process.

AM first surfaced in the 1980s with a Rapid Prototyping (RP) process called Stereolithography (SL) from 3D systems. The RP process was initially intended to produce prototypes of final parts [5]. During the period between the introduction of SL and the year 2014, AM technology grew by 26.3% annually with the development of other AM processes. During this growth period, the demand and curiosity-driven intent to use AM for the manufacturing of fully functional parts increased from 3.9% in 2003 to 42.6% in 2014 [5]. It was due to this increase in the manufacturing of fully functional final parts that this technology evolved from RP to AM.

Ti6Al4V is an alloy of titanium, aluminium and vanadium containing 6 wt.% Al and 4 wt.% V, with Al acting as the α stabiliser and V acting as the β stabiliser. Due to its contents, this alloy is referred to as an alpha-beta (α+β) alloy, which means that it consists of α and β phases at room temperature. Ti6Al4V is known as the “workhorse” of the titanium industry because it is by far the most common Ti alloy of the 21st century [1]. Many Ti alloys have been invented, but none of them has seen such significant commercial use as the Ti6Al4V alloy. Ti6Al4V is unique in that it combines attractive properties such as high strength, lightweight, and corrosion resistance, which make it a desirable material for applications in many industries [6].

Conventionally, pre-alloyed (PA) powder of Ti6Al4V has been the main feedstock used for AM processes, mainly because it simplifies the AM production of parts while providing the required alloy composition with good mechanical properties and high

part quality [7]. In a PA powder feedstock, each individual powder particle has the composition of the desired alloy composition of the final part. Due to the chain of processes involved in producing these powders [8], they result in an expensive alloy, which then limits the application of the Ti6Al4V alloy mainly to high-value parts in industries such as aerospace, motorsports and modern medicine where its good combination of properties and characteristics justify its high price [9]. To pave the way for this alloy to be used to produce parts for less critical applications, such as brackets for boat components in marine applications and valves and fittings for industrial applications, different methods of production need to be explored in an attempt to identify new types of cost-effective powder feedstock, thereby expanding the range of powder materials that can be used to produce this alloy [9].

The development of new AM materials has been identified as a high-priority, key focus area in the South African (SA) Additive Manufacturing Strategy (Figure 1).

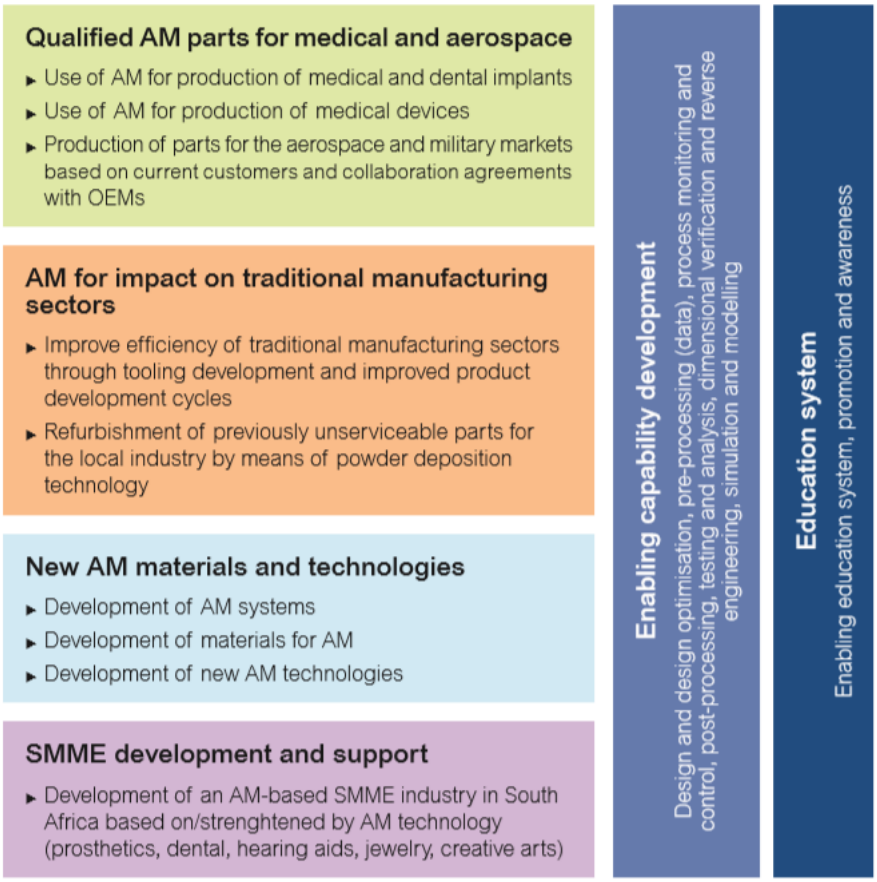

Figure 1. The South African Additive Manufacturing Strategy focus areas [10]

This strategy aimed to unlock the true potential of SA's AM industry by taking advantage of South Africa's natural resources. Utilising the natural resources that SA has to offer, the development of new AM materials will have a good impact on SA's economy by eliminating the need to import any material from other countries at exorbitant prices, as has been the case with the Ti metal [10].

To contribute to the above-mentioned body of knowledge, this study focused on developing alternative methods of producing Ti6Al4V alloy parts by AM using raw materials, thereby demonstrating the competency to utilize locally sourced elemental Ti powder for AM. The initial approach towards applying this proposed alternative method was the production of the Ti6Al4V alloy from a powder blend consisting of commercially pure (CP) Ti powder and Al-V master alloy (MA) powders blended to the ratio of 90 Ti: 10 MA (wt.%). Since the Al-V MA powder is essentially a PA powder, and the behaviour of PA powders in AM systems has been thoroughly investigated and documented, this approach would provide insight into the behaviour of elemental CP Ti in AM systems, thus paving the way to the subsequent proposed Ti6Al4V production approach. This approach entailed employing BE powders (Ti, Al, V) as feedstock in the AM (laser powder bed fusion; LPBF) process. In a BE powder blend, each individual powder particle has an elemental composition [11]. These powders were blended to the correct ratio of 90% Ti: 6% Al: 4% V (wt.%) to form a Ti6Al4V powder blend which was then used as AM powder feedstock.

1.2 Problem statement

South Africa (SA) has huge reserves of the Ti-bearing metal. Ti is mined from the ore as a part of minerals such as rutile (TiO_2) and ilmenite ($FeTiO_3$) and exported without being extracted from the mineral. The extracted Ti metal or its alloys are then imported at a high price when there is a need to produce products from this metal or its alloys. For this reason, the Council for Scientific and Industrial Research (CSIR) in Pretoria, South Africa, has developed a process of producing Ti powder directly from titanium tetrachloride ($TiCl_4$) as feedstock. Through their Titanium Pilot Plant, CSIR tried to prove that their process could be upscaled to a full commercial level [12]. This was an attempt to bridge the gap between the mining of the mineral and the production of Ti products by producing the powder locally. It was anticipated that the locally produced Ti powder would be more economical compared to the currently

imported Ti powder. Once this powder production process has been commercialised, SA will benefit by producing low-cost Ti powder that can be utilised for various manufacturing processes and exported globally. The progression of this study was intended to lead to the Ti powder being used in different MAM processes once it had been successfully commercialised by the CSIR [12].

Research into more economical powder feedstock that can be utilised in AM technologies is required to enhance the advantages offered by these processes. As already stated in section 1.1, using BE powders to produce parts in the LPBF process would lower the cost of the feedstock material, thus lowering the overall cost of the produced part. Although it is easier to obtain homogeneous and fine microstructures using the PA approach, the PA powders have a high cost due to the chain of processes involved in the production of these powders [9]. The required alloy composition is first obtained through the conventional production route in the form of a solid metal, which is then processed back into powder through a gas atomisation process, which adds additional cost to the production process [13].

While it is an attractive alternative, the approach of producing the Ti6Al4V alloy from elemental powders through the DMLS process has not been technically proven to produce a homogeneous alloy with properties that are comparable to those produced through the PA and wrought metal approaches. If this study could demonstrate the capability of the DMLS process to produce high-quality products from BE powder, an opportunity to use the locally produced Ti powder would present itself, benefiting the local manufacturing industry. If the powder cannot be sourced locally, importing elemental powders will still be more cost-effective than importing PA powders.

1.3 Aim of the study

The aim of this study was to evaluate the feasibility of employing a powder blend consisting of a combination of elemental Ti and Al-V MA powders and a powder blend consisting of purely elemental Ti, Al, and V powders as feedstock for producing Ti6Al4V parts through the DMLS process.

1.4 Objectives of the study

The objectives of this study were to:

1. Determine the optimum process parameters that could be used to manufacture the Ti6Al4V alloy from BE powders through the DMLS process using the EOSINT M280 machine.

2. Study the microstructure and mechanical properties of the Ti6Al4V samples manufactured from BE powders through the DMLS process using the EOSINT M280 machine.
3. Compare the mechanical properties and the microstructure of the Ti6Al4V alloy samples manufactured by the DMLS process using the EOSINT M280 machine with those from conventional wrought material methods and those obtained using PA powder.

1.5 Delimitations

This study was a collaborative study between Central University of Technology, Free State (CUT) and Stellenbosch University (SU). An agreement was reached between the two universities that SU would focus on powder blending while CUT would focus on the AM aspect of the collaborative study. Therefore, this study solely focused on producing and analysing the parts produced from the powder blends received from SU.

1.6 Layout of the dissertation

Chapter 1 provides the background behind the conceptualization of this study. Furthermore, the aims, objectives and limitations of the study are clearly defined in this chapter. The literature regarding MAM, the Ti6Al4V alloy, the conventional AM PA Ti6Al4V powder feedstock production and the production of the proposed AM BE Ti6Al4V powder feedstock, and a comparison thereof is presented in Chapter 2. In Chapter 3, the methodology that was employed to achieve the aims and objectives of the study is reported. Chapter 4 presents the results obtained from the range of analyses conducted on the produced samples. In Chapter 5, a report of the extent to which the aims and objectives that were set out in the study were achieved, together

with recommendations for future work, is provided. A schematic illustrating the layout of the study is shown in Figure 2.

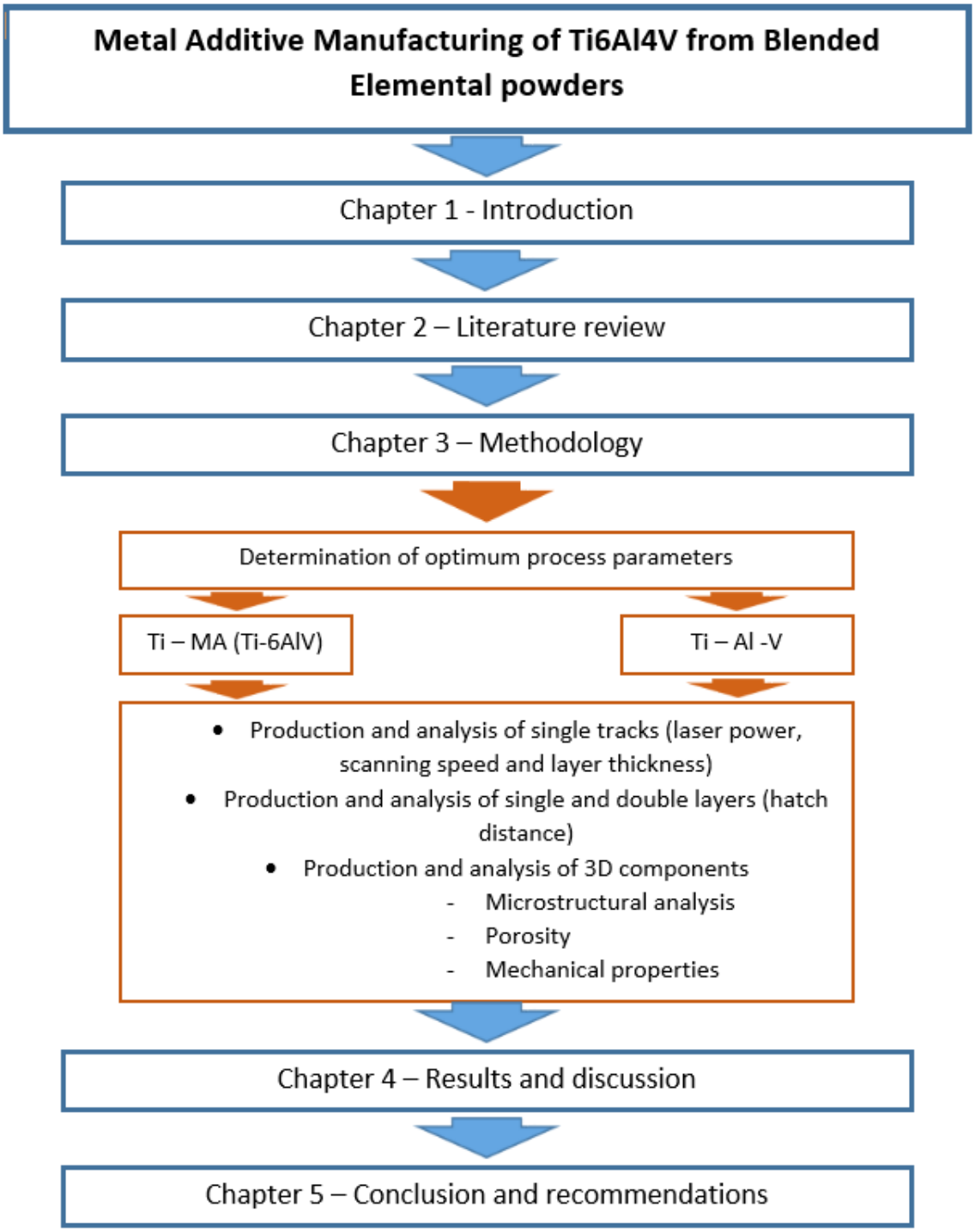

Figure 2. Schematic of the layout of the dissertation

1.7 Summary

In this chapter, the background and problem statement that clearly outlined the need to develop an alternative approach to produce the Ti6Al4V alloy through the DMLS process was presented. This then led to the development and presentation of the aim and specific objectives of this research study. The delimitations and the proposed layout of the study were clarified and presented. The following chapter focuses on the literature review specific to the DMLS process, the Ti6Al4V alloy, the conventional DMLS Ti6Al4V production approach and the proposed alternative Ti6Al4V alloy production approach.

Chapter 2 Literature review

2.1 Introduction

The preceding chapter focused on the need to develop an alternative approach to produce the Ti6Al4V alloy through the DMLS process. BE powder metallurgy (PM) in conjunction with in-situ alloying can be used to produce the Ti6Al4V alloy through the DMLS process. In this chapter, a literature review on AM with a specific focus on the DMLS process, the Ti6Al4V alloy, the PA DMLS Ti6Al4V production approach, and the proposed BE powder in-situ Ti6Al4V alloy production approach is presented.

2.2 Additive Manufacturing

Additive Manufacturing (AM) is a relatively new manufacturing technology that has the potential to replace the conventional methods of manufacturing [14]. Since its inception, AM technology has been given many names, such as rapid prototyping (RP), additive layer manufacturing (ALM), direct manufacturing, solid freeform fabrication (SFF) and on-demand manufacturing [3], [5]. These names were all derived from the additive technique that this manufacturing process utilises. Therefore, they essentially refer to the same process. To alleviate the confusion that would arise from the development of multiple names for one process, the ASTM developed a standard which stated that any process that produces near-net-shape parts in a layer-wise fashion can be considered an AM process [4].

In the 1890s, people already had an idea of producing products using a layer-by-layer approach. However, the individual layers were manufactured separately and then bonded together by glue or welding to form the required part [15]. This approach did not improve the manufacturing sector by a great margin since the conventional subtractive manufacturing and fabrication processes still had to be employed during the production of the layered part. The first breakthrough in AM came in the years between 1984 and 1987 when Charles Hull of 3D Systems invented and patented the stereolithography process [5], [16]. This process was commercialised in the early 1990s through the production of the Stereolithography Apparatus (SLA) which became the first commercial AM machine in the world. In 1989, MIT patented the 3D printing (3DP) process, and the patent was awarded in 1993. The early 1990s saw the development of AM processes such as Selective Laser Sintering (SLS; 3D

Systems, 1990), Laser Engineered Net Shaping (LENS; 1990), Fused Deposition Modelling (FDM; Stratasys, 1992), Material Jetting (Objet, late 1990s) and Laminated Object Manufacturing (LOM; Helisys, early 1990s). In the early 2000s, Electron Beam Melting (EBM) was developed and many improvements on the existing technologies by different manufacturers emerged. These improvements were aimed at particularly accommodating the production of metal parts and to introduce a range of new materials [3], [5]. Since AM proved to be a developing manufacturing technology with potential, the ASTM established committee F42 in 2009, the first AM standards committee to develop AM standards. In 2011, the University of Southampton produced the first 3D-printed aircraft, thus demonstrating the development and capabilities of the AM process [3].

The past 30 years have seen the development of many different types of AM systems that operate on the same principle to produce parts [14]. These systems share some general advantages and disadvantages because of their process similarities. AM processes have advantages such as reducing the cost involved in the production of parts. This cost reduction is a result of the decreased necessity to employ the conventional machining operations required to produce a part [17]. Many parts with complex geometry can be produced with ease using AM technologies. The material-to-part efficiency is increased by the additive nature of this manufacturing process because material wastage is limited. The part production time can be reduced rapidly due to the iterative nature of this process that allows for timely design modifications, thereby minimising the lead time between model modification and final part production [18].

AM processes were initially developed as rapid prototyping technologies which could be used to produce prototype parts that can be assessed to detect defects and design flaws before the real product can be manufactured. Consequently, some industries still consider AM as just a prototyping tool, not as a method of manufacturing fully functional parts. The current disadvantages of the AM process include a limitation in the range of materials that can be used in AM processes. Some of the materials that are available for AM and the atomisation processes required to produce these materials are expensive. Due to the size of the machines, the product size is limited to the size of the build platform [5], [14], [15].

Since AM processes were developed at an alarming rate, with some sharing similarities with each other, a need was identified to classify these processes to ensure that the generic processes and their definitions could be standardised instead of defining every individual commercial variation of the process. For this reason, the ASTM F42 committee developed the ASTM 2792 standard for grouping similar AM technologies [4]. The AM processes were then classified into seven distinct standard categories in which AM technologies were grouped (Figure 3). These categories are Powder Bed Fusion, Vat Polymerization, Material Extrusion, Material Jetting, Binder Jetting, Directed Energy Deposition, and Sheet Lamination [4], [19].

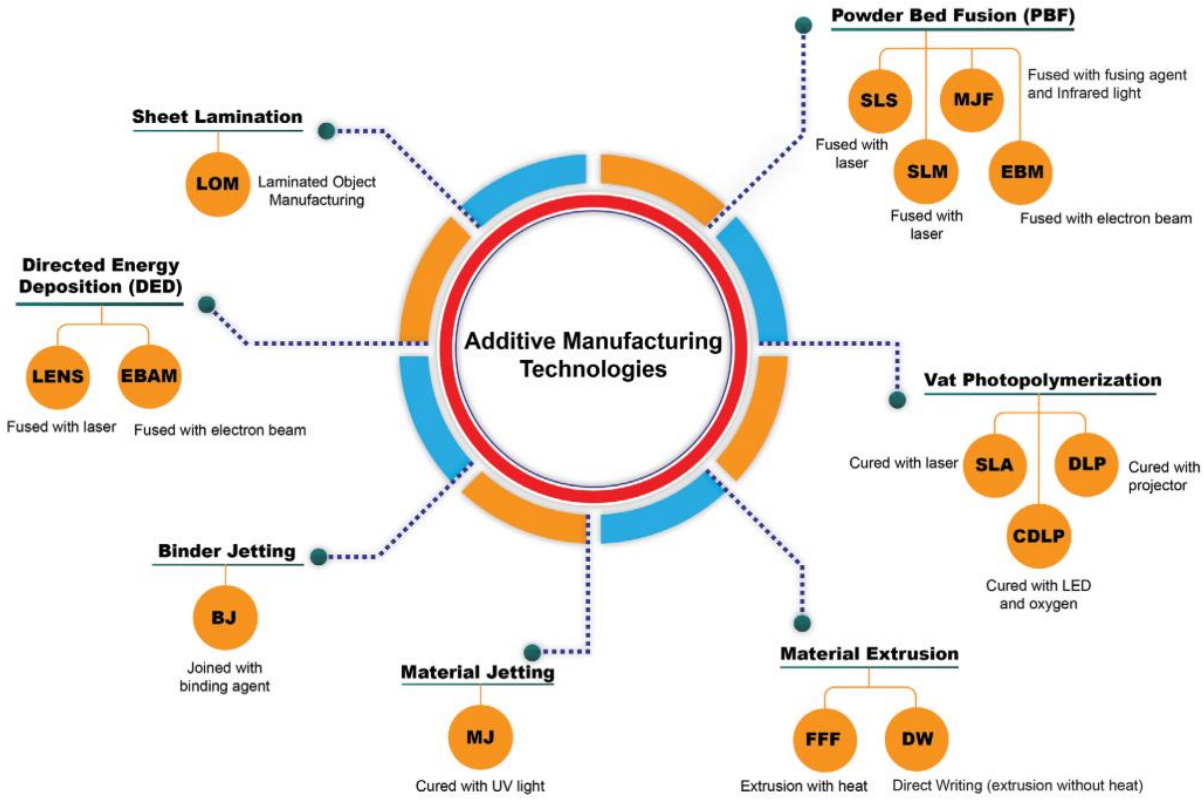

Figure 3. The seven distinct categories of AM and the technologies in each category [19]

2.2.1 Direct Metal Laser Sintering

The DMLS AM technology is a type of process within the Powder Bed Fusion (PBF) AM category. DMLS and Selective Laser Melting (SLM) are tradenames that essentially refer to the same technology, which has led to these two terms being used interchangeably to describe this process. The development of the DMLS process by EOS GmbH and the SLM process by SLM Solutions drew its motivation from the desire to process metal powders in the Selective Laser Sintering (SLS) process in which the primary feedstock materials were plastic [20]. The main difference, however, is the temperature of the powder bed. The SLM powder bed is preheated to a temperature below the melting temperature of the powder particles to minimise the effects of the residual stresses on the produced parts. [13], [21].

The working principle of the DMLS process

Figure 4 below provides an illustration of the basic operating principle of the DMLS process.

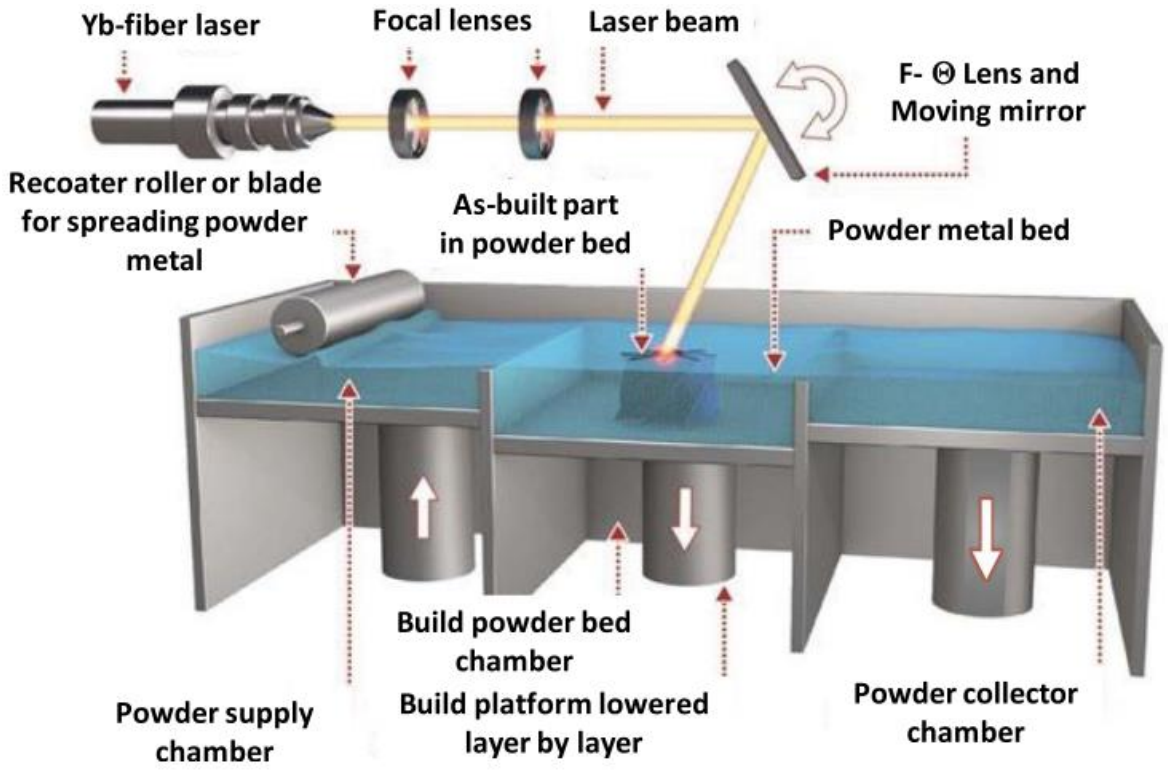

Figure 4. A schematic illustrating the basic operating principle of the DMLS process [22]

The DMLS process, like any other typical AM process, begins with the acquisition of a 3D CAD model of the part to be manufactured. This CAD model is then mathematically sliced into thin 2-dimensional (2D) layers in the order of micrometres by software and converted into an STL file. The STL file is then imported into the DMLS equipment, and each 2D layer acts as a blueprint that provides geometrical information for that cross-section of the part. A flat and homogeneous layer of metal powder is then distributed by a re-coater assembly (levelling roller or blade) from the powder feed supply chamber across the build platform on which the part is built. Excess powder is then collected in the powder collector chamber. A Yb-fibre laser guided by the digital blueprint of the current layer then selectively fuses the powder layer according to the geometry required for that layer. Each layer consists of a series of single laser-melted tracks that are deposited next to each other according to the diameter of the scanning laser beam and the selected overlapping distance (hatch distance) between them. After the first layer has been built, the build piston then lowers the build platform while the powder feed piston lifts the reservoir platform by a distance that is equal to the thickness of the next layer. The re-coater then spreads another layer of powder across the build platform, and the fusion process is repeated until the required part is produced. The first layer is built on a metal substrate, and the next layer is then fused onto the previously deposited layer. Therefore, each layer acts as a substrate for the next layer to be deposited. Support structures are used to support parts with overhanging features, and these supports are removed during post-processing [13], [23].

The production of a part in the DMLS process is essentially the result of the fusion of individual single tracks and single layers, as illustrated in Figure 5 [21].

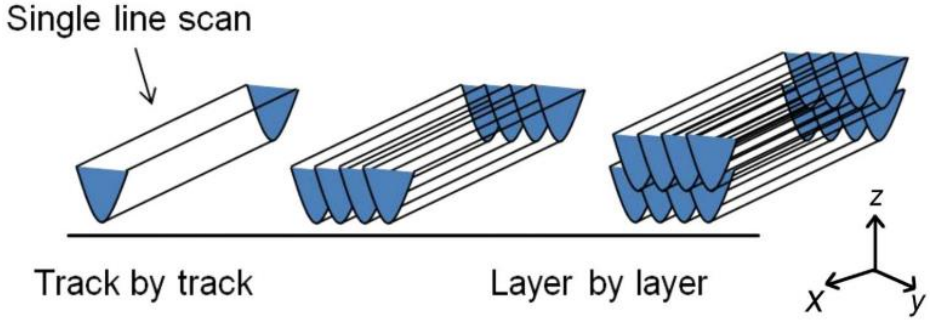

Figure 5. Illustration of a 3D part as a function of singe tracks [21]

It can be said that a single track is the primary unit of all DMLS-produced parts. When attempting to produce a part with the DMLS process from any metallic powder material, it is necessary first to develop a set of process parameters that can produce good quality, defect-free single tracks. Once these process parameters have been developed, they can be used to produce a layer consisting of a series of these single tracks for which a suitable overlapping distance can be determined to produce a defect-free layer. After mastering the production of a defect-free layer, the process can continue in a layer-by-layer fashion until a part has been built [2].

The principal process parameters that govern the production of an optimal single track are laser power, scanning speed, layer thickness and hatch distance (overlapping distance between two consecutive tracks) [2]. Although these are not the only process parameters involved, machine operators aim to achieve properties and characteristics such as good mechanical strength, low surface roughness, high dimensional accuracy and a minimum production time when producing parts using the DMLS process through the optimisation of these process parameters. The use of optimised input-based process parameters ensures the production of parts with the required properties and characteristics [2], [24]. A network diagram that displays the relationship between the process parameters and the resultant properties is shown in Figure 6 [25].

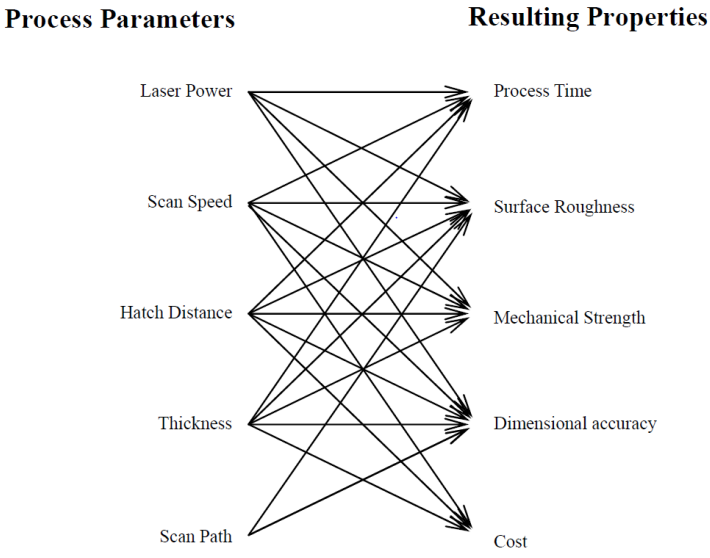

Figure 6. The resulting properties of DMLS-produced parts as a factor of the process parameters [25]

The DMLS process is an extremely parameter-sensitive process [26]. Altering one of the parameters can have an adverse effect on the resultant properties. A combination of moderately high laser power and low scanning speed will allow the metallic powders to absorb more laser energy, resulting in a part with a high density. However, extremely high laser power at the same scanning speed will result in more energy being transferred to the loose powder in the periphery of the laser spot, increasing the consolidation zone and resulting in part inaccuracy. Additionally, a high laser power will also increase the surface roughness due to spatter particles that tend to increase with an increase in laser power. It is imperative that the process parameters used to produce parts with the DMLS process be optimised in order to obtain good part properties [27].

2.3 DMLS process parameter optimization

As illustrated in section 2.2.1, the procedure employed in the DMLS process to produce parts involves the deposition of single tracks, layers and the final 3D parts from a powder feedstock. Each powder material employed in the DMLS process requires the development of process parameters that have been tailored for the production of high-quality, defect-free parts from that particular feedstock material [2]. Since the DMLS process is complex, there are many process parameters (machine, material and process-based parameters) that govern the production of parts [26]. From the literature, it became apparent that the most critical process parameters are the laser power (W), laser spot size (μm), laser wavelength (ηm), scanning velocity (m/s), hatch distance (μm) and layer thickness (μm) [28]–[30].

A closer inspection of these critical process parameters within the context of part production revealed that parameters such as the laser spot size and wavelength are usually fixed and cannot be altered mid-production [29]. The layer thickness can be selected and fixed according to the desired surface finish. Therefore, the remaining parameters that can be altered to investigate the production of high-quality parts are the laser powder, scanning speed and hatch distance. The selection of an optimum combination of these process parameters is crucial for the deposition of optimum single tracks, layers and final 3D parts [2], [29]. Yadroitsev et al. [2] and Dilip et al. [31] studied single track and layer formation from new powder materials, and their

findings can thus be used as guidelines for the development of process parameters suitable for the production of high-quality DMLS-produced parts.

2.3.1 Single tracks

As demonstrated in Figure 5 in section 2.2.1, single tracks are the building blocks of DMLS-produced parts. It is imperative that the process parameters that govern the production of single tracks be optimised to meet the mechanical property, density and surface quality requirements of the final parts [32]. This can be done by first generating an experimental design consisting of a wide range of primary process parameters, such as laser power, layer thickness and scanning speed that govern the deposition of a single track. These primary process parameters can be used to produce numerous single tracks, which can then be analysed to identify the parameter set that delivers single tracks with the optimum track characteristics.

2.3.1.1 Single track characteristics

The scanning process parameters can be optimised through the comprehension of the optimum and non-optimum single-track characteristics [20],[29]. The two main characteristics that are important in the analysis of single tracks are the track continuity and the geometry of the track penetration into the substrate. These characteristics are heavily reliant on the laser linear energy density (LED) employed during their deposition [2]. The LED can be described as the laser energy per unit of speed and is given by Equation 1 [32]:

$$\boldsymbol{LED}: \frac{\boldsymbol{P}}{\boldsymbol{V}} \left(\frac{\boldsymbol{J}}{\boldsymbol{m}}\right) \quad (1)$$

where P is the laser power (W) and V is the scanning speed (m/s).

Figure 7 displays the different morphologies of single tracks that can be formed during part production in the DMLS process [32].

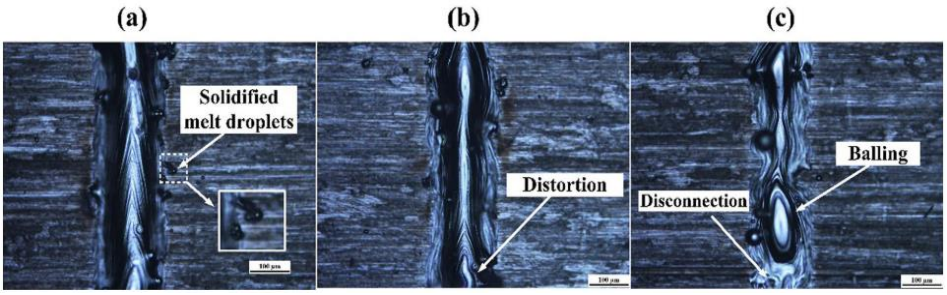

Figure 7. The different kinds of single-track morphologies that are formed during single-track production in the DMLS process: (a) Thick, deep penetrated and continuous, (b) Thin and continuous, (c) Thin, non-continuous exhibiting balling [32]

The width and the solidified melt droplets of the single track are displayed in Figure 7(a) suggest that the LED that was used to produce the track was excessive, i.e. a low scanning speed was selected for a given laser power. When the LED is excessive, more powder is drawn into the molten pool, and the laser does not only fuse the powder that is under the laser beam spot but also the surrounding powder particles; thus, wide and deep penetrated tracks are formed. Depending on the target application, these kinds of single tracks are undesired for DMLS-produced parts as they result in gas pores within the part [2], [26], [32]. The solidified melt droplets that can be seen alongside the single track also suggest that the LED used to produce this single track was excessive. When the LED is excessive, the temperature of the melt pool rises considerably to a point where partial vaporisation of the molten pool occurs, causing a recoil pressure that acts on the molten pool. The recoil pressure resulting from the vaporised material results in the molten metal being ejected from the melt pool, which rapidly solidifies in-flight, resulting in the formation of spherical melt droplets on the powder bed or on the single tracks. The width of the track can be controlled, and the melt droplets can be reduced by decreasing the LED [32].

The single track displayed in Figure 7(b) is continuous and void of solidified melt droplets, which suggests that the LED used in the production of this track may be moderate. However, this single track is slightly distorted. Yu et al. [32] attributed this

distortion to the non-symmetrical distribution of the powder in the path of the laser scanning direction in the powder bed. When the laser beam approaches this area of unsymmetrical powder distribution, the melt pool tends to distort by an angle to the side with the most powder because of the effect of the surface tension. Therefore, when the melt pool solidifies, a continuous single track that is distorted by an angle with respect to the laser scanning direction is formed. The occurrence of this phenomenon can be reduced by using powder feedstock with powder particles that are within a controlled Particle Size Distribution (PSD), resulting in a higher and more uniform packing density. A uniform packing density allows for a consistent interaction between the powder in the powder bed and the Gaussian laser beam, eliminating the occurrence of defects such as single-track distortion [33].

The balling effect displayed in Figure 7(c) is a common occurrence in the formation of single tracks in the DMLS process [2], [26], [32]. This phenomenon usually occurs when a high scanning speed for a given laser power, i.e., a relatively low LED is used to produce a single track. Due to the high scanning speed, the laser-to-powder bed interaction time is reduced, resulting in less thermal energy being transferred from the laser to the powder bed. This reduced thermal energy may be adequate to completely melt the smaller powder particles in the path of the laser beam. Still, it would not be enough to completely melt the larger particles and penetrate the substrate or previously deposited layer. Since the surface tension of the substrate is inversely proportional to the temperature of the melt pool, the relatively lower melt pool temperature results in an increased Plateau-Rayleigh instability that acts on the molten pool as it is deposited by the high-speed laser beam. The Plateau-Rayleigh instability describes the propensity of a stream of liquid to fragment into smaller sections under the effect of surface tension [34]. The molten pool can be considered as a liquid stream with a certain width-to-length ratio. If the width of the molten pool is considerably smaller than its length, it will be more prone to Plateau-Rayleigh instability, which is the case with single tracks produced from a relatively low LED. The incompletely melted powder particles in the molten pool paired with the Plateau-Rayleigh instability result in a solidified track that is discontinuous, broken up into ellipsoidal and spherical solidified melt droplets, exhibiting the balling effect [2], [34].

The balling effect is detrimental to the DMLS process as it can result in defects such as porosity, poor surface finish and inconsistent layer bonding [35]. To avoid the balling phenomenon, the scanning speed should be reduced for the given laser power, resulting in an adequate laser-to-powder interaction time. A lower layer thickness should also be used to minimise the occurrence of the balling effect. A lower layer thickness allows for better thermal interaction between the laser, powder particles and the substrate, resulting in the formation of a stable melt pool with adequate penetration into the substrate [2], [36].

A micrograph of a typical single-track cross-section is shown in Figure 8.

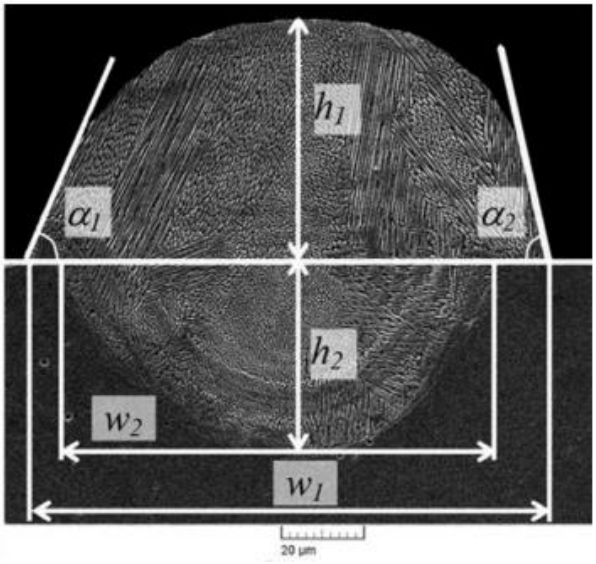

Figure 8. Typical cross-sectional characteristics of a single-track [26]

The crucial characteristics that are investigated in single-track formation are the track height (*h1*), penetration depth (h2), track width (*w1*), the width of the contact zone (w2), shape into the substrate, and the angle of contact (α1 and α2). The total height (*h1+h2*) of the single track is dependent on several parameters, such as the LED, layer thickness and the packing density of the powder bed [26], [37]. A relatively high LED radiates more energy into the powder bed, therefore involving more powder in the melt pool, resulting in deeply penetrated single tracks with a relatively high height above the substrate (h2). A relatively low LED, on the other hand, may not radiate sufficient energy to melt the powders and penetrate the substrate, consequently resulting in a lower single-track height. Since the layer thickness determines the

volume of powder available for single-track production, it has a notable effect on the height of the produced single track [26]. A relatively high LED would be required to melt a layer with a relatively high layer thickness fully, resulting in the formation of a greater melt pool size, which will solidify into a single track with a relatively high height. A relatively lower layer thickness would require a lower LED, resulting in the formation of a smaller melt pool and solidifying into a single track with a lower track height. A powder bed which consists of spherical powders within a controlled PSD will have a uniform packing density, resulting in the production of single tracks with a constant track height along its length. A powder bed that consists of irregularly shaped powders within a certain PSD will have an inconsistent packing density due to the mismatch between the irregularly shaped powders, resulting in the production of a single track with a varied track height along its length, as there will be a variation in the shrinkage and the solidification time due to the varied packing density [26].

The track width and penetration depth, on the other hand, are controlled by the LED [2]. As explained in the continuity discussion based on Figure 7, when the LED is excessive (low scanning speed for given laser power), thick and deeply penetrated single tracks are formed. Likewise, when a low LED is used, unstable, relatively thin single tracks with little to no penetration into the substrate are formed [26].

The shape of the single-track penetration into the substrate is also dependent on the LED and the mode of thermal conduction [2]. When the LED is moderate, the heat transfer from the molten pool to the substrate occurs through the normal convection in the molten pool and conduction heat transfer from the molten pool into the substrate without any boiling and evaporation of the molten pool. This is the preferred type of heat transfer between the molten pool and the substrate, and it is known as the conduction mode, which is characterised by a semi-circular U-shape penetration into the substrate. A significant increase in the LED past a certain threshold results in a substantial increase in the heat energy radiated to the powder and the substrate. This increased heat energy causes localised melting and vaporisation of the powder particles and substrate material, causing the formation of a melt pool with a cross-section that resembles a keyhole. The vaporised metal (powder particles) then seeks to escape the melt pool. It travels from the bottom to the top of the melt pool at a high velocity, resulting in the formation of a vapour jet that tends to travel vertically in a

direction opposite to the laser radiation. The high heat energy from the laser beam promotes the localised boiling and evaporation of the melt pool. In contrast, the high solidification rate (up to 108 K/s) [38] typical of the DMLS process results in the entrapment of some of the metal vapour and gas contained within the deeply penetrated single track. A single track with a deep penetration that resembles a keyhole is formed upon solidification. This kind of laser-material interaction is known as the keyhole mode. Depending on the target application of the parts being produced, the keyhole effect can be beneficial or detrimental to the properties of the parts. In the case where parts with an increased density are required, the concentrated laser energy will promote the complete melting of the powders while also remelting the previous layers, thereby increasing the density of the part in-situ [38]. However, this type of penetration can result in gas pores as the pockets of air that have been trapped in the melt pool collapse upon solidification, leading to the formation of voids within the AB part [2], [39], [40].

It has already been established that the DMLS process is a process parameter-sensitive process [41]. The single-track formation mechanism must be understood to avoid the formation of defects in the AB parts. A summary of how the relationship between the laser power and scanning speed affects the quality of the single track is shown in Figure 9. From this figure, it is evident that the laser power and scanning speed used for any given layer thickness governs the quality outcome of the produced single track. For a given laser power, the keyhole formation can be prevented by increasing the scanning speed, thereby reducing the LED. The balling phenomenon can be avoided by decreasing the scanning speed per given laser power, resulting in a moderate LED that can produce continuous single tracks. The occurrence of the lack-of-fusion phenomenon can be avoided by ensuring sufficient laser power for the selected scanning speed [26], [36]. For each type of powder feedstock, an optimum operating window exists in which high-quality single tracks can be produced. This optimum operating window can be found by understanding the dynamics of single-track formation [42], [43].

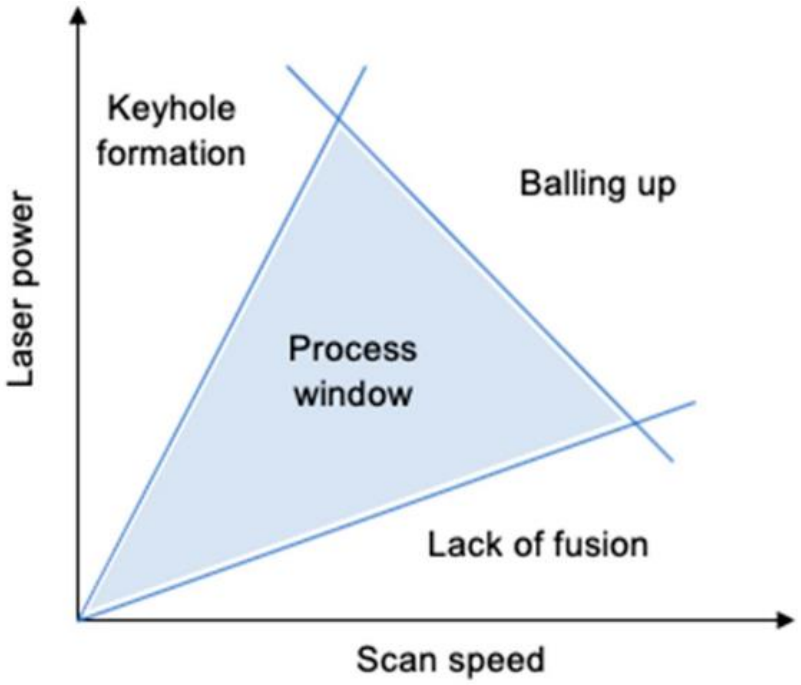

Figure 9. DMLS process outcomes as a function of laser power and scanning speed [42]

The stability of a single track can be determined and predicted by inspecting the angle of contact (ɵ) between the molten track and the substrate [2], [44], [45]. When a single track is deposited onto the substrate, the molten pool forms and the stability of the single track is affected by the intermolecular interactions between the phases present at the three-phase contact line [45]. The phases that are present and interact with each other during the single-track deposition are liquid (molten pool), solid (substrate) and vapour (evaporation emitted from the molten pool), as illustrated in Figure 10. The angle of contact, ɵ, is, therefore, the angle between the liquid-to-solid contact line and the tangent of the single track profile that results from the interaction between the three phases present at the triple point [44], [45].

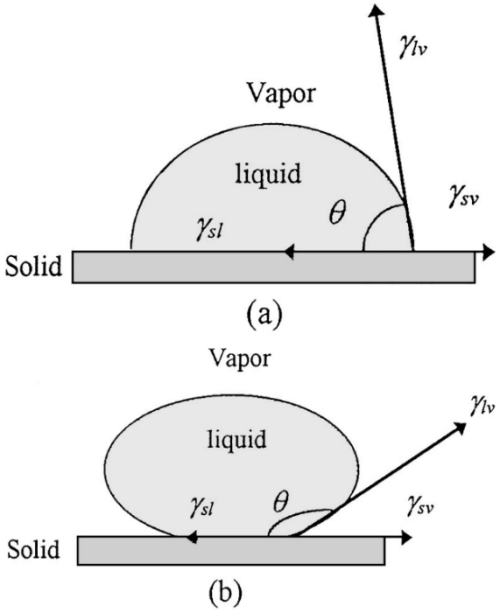

Figure 10. The angle of contact as a function of material phases present during single-track deposition, (a) wetting and (b) non-wetting [46]

The interaction of these three phases can be characterised by the degree of "wettability" that occurs during the deposition of the single tracks [44]. The term "wettability" refers to the macroscopic interactions between the different phases of the triple point [46]. During single-track deposition, the molten pool experiences cohesive and adhesive forces. The cohesive forces act within the molten pool and tend to keep the molten pool together, while the adhesive forces act between the liquid and solid phases and tend to spread the molten pool onto the substrate [45]. If the cohesive forces are greater than the adhesive forces, the molten pool will contract into spherical balls that have minimum contact with the substrate with a high contact angle (Figure 10(a)), resulting in the balling phenomenon. In the case where the adhesive forces are greater than the cohesive forces, the liquid-to-solid contact length will be longer, leading to a smaller contact angle, as demonstrated in Figure 10(b), resulting in a continuous single track [46]. A contact angle of less than 90° proves that the wetting between the liquid and the substrate was sufficient, while a contact angle greater than 90° is an illustration of poor wettability and an indication of the occurrence of the balling effect [44]. When the LED is not sufficient to penetrate the substrate, poor wettability occurs, causing the balling phenomenon to occur. It can be said that an increase in the LED will result in good wettability and, in turn, a contact angle that is less than 90° [47].

2.3.1.2 Substrate denudation

Upon solidification of a single track, an area void of powder is usually visible in the immediate vicinity of the solidified single track in the powder bed. This absence of powder particles in the vicinity of the processing area is a direct result of the denudation effect [48], [49]. Figure 11 illustrates the effect of the denudation phenomena in which the denuded width (area without powder) can be seen.

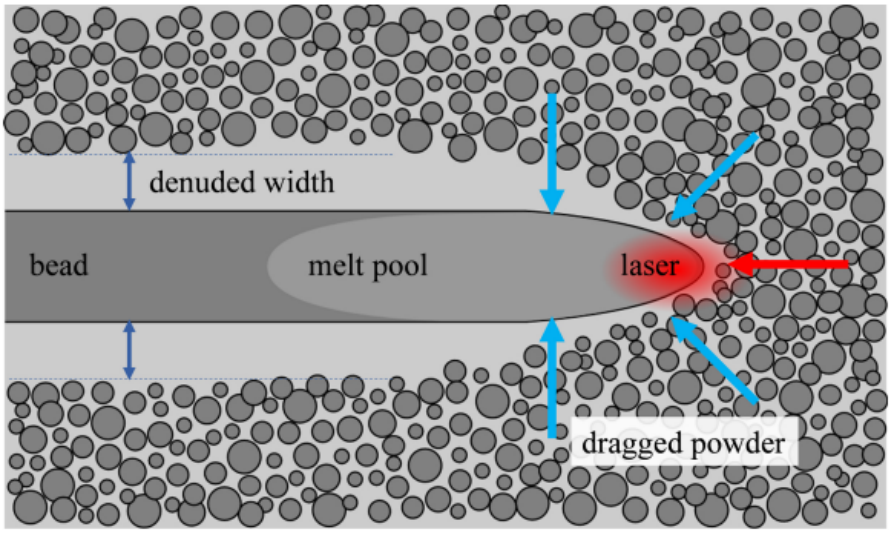

Figure 11. An illustration of the denudation effect [50]

Several mechanisms bring about the denudation phenomenon during DMLS part production. [51]. One of these mechanisms is the effect of the Marangoni convection within the melt pool. With reference to LPBF, the Marangoni effect depicts the outward flow of the molten material within the melt pool due to the effect of surface tension caused by the temperature gradient present between the centre and the edges of the melt pool as a result of the non-uniform energy distribution by the laser beam [52]. This effect is believed to contribute to the formation of the denuded width as it is suspected that there is an uptake of the loose powder surrounding the single track into the molten pool by virtue of the outward circulating flow in the molten pool, therefore widening the molten pool and resulting in attachment and possible absorption of the surrounding powders in contact with the molten pool [49]. Although this is a generally accepted explanation, it fails to account for the large width of the denuded zone that is commonly seen in the DMLS production of parts, suggesting that there are more dominant mechanisms that bring about this effect.

Figure 12 illustrates two more mechanisms that can possibly be responsible for the denudation effect. The Knudsen number (Kn) is a unitless number used to describe the type of gas flow present in the AM system during part production. A low Kn value (Kn < 1) indicates that gas flow in the system can be described as a continuous medium wherein the standard fluid mechanics principles are applicable. A high Kn value (Kn>1) indicates that the gas flow in the system is irregular, and other factors, such as the interaction between the individual gas molecules and the powder particles, need to be considered [49], [53].

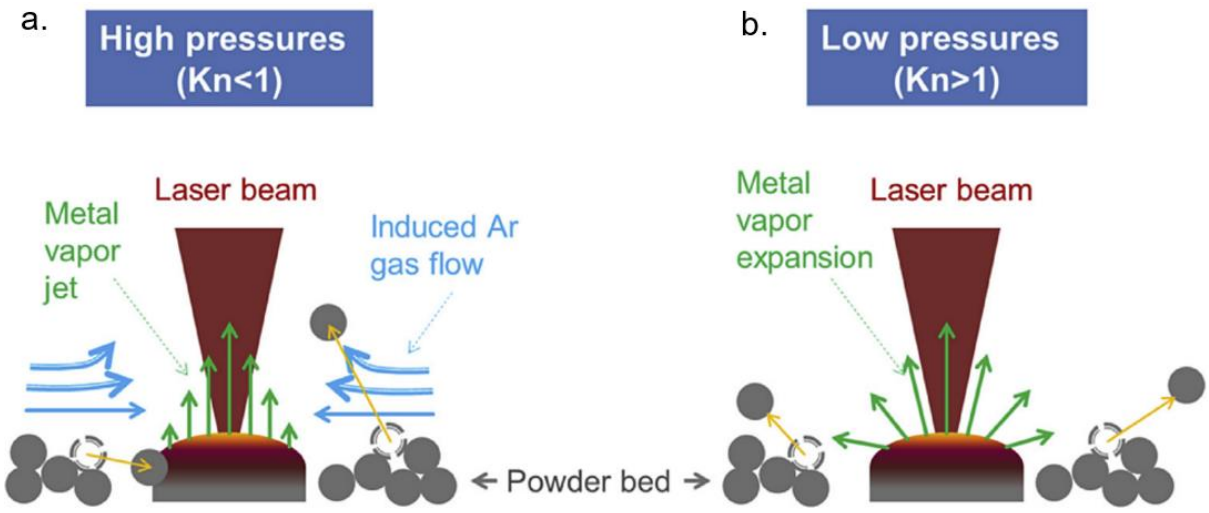

Figure 12. The two mechanisms behind the denudation effect as a function of the shielding gas pressure [49]

These mechanisms consider the effect of the pressurised shielding gas used in the production chamber to prevent the high-temperature oxidation of the parts. At high shielding gas pressure (see Figure 12(a)), Matthews et al. [49] observed that powder was drawn in from the surroundings and incorporated into the melt pool, leaving a large area around the solidified single track without powder. As the dynamic laser beam interacts with the metal powder, the powders melt and form a molten pool, and the surface of this molten pool is heated to or beyond the boiling point of the feedstock material, leading to evaporation through a metal vapour flux. Since the system is pressurised, the evaporation causes a pressure drop at the surface of the melt pool, leading to powder being drawn in from the surroundings, transported by the high-pressure shielding gas through the Bernoulli effect. The dragged powder can either be drawn into the melt pool and become completely melted, or it can be partially

melted, resulting in a single track and, therefore, a layer with a high surface roughness. Additionally, the dragged powders may become partially melted and ejected from the fusion area, landing and solidifying as melt spatter particles. This mechanism has been accepted as the dominating cause of the denudation effect [48], [49].

In Figure 12(b), it is illustrated how, at low shielding gas pressure, the powder particles are propelled away from the melt pool, leading to a denudation zone, which can be characterised by a pile-up of powder particles at the contour of the denudation zone. Since the ambient gas pressure is low, the melt vapour pressure originating from the fusion area is greater. Therefore, the metal vapour is ejected in different directions from the molten pool. The powder surrounding the fusion area is then transported away from this area through the metal vapour flow. This mechanism results in a wider denudation zone compared to the high-pressure mechanism [49].

The denudation effect is undesired in LPBF as less powder is available to produce the consecutive single track, leading to layer height non-uniformity. Additionally, this effect influences the surface roughness of the layer by causing spatter particles [51], [54]. As much as the denudation effect has been portrayed as a function of the shielding gas pressure, process parameter optimisation remains of utmost importance to smoothen the interaction between the laser beam and the powder feedstock [54].

2.3.2 Single and double layers

The process parameters that govern the deposition of a layer are illustrated in Figure 13. From this figure, process parameters such as the laser power, scanning speed and layer thickness determine the morphology of the single tracks. It is further evident that the morphology of each deposited single track affects the morphology of the DMLS-produced layer since a layer is essentially an array of individually deposited single tracks. Apart from the single-track characteristics, Figure 13 illustrates that the morphology of a DMLS-produced layer is affected by the hatch spacing, also known as the hatch distance, used to produce the layer [55].

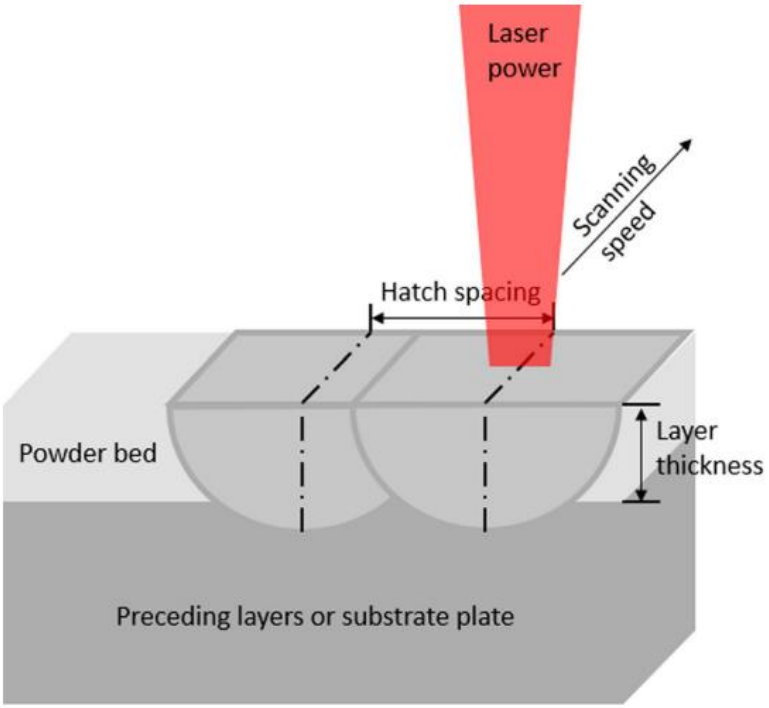

Figure 13. The input-based process parameters required for layer production [49]

During layer formation, single tracks are deposited in an array at a particular distance apart, which allows the overlapping of the consecutive single tracks. This distance is the hatch distance, and it can be defined as the distance between the centres of two consecutive single tracks, as shown in Figure 13 [2]. Careful consideration of the single-track characteristics should be given in the selection of an optimum hatch distance. From the literature, it was found that the value of the hatch distance should not exceed the value of the single-track width to ensure sufficient overlapping and bondage of the single tracks instead of being deposited as a series of individual tracks [2]. A hatch distance much smaller than the width of the single track (i.e. < 50% of the track width) may result in the production of a layer with a lower surface roughness but at the cost of the production time. If the value of the hatch distance is comparative to or larger than the value of the track width (i.e. > 90% of the track width), there will be a minimum or lack of bondage and overlapping between the deposited single tracks, resulting in individual or connected channels of pores, as illustrated in Figure 14, accompanied by a decrease in the mechanical properties of the final part [56].

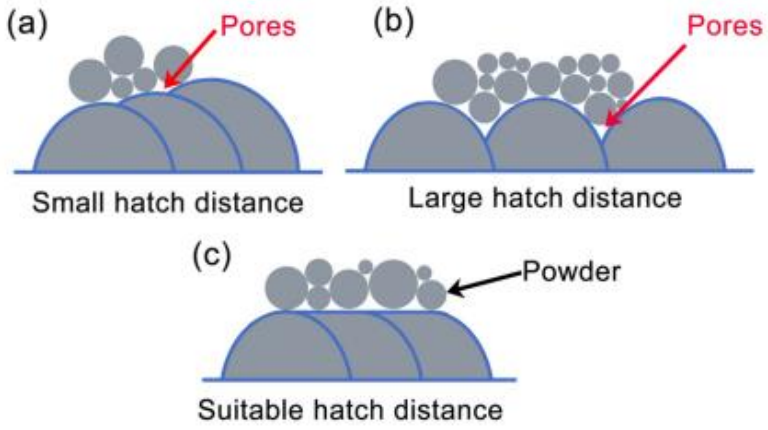

Figure 14. The effect of the hatch distance in the DMLS process: (a) small hatch distance, (b) large hatch distance and (c) suitable hatch distance (50%) [56]

The production of parts in LPBF entails repeated cycles of localised heating (melting) and cooling (solidification) of the powder feedstock in the powder bed. The heat energy radiated by the laser (up to 3500 K) [54] results in an expansion while the rapid solidification due to the high cooling rate (up to 10^6 K/s) [57] results in the contraction of the fused material. Since the melt pool to solidified material transition occurs rapidly, there is a steep temperature gradient across the material as the dynamic laser fuses the powder particles in its scanning path. This steep temperature gradient is ,accompanied by a restricted expansion due to the rapid contraction of the fused material, causing residual stresses in the part [57]–[59]. The Ti6Al4V alloy is sensitive to rapid temperature changes during its production [60]. The steep temperature gradients result in the formation of an α' Ti6Al4V microstructure. This kind of microstructure results in the production of parts that have a high strength-to-ductility ratio, negatively affecting the toughness of the part [57], [61]. The residual stresses cause the deformation and cracking of the part and affect the fatigue life of the part [57].

To mitigate the effect of the high-temperature gradient in-situ, several scanning strategies have been developed and introduced by researchers [62]–[64]. The link between the scanning strategy, thermal gradient, microstructure and mechanical properties has been demonstrated in the literature [63], [65]. Figure 15 illustrates the common scanning strategies used in the LPBF production of parts.

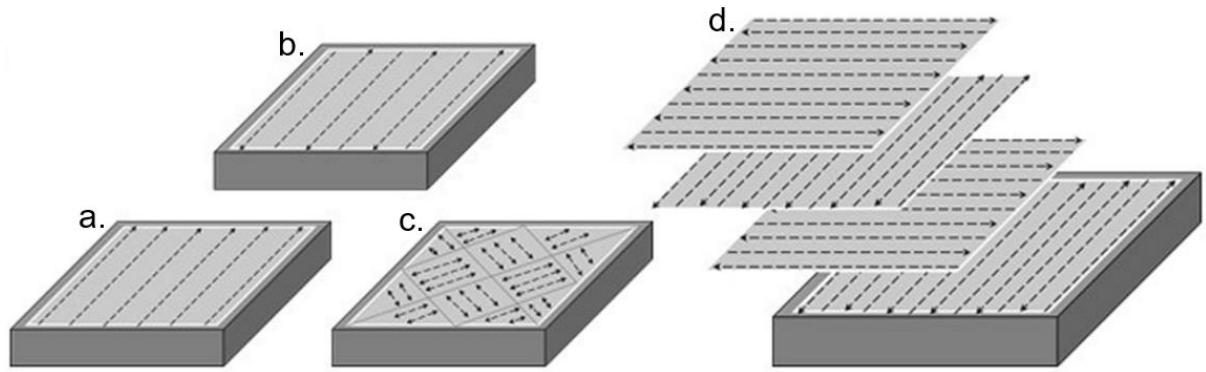

Figure 15. Common scanning strategies employed in LPBF processes: (a) unidirectional, (b) bidirectional, (c) island and (d) layer rotation paired with bidirectional scanning with a 90°-layer rotation. Adapted from [66] **and edited**

The unidirectional scanning strategy (Figure 15(a)), although reported to cause unidirectional residual stress distribution, is the basic strategy on which other scanning strategies have been developed. The direction of the laser beam can be changed to sinter each single track in a direction opposite to the previously sintered single track, resulting in the bidirectional scanning strategy (see Figure 15(b)). However, like the unidirectional scanning strategy, the bidirectional scanning strategy results in residual stresses that are distributed along the x and y directions, depending on the laser scanning direction [62]. The island scanning strategy (Figure 15 (c)) utilises shorter scan tracks to fuse the powders in a series of individual squares (islands) to form a layer. It has been reported that the effectiveness of the island scanning strategy in decreasing the formation of residual stresses in the final part is directly proportional to the length of the single tracks, which may affect the build time [64], [67], [68]. The layer rotation strategy (Figure 15 (d)) is based on the production of a layer using either the unidirectional or bidirectional scanning strategy and then rotating the scanning direction 90° to deposit the consecutive layer. Reviewed literature suggests that this scanning strategy results in lower and more uniform residual stresses in the produced parts compared to parts produced with no layer alternation [62].

The DMLS process primarily uses the two scanning strategies illustrated in Figure 16 to produce parts.

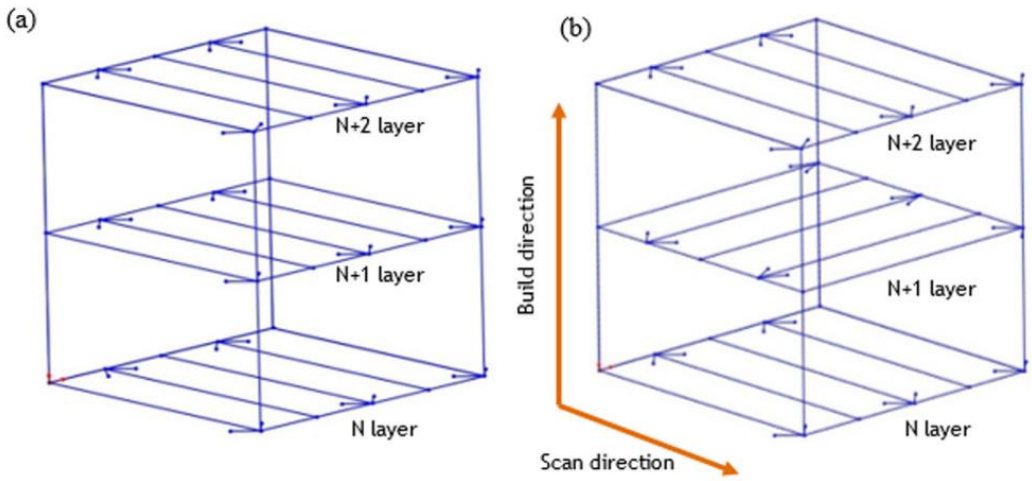

Figure 16. The scanning strategies commonly used to produce parts in the DMLS process are (a) bidirectional with no layer rotation and (b) bidirectional with layer rotation. Adapted from [69]

In the bidirectional scanning strategy with no layer rotation (X-X scanning), shown in Figure 16(a), a layer is formed as consecutive single tracks are fused by the laser in opposite scan directions on the powder bed. The bidirectional scanning strategy with layer rotation (X-Y scanning), shown in Figure 16(b), relies on the rotation of each fused layer at a certain angle relative to the previously deposited layer. The X-X scanning strategy has been reported to produce parts with a relatively lower density compared to the X-Y scanning strategy due to the formation of pores and voids in the parts [69], [70]. Since the layers are fused in one direction only, there is an uneven distribution of heat in the material as the part is being built, resulting in the development of residual stresses in the material. The residual stresses initiate the formation of tears and cracks on the fused layers, which affect the powder deposition for the next layer, resulting in the production of a non-uniform layer and ultimately, pores in the parts [71]. Due to the occurrence of such defects, the surface roughness of the parts produced using the X-X scanning strategy have a relatively higher surface roughness than the surfaces of the parts produced from the X-Y strategy [69], [70].

The rescanning strategy, which involves the processing of a fused layer twice, can be used in the DMLS process to reduce surface defects and improve densification [2], [63]. Rescanning can be used to optimise the properties of the parts to meet the requirements of a certain application such as the high-surface quality required for

turbine blades in the aerospace industry. Since the thermophysical properties of solidified metal and unmolten or partially molten powder are different, the second laser scan melts any unmolten powder from the first scan, improving the layer surface quality and increasing densification. Authors such as Yadroitsev et al. [2] reported success in utilising the rescanning process to reduce surface defects and improve the density of produced parts by melting any unmolten particles that may not have been molten during the first laser scan. On the other hand, Haider et al. [63] found that employing the rescanning process is not feasible, considering the increased production time and the negative effects, such as decreased layer adhesion that this process has on the mechanical properties of the AB parts.

2.3.3 Three-dimensional parts

The layer-by-layer production of defect-free, high-quality parts with good mechanical and physical properties is heavily dependent on the optimisation of the single track and layer formation process parameters [2]. Once a 3D part has been produced from a set of process parameters, it must first be analysed to identify the microstructure and any defects, such as porosity within the part, to ensure that the process parameters are optimum. Several post-processing techniques, such as hot isostatic pressing (HIP) and heat treatment processes, such as stress-relieving and annealing, can be used to improve the quality of the part [72], [73].

Two types of pores are usually present in LPBF-produced parts: lack-of-fusion pores (LOF) and gas pores (see Figure 17) [57], [74]. These pores are usually characterised by their shape and size within the part. LOF pores are usually irregularly shaped, with a size range of 100–150 µm, and they take on a linear (perpendicular to build direction) orientation within the layers of the part, as shown in Figure 17(a) [57], [74], [75]. Gas pores, on the other hand, are normally scattered randomly in the part and are spherical in shape with diameters varying from 0–100 µm, as shown in Figure 17(b).

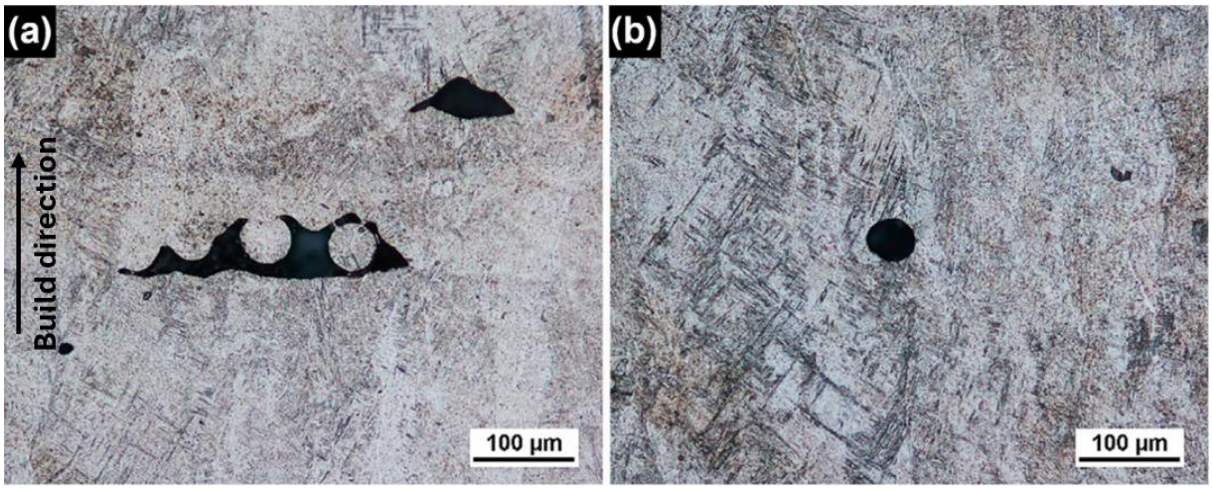

Figure 17. Optical micrographs of the typical pores present in LBPF parts. (a) Irregularly shaped lack-of-fusion pores and (b) a spherical gas pore. Adapted from [57] **and edited to show the build direction in (a)**

The LOF pores, as the name suggests, are formed when the LED is not sufficient to melt the deposited layer of powder while penetrating the previously deposited layer to allow for complete fusion between the two layers, causing irregularly shaped cavities with a high aspect ratio (width-to-height ratio). The LOF pores may contain unmolten powder particles within the boundaries of the unfused layers, while in some instances, the LOF pores may not necessarily contain unmolten powder particles. Figure 17(a) [57]. It is generally accepted that gas pores form due to individual powder particle porosity and trapped gas caused by the Marangoni turbulence in the melt pool [74]. Additionally, the powder bed usually has a porosity that ranges from 30 to 50%, depending on the morphology and the PSD of the powder[76], [77], which is found within the spaces in between the packed powder particles. During part production, the loose powder is melted and some of the gas contained within the cavity of the powder bed is dissolved within the melt pool, while the remainder of the gas becomes trapped within the solidified metal due to the rapid solidification process. The trapped gas causes a spherical gas pore to form within the bulk of the part [57], [60]. Porosity in general, is an undesired defect in DMLS-produced components because it negatively affects the mechanical properties and the general cycle life of the parts. Due to the differences in their location, size and morphology, LOF and gas pores impact the parts in different ways. With respect to the mechanical properties and fatigue life, LOF pores are regarded to be more detrimental due to

their size and sharp edges that act as local stress concentration points and crack initiation sites in parts that experience loading in a direction that is parallel to the build direction. The gas pores have a less pronounced effect on the mechanical properties and fatigue life due to their spherical shape and relatively smaller size in comparison to the LOF pores [57], [74].

HIP can be applied to eliminate the pores present in the AB parts, thereby improving the density and the tensile and fatigue strengths of the AB parts [78], [79]. HIP relies on the application of heat and isostatic pressure to the part while it is contained in a pressure vessel. The combination of sub-melting point heat (between 900 to 920 °C) for Ti6Al4V [80], [81]) and uniformly distributed isostatic pressure (between 100 to 200 MPa [80]) for a holding time of 2–4 hours eliminates the pores through high-temperature and pressure diffusion [78], [80]. After densification has been completed, the heat is withdrawn, and the part is allowed to cool in the pressure vessel under the applied pressure to maintain the structural integrity and control the dimensional accuracy of the part. This process has been successfully used by Qin et al. [79] to improve the density of AISI M50 tool steel parts produced through LPBF by eliminating the pores.

The repeated rapid heating, melting and cooling of the feedstock and fused material in the LPBF process results in parts with a fine microstructure with columnar grains that are aligned parallel to the build direction (z-direction), as can be seen in Figure 18 [71].

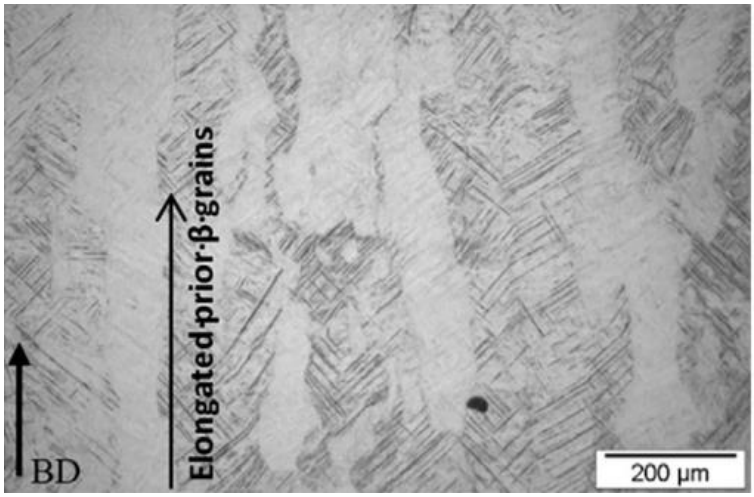

Figure 18. Typical LPBF AB Ti6Al4V microstructure with fine martensitic laths within columnar grains that are parallel to the build direction

The cooling rate has a significant effect on the size of the grains formed within the microstructure of the part. The high cooling rate (up to 10^6 K/s) typical of the LPBF process results in the formation of a fine-grained microstructure that consists of fine, needle-like grains, which can cause residual stresses in the parts due to the short grain nucleation time [82]. The steep thermal gradients between the melt pool and the previously solidified layers result in the columnar grains forming that are aligned parallel to the path of heat dissipation (build direction) [20], [71]. These grains grow epitaxially from the previously fused layer during the solidification of the newly fused layer, resulting in the growth of these grains across the fused layers. This AB microstructure, typical of LPBF-produced parts, results in parts that exhibit high strength, hardness and low ductility values [71]. Due to the low ductility, AB LPBF parts are generally considered to be brittle, and they are highly susceptible to sudden failure under dynamic or sudden loading conditions due to the quick propagation of cracks within the brittle material [83]. Additionally, the AB parts may exhibit anisotropy of the mechanical properties due to the preferential growth of the columnar grains along the build direction [20], [71]. This means that the parts would exhibit greater tensile values in the direction of grain alignment (z-direction) than in the x and y-directions.

To reduce the effect of the AB microstructure on the parts, heat treatment processes such as stress-relieving and annealing can reduce the residual stresses while

improving the overall mechanical properties of the part [20], [71], [84]. During stress-relieving, the part is furnace-heated to 650 °C for Ti6Al4V [84]), which is below the recrystallization temperature of the material, and held at that temperature for a certain amount of time (two hours for the Ti6Al4V alloy [84]) before the part is removed from the substrate. The part is then slowly cooled through air cooling to prevent the regeneration of the fine-grained microstructure associated with rapid cooling. Heating and holding the part at a temperature below the recrystallization temperature of the material results in the relaxation of the internal stresses by exciting the atoms of the material and providing them with the energy to move and redistribute more evenly within the material. Through this mechanism, stress-relieving eliminates the distortion and warping of the parts when they are removed from the substrate [71], [84].

The annealing heat treatment can be applied to parts to transform the fine and brittle microstructure into a more equiaxed and ductile microstructure while reducing the internal stresses within the part [85]. During annealing, the part is normally heated to a temperature that is below the melting point of the part material and held at that temperature for a period of two to four hours, depending on the composition of the material and the desired final microstructure, and then either slowly cooled in the furnace or rapidly cooled through water quenching [57], [85]. In the case of the Ti6Al4V alloy, the part can be heated to a temperature that is either below or above the β-phase transformation temperature (β-transus) of the alloy (995 °C) [84], [86]. Sub-β-transit annealing is usually carried out at a range of 700 to 950 C, resulting in a microstructure that has a balanced combination of the α and β phases since the microstructure was not transformed to a 100% β-phase state during heating [73]. Annealing below the β-transus temperature results in parts that have a balanced strength-to-ductility ratio due to the stable α+β microstructure formed upon furnace cooling [72]. In β-phase annealing, the part is heated to a temperature above the β-transus temperature, resulting in a microstructure that is completely dominated by the β-phase, which upon cooling, can either transform back into the fine, brittle microstructure (rapid cooling) or a more equiaxed α+β microstructure (slow furnace cooling) that is dominated by the β-phase [86]. This type of annealing process results in a Ti6Al4V alloy that has a higher hardness with a lower ductility [86]. Depending on the material and the desired mechanical properties, the different types of

annealing heat treatment can be applied to the AB LPBF parts to transform the microstructure and improve or tailor the mechanical properties of the produced parts.

2.4 Titanium metal

A lot of small but impactful discoveries, inventions and breakthroughs led to the gradual development of the extraction of titanium metal and consequently, the titanium industry. Titanium metal was initially discovered by William Gregor in the year 1791 [1], [87]. While examining the local river of Manaccan Valley, Cornwall England, Gregor came across ilmenite ($FeTiO_3$) in the form of a substance that resembled a “black sand” [1]. He then proceeded to produce an impure oxide of a new element by using a magnet to remove the iron (Fe) from this substance and then treating it with hydrochloric acid. Gregor named this impure oxide that resulted from his treatment “Manaccanite” (TiO_3) after the location where it was discovered. Two years later, in 1973, Martin Heinrich Klaproth from Berlin was able to isolate titanium oxide (TiO) from rutile (TiO_2), and he then named the new element “Titanium” after the Titans of Greek mythology [1]. Gregor saw this name to be a great fit for this metal because of the Greek mythology that the Titans had rebelled against their father, who, as a result, detained the Titans in the earth’s crust, similar to where the hard-to-extract Ti metal was found. A century later, in 1910, Matthew Albert Hunter from Troy, New York, heat-treated $TiCl_4$ with sodium through his “Hunter process” and succeeded in isolating the titanium metal. The last historic breakthrough was by Wilhelm Justin Kroll when he demonstrated that his process, the “Kroll Process” could produce large amounts of Ti by reducing $TiCl_4$ with magnesium (Mg). It was through this invention that he eventually became renowned as the “father of the titanium industry” [1].

2.4.1 Characteristics of pure titanium

Titanium metal appears on the periodic table of elements as a chemical element with atomic number and mass of 22 and 47.867 atomic mass units (AMU), respectively. It is a metallic silver metal that is characterised by its low density, high strength and exceptional corrosion resistance [6]. There are five stable isotopes of naturally occurring titanium ranging from ^{46}Ti to ^{50}Ti according to atomic mass. These isotopes are used for a wide range of applications and studies, such as producing radioisotopes and super-heavy elements. Ti is an allotropic element, which means

that it can consist of different allotropes (crystal structures) depending on the temperature it has been subjected to [6]. The allotropy of titanium is made up of two allotropes, alpha (α) and beta (β). The α allotrope exists in the form of a hexagonal close-packed (HCP) crystal structure at room temperature, while the β phase exists as a body-centred cubic (BCC) crystal structure at elevated temperatures, as shown in Figure 19 [1]. At room temperature, the distance between the atoms in the HCP structure (characterised by the nm lengths in Figure 19) is shorter compared to the atom spacing found in the high-temperature BCC structure. The shorter spacing between the atoms in the HCP structure suggests that the atoms are more tightly packed, hence the high strength and low ductility of Ti at room temperature compared to the high-temperature BCC Ti.

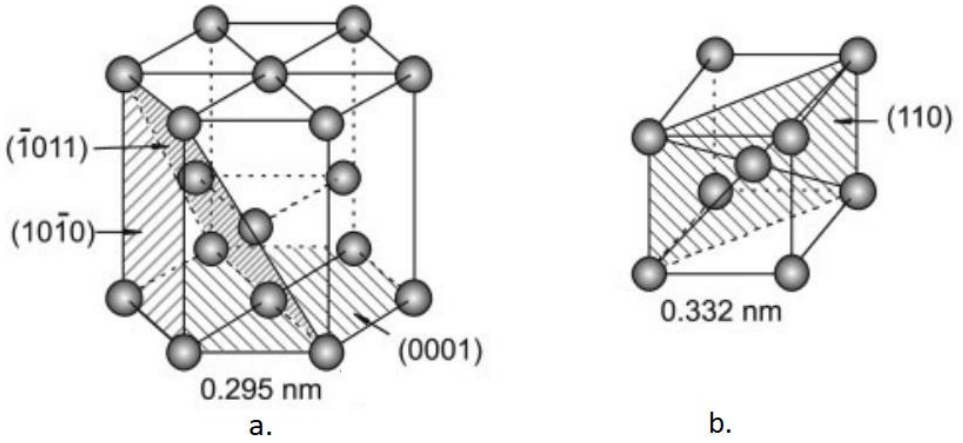

Figure 19. Crystal structure of the Ti allotropes, (a) Alpha HCP and (b) Beta BCC [1]

2.4.2 Extraction of titanium

The geographic distribution of the Ti metal reserves is shown in Figure 20 [88]. This figure shows that Ti metal reserves are widespread throughout the world. Most deposits suitable for mining are primarily located in Australia, Canada, Norway, South Africa, and Ukraine, listed in order of decreasing concentration. Ti is mined from the ore as a part of minerals such as rutile (TiO_2) and ilmenite ($FeTiO_3$), from which it is extracted using the Kroll process. Ilmenite is the most abundant ore of Ti, and it has a grey-to-blackish appearance, while rutile has a reddish-brown appearance [1]. Ilmenite, in comparison to other Ti-bearing minerals such as rutile, is a particularly inexpensive mineral that is usually pre-cleaned and processed through the Becher

process to separate the TiO_3 from the iron (Fe). The TiO_3 is then enriched to achieve a concentration that is similar to TiO_2 [1], [6]. The TiO_2 from $FeTiO_3$ or rutile TiO_2 is either directly reduced to Ti through an electrolytic process such as the FFC Cambridge process, or it can first be converted into $TiCl_4$ and further reduced into pure Ti through the Kroll and Hunter processes, with the former being the most used process for this application.

TITANIUM MINERAL CONCENTRATES

World Mine Production and Reserves: Reserves for Australia, Canada, China, Kenya, Madagascar, Mozambique, South Africa, and "Other countries" were revised based on company and Government reports.

	Mine production		Reserves[8]
	2022	2023e	
Ilmenite:			
United States[2, 9]	200	200	2,000
Australia	400	400	[10]180,000
Brazil	28	54	43,000
Canada[11]	520	500	52,000
China	3,140	3,100	210,000
India	210	210	85,000
Kenya	190	140	130
Madagascar[11]	320	320	27,000
Mozambique	1,400	1,600	22,000
Norway	410	430	37,000
Senegal	410	340	NA
South Africa[11]	1,100	1,000	28,000
Ukraine	190	60	5,900
Vietnam	170	140	1,600
Other countries	110	110	1,200
World total (ilmenite, rounded)[9]	8,800	8,600	690,000
Rutile:			
United States	(9)	(9)	(9)
Australia	200	200	[10]35,000
India	13	13	7,400
Kenya	73	58	70
Madagascar	—	—	520
Mozambique	8	9	720
Senegal	9	8	NA
Sierra Leone	130	110	2,900
South Africa	100	100	6,100
Ukraine	95	50	2,500
Other countries	10	10	20
World total (rutile, rounded)[9]	640	560	55,000
World total (ilmenite and rutile, rounded)	9,400	9,200	750,000

World Resources:[8] Ilmenite accounts for about 90% of the world's consumption of titanium minerals. World resources of anatase, ilmenite, and rutile total more than 2 billion tons.

Figure 20. Summary of the worldwide Ti reserves and production in 2023 [88]

The metallurgical Ti reduction processes can be classified by the primary product produced by these processes. The primary product from these reduction processes can either be Ti sponge or Ti powder that has been reduced directly from the precursor without the production of Ti sponge [11], [89]. Ti sponge refers to porous Ti lumps that are usually accompanied by a by-product (sponge fines) that can be used as Ti powder. The Ti sponge can then be used as the starting feedstock or raw material for Ti manufacturing and powder-making processes. There are three common reduction agents used in the production of Ti sponge and powder, namely

Mg, Na, and Ca. These reduction agents are preferred due to their excellent thermodynamic feasibility [11].

There are two main categories in which Ti extraction thermochemical processes can be classified: processes that extract Ti based on the reduction of $TiCl_4$ and processes that extract Ti based on the reduction of TiO_2. The processes reviewed in this section are processes that extract Ti from $TiCl_4$ using either Na, Mg or Ca as the reducing agent. At the time of writing, some of these processes had been commercialised while some were still under development.

2.4.2.1 Hunter process

The Hunter process, shown in Figure 21, was developed by Matthew Hunter in 1910, and it was the first and only industrial-scale process used to produce the Ti metal until the development of the Kroll process in the 1930s [90], [91]. The Hunter process is a thermochemical process based on the reduction of $TiCl_4$ using Na. This process was commercialised during the middle of the 20th century, and for a certain period, the Hunter and the Kroll processes were the only commercialised titanium production processes. In this process, Na is placed in a reactor furnace at a temperature above 800 °C, where it becomes molten. $TiCl_4$ is then gradually fed into the molten Na, and as soon as contact is made, a reaction occurs. In this reaction, NaCl is formed, and Ti crystals also begin to form and settle to the bottom of the liquid pool. The furnace temperature is above the melting points of both Na and Cl; therefore, they are always in a molten state. Powders produced from the Hunter process have a superior quality due to the Na atmosphere in the reactor, which protects these powders from air exposure [11], [91], [92].

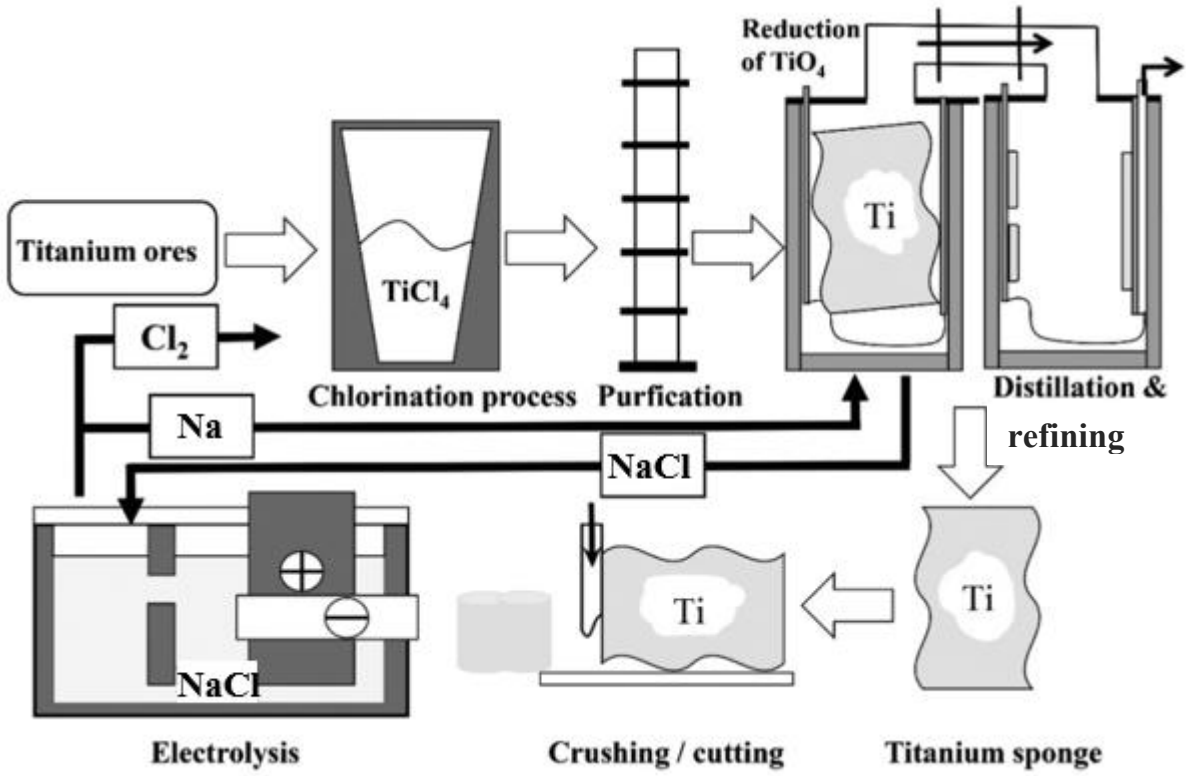

Figure 21. Schematic illustration of the Hunter process. Adapted from [90]**.**

When compared with the Kroll process, the Hunter process used twice as much Na than the Mg used in the Kroll process to yield the same amount of Ti sponge produced in the Kroll process. The Hunter process was then declared uneconomical, and it was stopped due to the high cost of the Na reducing agent [91]. However, a positive feature about the Hunter process is that its process parameters can be adjusted to produce both Ti sponge and powder or to produce Ti powder only [11], [90], [91], [93].

2.4.2.2 Kroll process

The Kroll process, diagrammatically shown in Figure 22, was developed by William J. Kroll in the 1930s, and it was the second commercial process used to produce primary Ti metal. This process uses Mg as a reducing agent to produce Ti sponge and sponge fines from $TiCl_4$. The Kroll process has been used since the 1940s as a Ti production method due to its cost effectiveness compared to the Hunter Process. Processes that were developed after the Kroll process were either equally or less economical when compared to this process [11], [89]. However, due to the increased interest in the Ti metal and its alloys, there have been ongoing attempts to develop

Ti production technologies that are more efficient and economical than the Kroll process to broaden the application of this metal and its alloys by reducing the costs associated with its production [93].

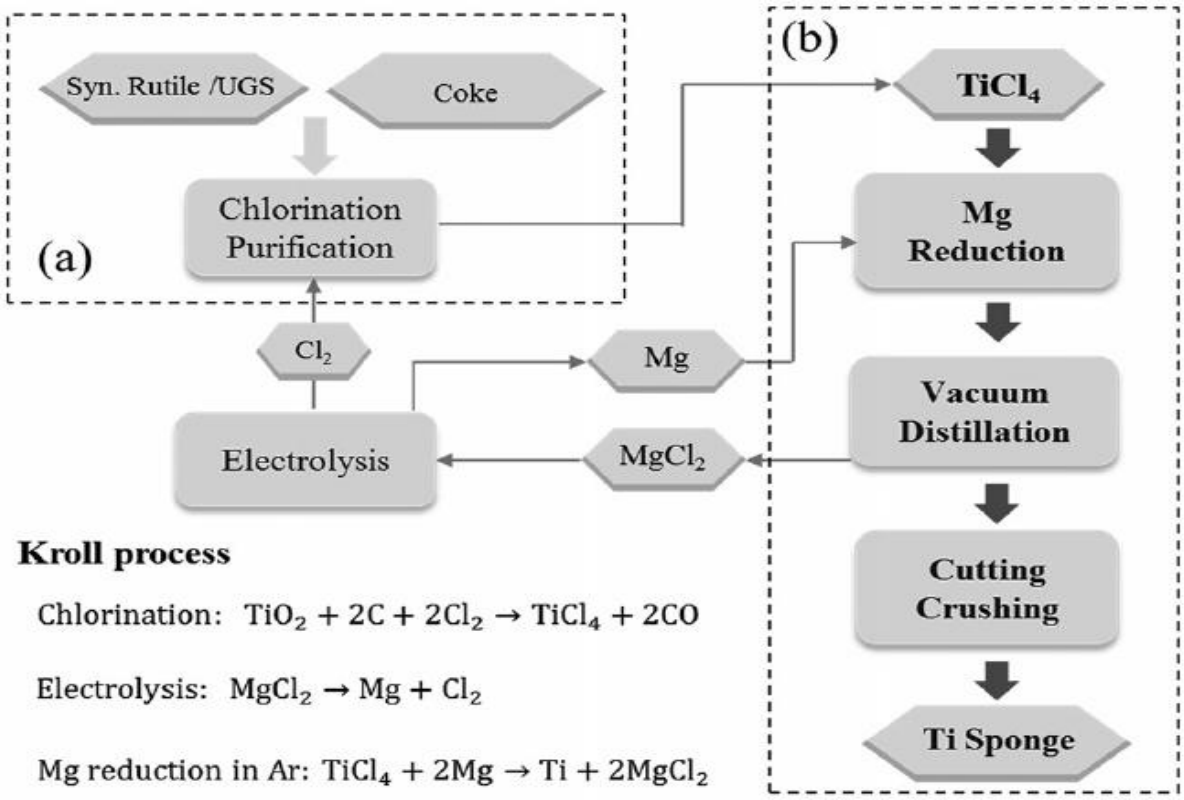

Figure 22. The major processing steps of the Kroll process [11]

In the Kroll process, TiO_2 slag is first chlorinated with the aid of petroleum coke in a fluidised bed to produce raw $TiCl_4$. Before the introduction to the reducing agent, the raw TiCl4 needs to be refined through distillation to remove any impurities, such as iron chloride (FeCl3) and vanadium chloride (VCl4), that may affect the purity of the metallic Ti. Since the impurities have a higher boiling point than the $TiCl_4$, the mixture of the TiCl4 and its impurities is heated to the boiling point of the $TiCl_4$ at which it is vaporised and condensed into a separate chamber. After refinement, the $TiCl_4$ is then poured into molten Mg inside a stainless-steel reactor. The reaction then reduces $TiCl_4$ to Ti by forming $MgCl_2$, resulting in the nucleation of Ti sponge. The Ti sponge continues to grow from the bottom of the reactor and from inside the reactor walls. The $MgCl_2$ and the Mg vapour formed during the process is recovered and sent through electrolysis for separation. During electrolysis, the Mg and Cl are separated

and the Mg is channelled back into the molten Mg stage while the Cl_2 is channelled back into the chlorination stage [11], [90], [91].

The Ti sponge has unwanted $MgCl_2$ contamination due to the reduction process. Distillation in a vacuum is required to remove these contaminants. The distillation temperatures can range from 800 to 1000 °C, and the process lasts several days. Due to the high temperatures and long distillation times, the energy consumption of the distillation process can amount to 70% of the total energy consumed by the Kroll process. Therefore, it can be said that the cost involved in purifying the Ti sponge is one of the driving factors behind the high cost of the Ti metal [11], [91].

2.4.2.3 TIRO process

The TIRO process, diagrammatically shown in Figure 23, is a process that employs thermo-mechanical principles that are similar to the Kroll process to produce Ti powder from $TiCl_4$ [91], [94]. This process was developed by the Commonwealth Scientific and Industrial Research Organization (CSIRO) as an attempt to directly produce titanium powder at a lower cost than the powder production route based on the Kroll process [94].

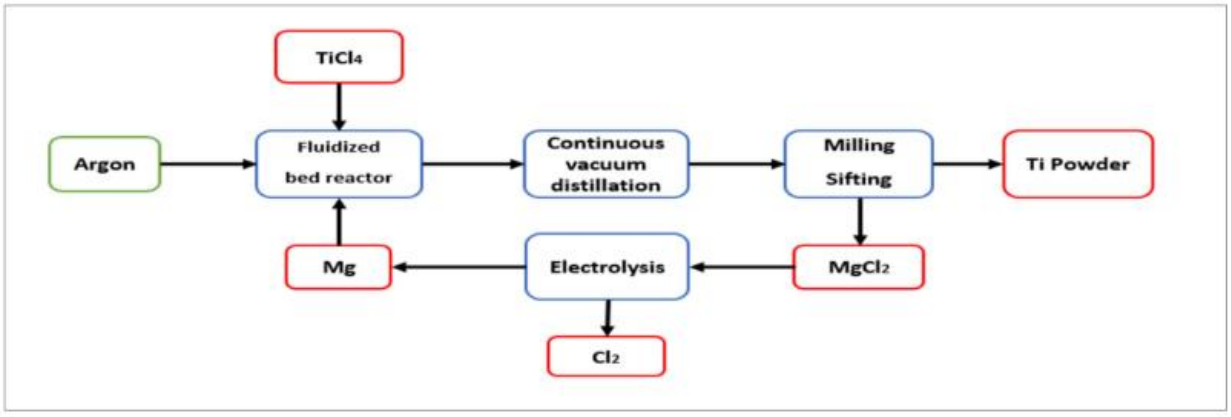

Figure 23. CSIRO Tiro Process [91]

The TIRO process is based on the metallothermic reduction of $TiCl_4$ using Mg in a powder form as the reducing agent and Ar as a carrier gas in a heated fluidised bed reactor. Pre-formed Ti, alumina or silica powders are usually pre-placed into the reactor, and they act as a substrate on which the Ti agglomerates during the reaction

[94]. The $TiCl_4$ (in gaseous form) and Mg powder (gaseous or solid) are continuously injected into the reactor, and they react to form solid Ti particles and a liquid phase $MgCl_2$ compound. The Ti particles are then separated from the $MgCl_2$ compound through a vacuum distillation process. The $MgCl_2$ compound is vaporised and condensed separately and further separated through electrolysis to recover the Mg [91]. The major advantage of this process over the Kroll process is the energy savings through by-passing the Ti sponge production stage of the Kroll process by directly producing spherical or irregularly shaped Ti powder [11], [91], [94]. The CSIRO has since collaborated with Coogee Titanium, which led to the commercialisation of this process at their plant in Kwinana, Perth, in 2021 [95].

2.4.2.4 Armstrong process

The Armstrong process (Figure 24) was developed based on the same chemistry as the Hunter process with the aim of decreasing the cost associated with the Hunter process by the direct continuous production of Ti powder instead of Ti sponge as in the Kroll and Hunter processes. This process was designed to run continuously to produce Ti powder, and it was considered an improvement of the Hunter process [11], [91].

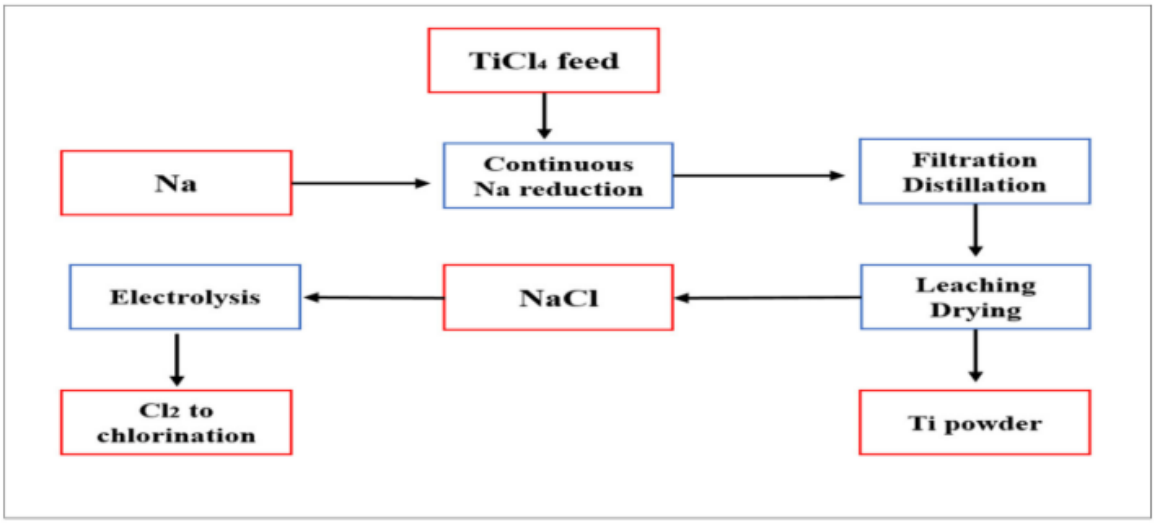

Figure 24. Armstrong process flow diagram [91]

In this process, a stream of Na is pumped into a reactor, where it reacts with gaseous $TiCl_4$. The Na reacts with Cl to form NaCl, resulting in the formation of Ti powder. The

excess Na is filtered out and pumped back into the system. The remaining mixture of NaCl and Ti powder is leached and dried to remove the NaCl, and the Ti powder as a product of this process can be collected [11], [96]. The Armstrong process has been commercialised. However, it has not been adopted for full-scale Ti powder production due to the cost (similar to Kroll) and the morphology (coral-like) of the powder [89].

2.4.2.5 The CSIR Ti production process

The Council for Scientific and Industrial Research (CSIR) in South Africa developed a continuous Ti powder production process, shown in Figure 25, that utilises molten salts such as MgCl and CaCl as reducing agents to produce Ti metal powder from the reduction of $TiCl_4$ [12], [97].

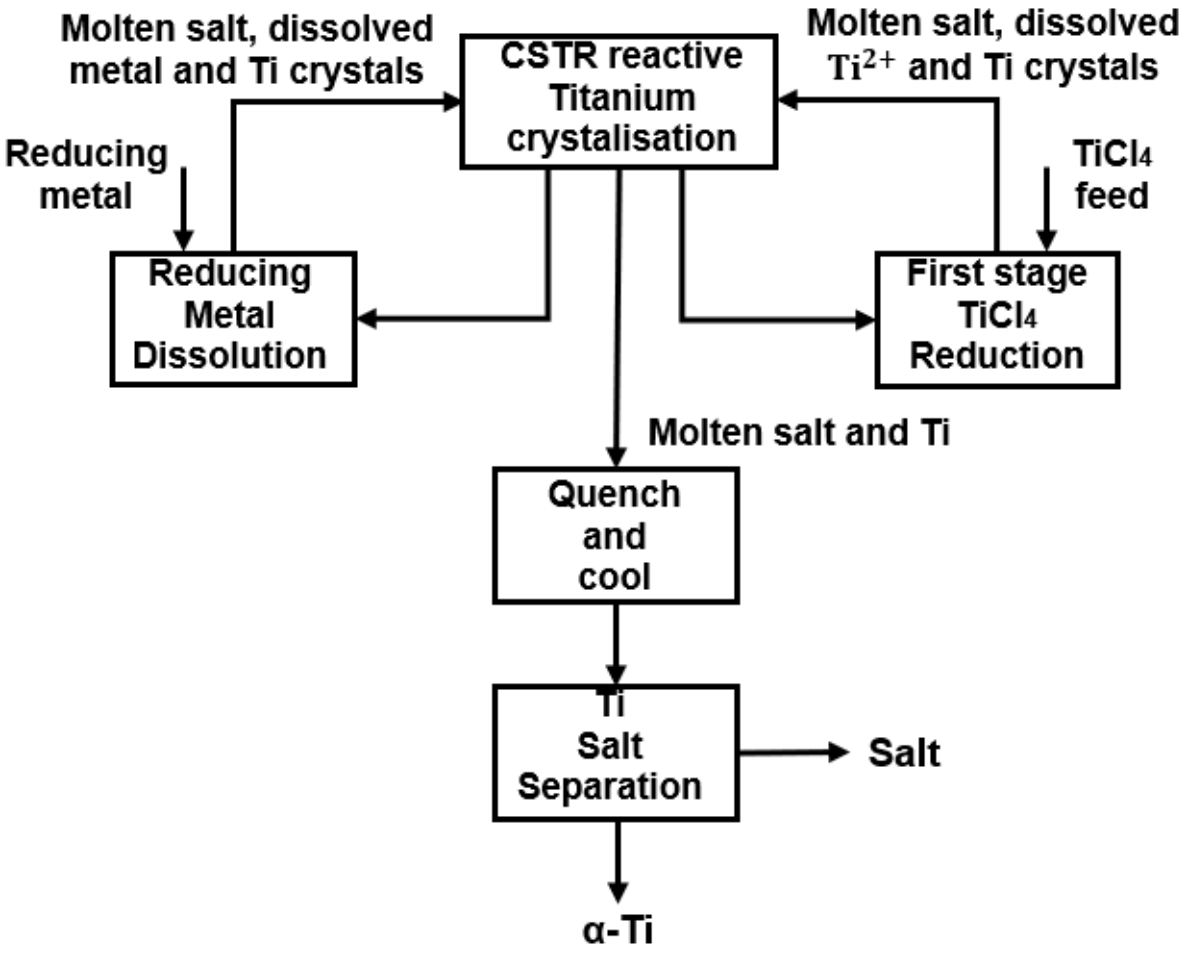

Figure 25. The CSIR Ti powder production process (adapted from) [12]

The reactor in which the reduction occurs contains a molten salt solution (MgCl or NaCl) that acts as a host, ensuring a controlled environment for the reduction. Gaseous $TiCl_4$ is injected into the reactor, followed by the reducing agent, and the reduction reaction occurs resulting in the formation of fine metallic Ti powder and either $MgCl_2$ or $CaCl_2$ as a by-product, depending on the reducing agent used. During the separation stage, the Ti can be obtained either through filtration, or the Ti-containing solution can be channelled to a cooling stage where the salt medium is solidified and cooled. The solid-state mixture of Ti powder and salt is then separated in a different stage through distillation, and the salt is channelled into an electrolysis system to recover the reducing material and Cl_2 [12], [89], [98].

The CSIR-Ti process is currently in its pilot plant phase; therefore, it has not yet been commercialised. [12]. While this process has an advantage over the Kroll and Hunter processes due to its direct Ti powder production, which is suitable for use in PM and AM systems, there are still some challenges that are delaying the commercialisation of this process. It has been reported that the efficiency of this process is negatively affected by the formation of unwanted by-products, such as $TiCl_2$ that tend to block the feed lines. In addition to $TiCl_2$, the blockages were also a result of Ti powder lumps that formed prematurely outside the intended Ti powder zone due to the high reactivity of the reduction reaction[12], [97].

2.5 Titanium and titanium alloys

Commercially pure (CP) Ti is the lowest strength but also the most corrosion-resistant form of the metal and its alloys [89], [99]. There are different grades of CP Ti, which are graded according to the content of the interstitial elements, such as oxygen and iron, that are present in the metal [6]. The strength of the Ti metal increases as the content of the interstitial elements (oxygen, nitrogen, and iron) increases. Ti grades that are purer and consist of fewer interstitials will exhibit lower values of strength and hardness [6]. The properties of this metal can be improved by designing a particular alloy, depending on the target application and properties, by adding alloying elements. The addition of different elements to the Ti metal has implications and yields different results in terms of composition, microstructure, and mechanical properties. An understanding of the different effects of the alloying elements on the Ti metal is essential and can be accomplished by studying the Ti phase diagram [6].

2.5.1 Titanium alloy phase equilibrium diagram

A phase diagram can be considered as a guideline for all possible alloy relationships in an alloy system [6]. The phases present in an alloy system, as well as the relationship between those phases, can be represented by a phase diagram. A pseudo-binary titanium phase diagram showing the different phases present in Ti alloy systems represented as a function of the temperature and the amount of beta-phase stabilizing elements is shown in Figure 26 [6]. The most common Ti alloys can also be seen in this diagram, where they are placed in their respective phases according to the alloying elements present in that particular alloy.

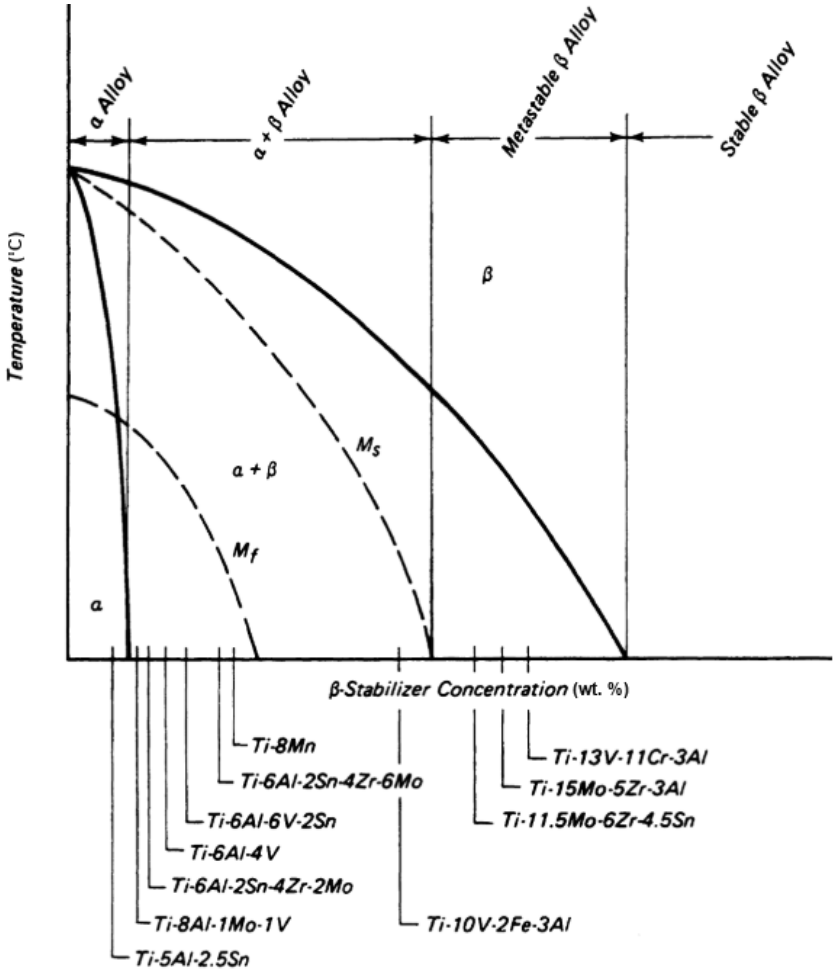

Figure 26. Pseudo-binary phase diagram of the Ti metal alloy system [6]

The alloying elements used in the design of Ti alloys can be classified as either α-phase stabilisers, β phase stabilisers or neutral elements, depending on the effect they have on the β-transus temperature [1], [6], [100] Figure 26 shows that Ti alloys

can be classified into three distinct groups according to the phases present in the alloy. A Ti alloy can either be an alpha (α), alpha-beta (α+β), or beta (β) phase alloy, depending on the elemental composition of the alloy [1], [6]. The α phase can be further subdivided into “pure α” and “near-α” alloys, while the β phase is subdivided into “metastable β” and “stable β” alloys. The temperature at which the α phase or α+β phase transforms to the β phase is known as the β-transus temperature. This temperature is different for all Ti alloys. It is important to identify the β-transus temperature of the particular alloy as heat treatment processes are usually carried out with respect to the β-transus temperature [84].

The α phase consists of an HCP crystal structure in which the atoms are closely packed, hence the high strength and relatively lower ductility of pure Ti and α-Ti alloys in comparison to α+β and β alloys [1], [6]. Annealing heat treatments can be used to improve the properties of α-Ti alloys to a certain degree, as α-Ti alloys are not as responsive to heat treatment compared to α+β and β alloys [6]. Heat treatment processes, such as annealing, rely on the refinement of the microstructure through phase transformations from α to β phase [100]. Since α-Ti alloys such as Ti-5Al-2.5-Sn are single-phase alloys, it is not possible to obtain α to β-phase transformations, limiting the extent to which heat treatment processes can improve the properties of the alloy. The addition of a small amount of β-phase stabilizing elements will result in a slightly heat-treatable near-α alloy. Near-α alloys contain a small amount (1–2 wt.%) [101] β-phase stabilisers such as Mo, V and Nb, allowing for a limited phase transformation during heat treatment, resulting in a slightly noticeable improvement in the alloy reaction to heat treatment compared to α-Ti alloys [102]. The most used alloy phase, due to its composition group, is the (α+β) alloy group. These alloys consist of a mixture of both α- and β-phase stabilizing elements with a β-phase stabiliser volume consisting of 5 to 10 wt.% of the total volume of the alloy [6], [101]. Due to the presence of a significant amount of β-phase stabilisers in α-β alloys, these alloys are highly responsive to heat treatment as it is possible to obtain α to β-phase transformations upon heating. Depending on the alloy composition and the heat treatment temperature, α+β alloys can transform to a 100% β phase during heating and transform back to α+ retained or transformed β during cooling, resulting in a good mixture of strength and ductility [6]. An increase in the volume fraction of the β-phase stabilizing elements will result in metastable β alloys. These alloys consist of a

minimum β-phase stabiliser volume fraction between 25–30 wt.% of the total volume of the alloy [103]. These alloys will retain the β phase formed at high temperatures during cooling and result in a heat-treated alloy consisting of a small amount of α phase and a majority of retained β phase at room temperature. The stable β-phase alloys such as Ti-13V-13Cr-3Al, Ti-13Nb-13Zr and Ti-30Mo are at the end of the spectrum of the Ti-alloy phase diagram as they have a volume of 100% β phase, which is retained at room temperature after heat treatment [104], [105].

2.5.2 Effect of alloying elements

The most common elements that act as α-phase stabilisers are aluminium (Al), oxygen (O) and nitrogen (N). These elements stabilize and favour the α phase by raising the β-transus temperature of the alloy. β-phase stabilisers, on the other hand, are elements such as vanadium (V), molybdenum (Mo), tantalum (Ta) and copper (Cu), and they tend to improve the stability of the β phase in the microstructure of the alloy at lower temperatures. The β-phase stabilisers can either be β isomorphous (V, Mo and Ta) or β eutectic (Fe, Mn, Cr and Cu) [6]. β-isomorphous elements have a high solubility in Ti, therefore eliminating the chances of intermetallic compounds forming in the alloy. β-eutectic elements, on the other hand, have a very low solubility in Ti and may result in the formation of eutectic intermetallic compounds. The neutral alloying elements are elements such as tin (Sn) and zirconium (Zr), which have nearly no effect on the β-transus temperature [6].

Existing literature based on the effect of the alloying elements on the Ti metal has provided insight into how the alloying elements can be added to the Ti metal to develop or improve certain properties of the metal [1], [6]. To achieve sufficient oxidation resistance, an addition of niobium (Nb) of not more than 2 at% will provide the required material property. To increase the strength of the alloy, the content of Al in the alloy should decrease. However, this will affect the alloy's ductility and resistance to corrosion. Creep resistance can be improved by the addition of tungsten (W), silicon (Si), and molybdenum (Mo) at a concentration of not more than 2 at%. Lastly, to stabilise the microstructure of the alloy during high-temperature operation, boron (B) can be included as an alloying element as it can refine the alloy grains, making it a suitable alloying element for high-temperature alloys [6].

2.6 Ti6Al4V alloy

The Ti6Al4V alloy is a two-phase (α+β) alloy consisting of both the α and β phases at room temperature [6], [57]. Essentially, the Ti6Al4V alloy has a composition (wt.%) consisting of 90% Ti, 6% Al and 4% V. However, interstitial elements Fe, N, H, O, etc., are always present in the produced alloy. Depending on the concentration of these elements within the Ti6Al4V alloy, they can either have a positive (e.g. increased strength) or negative (e.g. induce brittleness) effect on the quality of the alloy if their concentration within the alloy exceeds a certain threshold [105], [106]. The ASTM standard F3001-14 [107] specifies the maximum allowable concentration of interstitials in LPBF-produced Ti6Al4V(ELI) parts. The parts that conform to this standard are considered to be extra-low interstitial (ELI) parts that possess mechanical properties comparable to forged and wrought parts and can be used in applications such as the aerospace, medical, and cryogenic applications [108]. Another ASTM Ti6Al4V standard (Table 1) that is less strict on the concentration of the O, Fe, and H interstitial elements is ASTM F2924-14. [109]. Parts that conform to this standard can be used in less critical applications where the interstitials present in the alloy do not have a negative effect on the mechanical properties required for the intended application. Table 1 gives the standard compositions for LPBF-produced Ti6Al4V (ELI) and the lower purity Ti6Al4V alloy [107], [109].

Table 1. A comparison between the ASTM standard specifications for the chemical composition of LBPF Ti-6Al-4V [107], [109]

	Element (wt.%)									
Standard	**Al**	**V**	**Fe**	**O**	**C**	**N**	**H**	**Y**	**OTHER**	**Ti**
ASTM F3001-14 (ELI)	5.5 – 6.5	3.5 - 4.5	0.25	0.13	0.08	0.05	0.012	0.005	0.1 (ea.) 0.4 (tot.)	Rem.
ASTM F2924-14	5.5 – 6.75	3.5 – 4.5	0.3	0.2	0.08	0.05	0.015	0.005	0.1 (ea.) 0.4 (tot.)	Rem.

The Al in this alloy acts as an α-phase stabiliser, therefore increasing the α-phase retained at room temperature by increasing the β-transus temperature of the alloy,

while the V acts as a β-phase stabiliser [6]. A pseudo-binary phase diagram showing the effect of the addition of V to the Ti6Al alloy is shown in Figure 27.

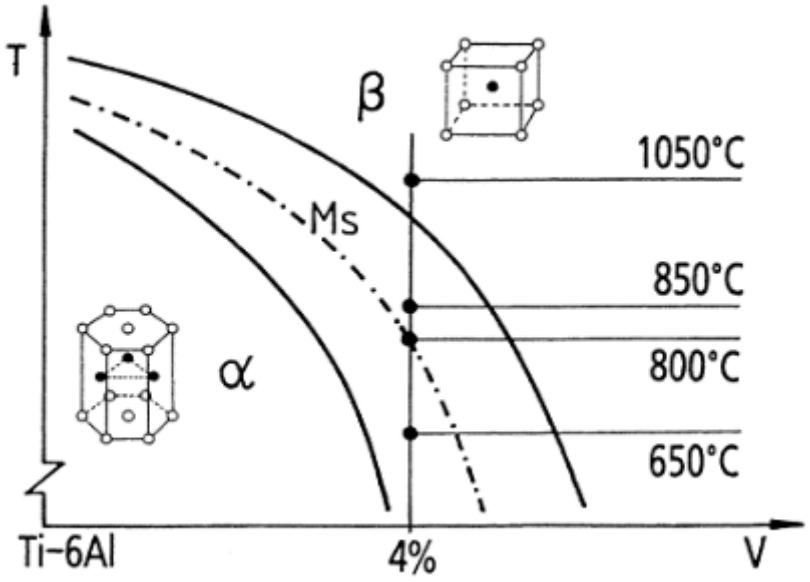

Figure 27. Ti6Al phase diagram illustrating the phases at different temperatures for at 4% V content [110]

This phase diagram is represented as a function of the relationship between temperature and the volume content (wt.%) of V, where the Ti6Al4V is represented as black points at different temperatures. At room temperature, the Ti6Al4V alloy is seen in the α+β two-phase region, with the α-phase dominating the microstructure of the alloy. As the temperature increases, the concentration of β-phase increases until the microstructure consists purely of β-phase grains [1], [6].

2.6.1 Ti6Al4V microstructures and mechanical properties

The term “microstructure” refers to the arrangement, size and orientation of the grains present in a metallic component at a microscopic level [6]. The behaviour and properties of any metallic material are directly related to the microstructure of the metal. Depending on the type of manufacturing process used to produce the Ti6Al4V alloy, the microstructure can either be of an equiaxed, martensitic or lamellar type [84]. These Ti6Al4V microstructures can be obtained and manipulated through

various heat-treatment processes to alter the mechanical properties of the alloy for certain application [61], [84], [105].

2.6.1.1 Wrought alloy Ti6Al4V

The term “wrought alloy” refers to an alloy that has been produced through high temperature (as high as 1 100 °C [111]) thermomechanical processes such as forging, extrusion and rolling [1]. The process of producing wrought Ti6Al4V alloy parts starts with the production of an ingot through the vacuum arc remelting (VAR) process [1]. In VAR, Ti sponge is poured into a chamber and blended with the alloying elements (Al and V) at the correct ratio to ensure compositional accuracy and then compacted to form a consumable electrode. The consumable electrode is then melted by an electric arc under vacuum into a copper crucible in which the molten Ti6Al4V alloy solidifies, forming an ingot. The microstructure of the ingot consists of a mixture of coarse α+β grains, which are generally known to have lower mechanical properties in comparison to finer-grained microstructures. The ingot is then used as the starting feedstock in the thermomechanical process, where the coarse microstructure is transformed into a finer microstructure, resulting in improved mechanical properties [89]. For this reason, wrought Ti6Al4V has become the standard alloy compared to other Ti6Al4V alloys that different manufacturing routes have produced.

Wrought Ti6Al4V has a microstructure which consists of equiaxed α grains with β-phase grains at the α-phase grain boundaries (Figure 28) [1], [84], [112]. The mechanical properties of wrought Ti6Al4V can be improved through the refinement of the grains. In Figure 28, the α phase appears as the lighter phase, while the β-phase is the darker phase on the α-phase grain boundaries. The β phase amounts to about 10% of the phases present in this alloy and heat-treatment-based refinement is required.

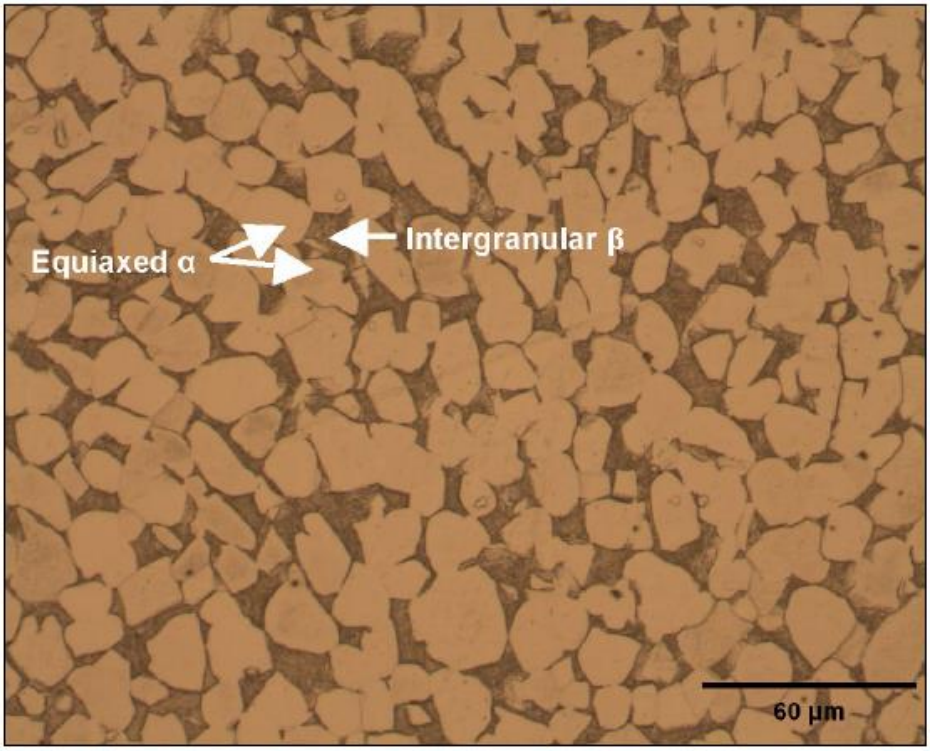

Figure 28. The microstructure of wrought Ti6Al4V [112]**.**

Typical mechanical properties of wrought Ti6Al4V are presented in Table 2 [84] and compared to those of AB DMLS Ti6Al4V parts. There is not much of a difference between the yield and tensile strengths of wrought Ti6Al4V. Additionally, when compared to the DMLS-produced Ti6Al4V, wrought Ti6Al4V has a relatively higher ductility due to its uniform, equiaxed microstructure. Therefore, it can be said that the wrought production route is able to produce an alloy with excellent mechanical properties.

Table 2. Comparison between typical mechanical properties of wrought Ti6Al4V alloy

Mechanical property	Wrought parts	DMLS AB parts
UTS (MPa)	1 006 [84]	1 155 [61]
YS (MPa)	960 [84]	1 110 [84]
%ϵ (% elongation)	18.37 [84]	7.28 [84]

2.6.1.2 DMLS produced Ti6Al4V

In recent studies [57], [72], [113], it has been reported that the AB Ti6Al4V alloy parts produced by the DMLS process consist of an acicular martensitic (α'-phase) microstructure (Figure 29) [61], [84], [113]. This microstructure forms when the material is cooled at cooling rates that are higher than 410 °C/s resulting in a beta-to-martensite transition [84]. The AB acicular martensitic microstructure is unfavourable because it results in parts that have high strength and low ductility, which can only be improved by post-production heat treatments [61].

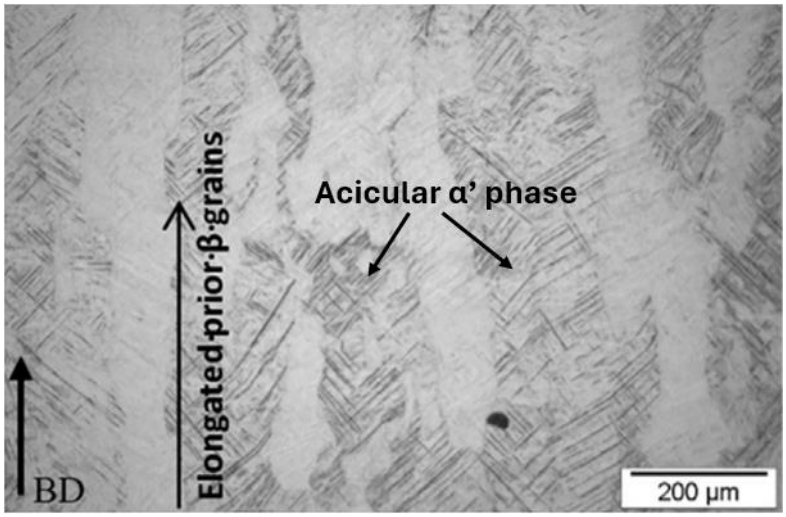

Figure 29. The AB acicular martensitic microstructure of DMLS-produced Ti6Al4V parts [113]

The mechanical properties of AB DMLS Ti6Al4V parts are shown in Table 2 [61], [84], [105]. From this table, these parts exhibit high values of yield strength (YS), ultimate tensile strength (UTS) and relatively low ductility. This is due to the fine acicular microstructure that is caused by the rapid cooling rate in the DMLS process, which results in parts with a poor strength-to-ductility ratio [84]. This strength-to-ductility trade-off problem can be resolved by improving the ductility of the Ti6Al4V parts through specifically designed post-process heat treatments [72].

2.6.2 Heat treatment of Ti6Al4V alloys

Heat treatment processes are usually applied to Ti and its alloys to relieve residual stresses developed during manufacturing or to improve specific properties such as fatigue properties and high-temperature creep strength [6], [84]. In the case of the Ti6Al4V alloy, the mechanical properties of this alloy are improved by heat treating the alloy at a temperature close to or above the β-transus temperature (995 °C) [84], transforming the microstructural grains of the alloy upon cooling to room temperature [72]. For Ti alloys, any heat treatment above 427 °C should be performed in an inert gas atmosphere such as argon (Ar) to avoid the embrittlement of the alloy's surface due to high-temperature oxidation [6]. This embrittlement is caused by the diffusion of oxygen into the solid solution of the Ti alloy when the heat treatment is carried out at elevated temperatures in a non-inert gas atmosphere. Since O is an α-phase stabiliser, an α phase develops on the surface of the part being heat treated to form a relatively brittle alpha case, resulting in reduced fatigue properties [6].

Heat treatment processes are highly dependent on the starting microstructure of the part to be heat-treated [84]. In turn, the microstructure is dependent on the type of process used to produce the part. Standard heat treatment procedures for wrought Ti6Al4V parts will not yield the same results when applied to DMLS-produced Ti6Al4V parts [61], [84], [114]. Conducting a microstructural analysis on any part to be heat-treated is essential for understanding the starting microstructure and determining the appropriate treatment process needed to achieve the desired results.

2.6.2.1 Microstructural evolution of DMLS Ti6Al4V alloy during heat treatment

Due to the rapid cooling rate (up to 10^8 K/s [57]) found in the DMLS process, the volume content of the AB Ti6Al4V alloy is made up of a martensitic α-phase (90%) at room temperature. The physical and mechanical properties that dominate this alloy are typical of a part that consists of this kind of microstructure [6], [84]. When this alloy is heated at a temperature below its β-transus temperature of 995 °C, the martensitic α-phase starts transforming into a lamellar microstructure at the grain boundaries, and the increased heat energy activates the V atoms, leading to the formation of the β phase at the α-phase grain boundaries [84]. The initial needle-like,

martensitic α-phase microstructure (Figure 29) is then transformed into a dual-phase microstructure that consists of a lamellar structure consisting of the α and β phases. This kind of lamellar microstructure can be identified with needles similar to those of the original martensitic α-phase microstructure, with the difference being that the lamellar microstructural needles are broader and consist of the two α and β phases. These phases compete for dominance, with the β-phase grain growth limited at temperatures below the β-transus temperature. At the same time, it grows with less resistance as the temperature approaches the β-transus temperature. Higher temperatures close to the β-transus temperature will result in the coarsening of the α phase during slow cooling, resulting in a decrease in the strength accompanied by an increase in ductility of the alloy. This increase in the α-grain width can be seen in Figure 30 [114], which shows that the α grains become wider during the heat treatment at higher temperatures. It can be said that heat treating below the β-transus temperature results in a good trade-off between the strength and ductility of the Ti6Al4V alloy. It has been reported that heat treating at temperatures of 850, 940 and 947 °C (below β-transus) followed by slow cooling in air yielded the best results for DMLS-producedTi6Al4V [61], [84], [114].

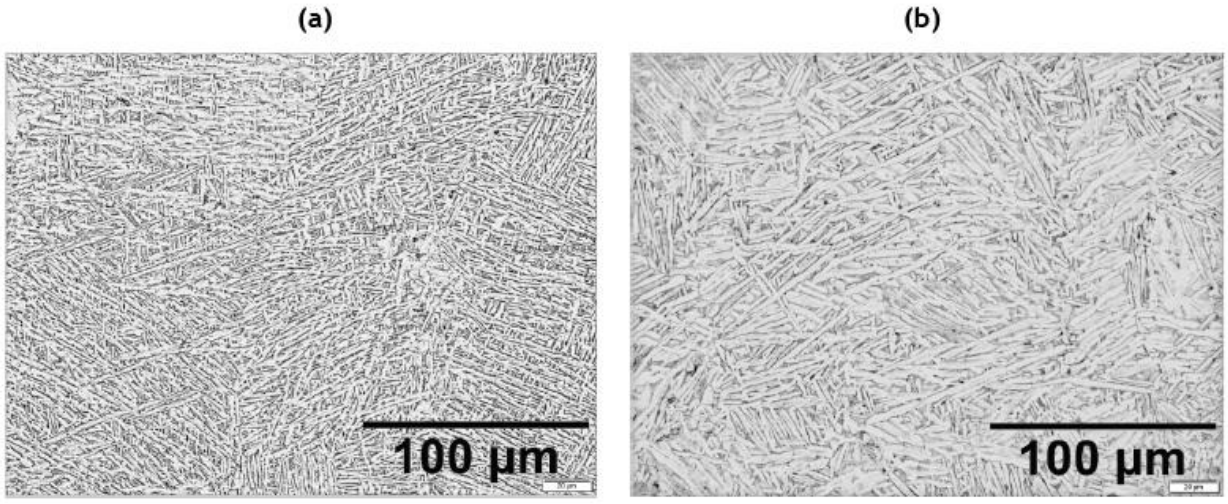

Figure 30. Microstructural evolution of DMLS Ti6Al4V for temperatures below the β-transus temperature (a) 828 °C and (b) 878 °C for a holding time of four hours [114]

When the Ti6Al4V alloy is heated to a temperature above its β-transus temperature of 995 °C, the β-phase grains grow rapidly, resulting in a fully uniform, single-phase microstructure that consists of β-phase grains [84], [114]. Since the Ti6Al4V alloy consists of only the β phase at temperatures above the β-transus, the heat treatment temperature should not be excessively higher than the β-transus temperature to avoid superabundant grain growth that can easily occur due to the absence of the competing α-phase grains [61]. During cooling from the 100% β phase, the α phase is precipitated as fine, needle-like plates (laths) that grow along the planes of the BCC crystal structure within the dominant β-phase grains. The resulting microstructure is an α-Widmanstätten (basket-weave) microstructure, which has been transformed from the starting martensitic α' microstructure. This microstructure can be identified by lamellar α laths that are arranged in a pattern similar to a basket-weave, as shown in Figure 31 [115].

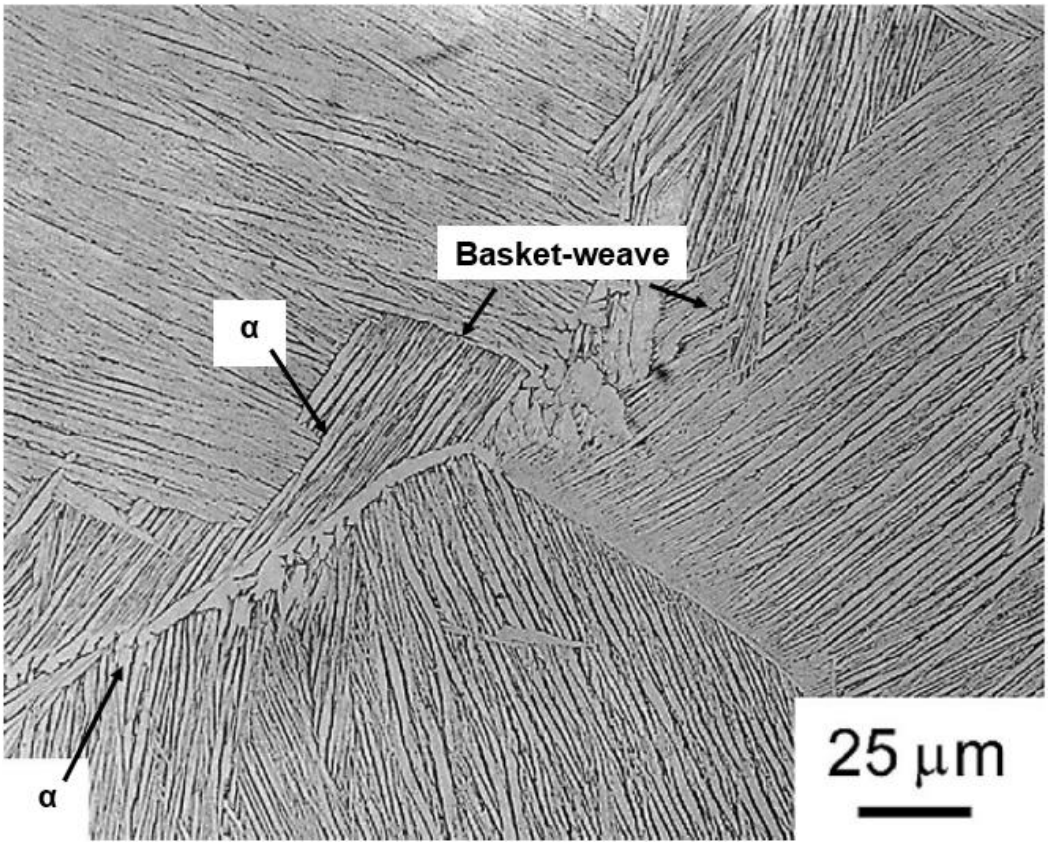

Figure 31. Ti6Al4V α-Widmanstätten microstructure formed upon furnace cooling from β phase. The lighter grains represent the transformed α phase, while the β-phase grains appear darker [115]

The cooling rate is a crucial factor to consider when cooling from a temperature above the β-transus temperature because the quantity of the α phase that forms after cooling is dependent on the cooling rate [84]. A high cooling rate, such as in quenching, will result in undercooling, which causes the formation of multiple α-phase nuclei, ultimately leading to the formation of smaller α-phase colony sizes. A small colony-size phase results in a finer microstructure, and such microstructures are known for their high strength, compromised creep resistance, and fatigue strength [116]. Moderate cooling rates, such as those found in air cooling, will result in the formation of an α-Widmanstätten (basket-weave) microstructure. Furnace cooling provides a low cooling rate, which allows the formation of a lamellar mixture of the α and β phases with an increased α-phase colony size [61], [85], [100].

Similar to the cooling rate, the effect of the residence time of the Ti6Al4V alloy at high temperatures during heat treatment is more noticeable for temperatures above the β-transus. Longer residence times tend to lead to larger phase grains, resulting in larger colony sizes and the subsequent optimum combination of strength and ductility. In general, when heat treating the Ti6Al4V alloy at high temperatures (high-temperature annealing), it is expected that the strength of the alloy will decrease and the ductility will increase [85], [86], [115].

2.7 Production of pre-alloyed Ti6Al4V powder for additive manufacturing

In MAM, the metal powder feedstock used to produce parts is vitally important. The type of powder feedstock used has a significant influence on the resulting mechanical properties of the part. The most-used metal powder in AM is of a pre-alloyed (PA)-type [8]. In a PA powder such as Ti6Al4V powder feedstock, each individual powder particle has the same alloy composition as the Ti6Al4V alloy [6]. This kind of powder is usually produced from wrought or cast Ti6Al4V raw materials. However, meltless processes such as the hydrogenation-dehydrogenation (HDH) and plasma spheroidisation (PS) processes that do not depend on wrought or cast raw materials to produce PA powders have been developed [96]. PA Ti6Al4V powder is highly sought after for its ability to produce parts with the required chemical composition and excellent mechanical properties that are comparable to those of cast or wrought-produced parts [6]. The processes used to produce pre-alloyed powder are often

cost-intensive, resulting in expensive final parts [6]. These processes will be discussed in the following headings.

2.7.1 Gas atomisation

The gas atomisation (GA) process, shown in Figure 32 below was developed by Crucible Materials Corporation in 1988 [89].

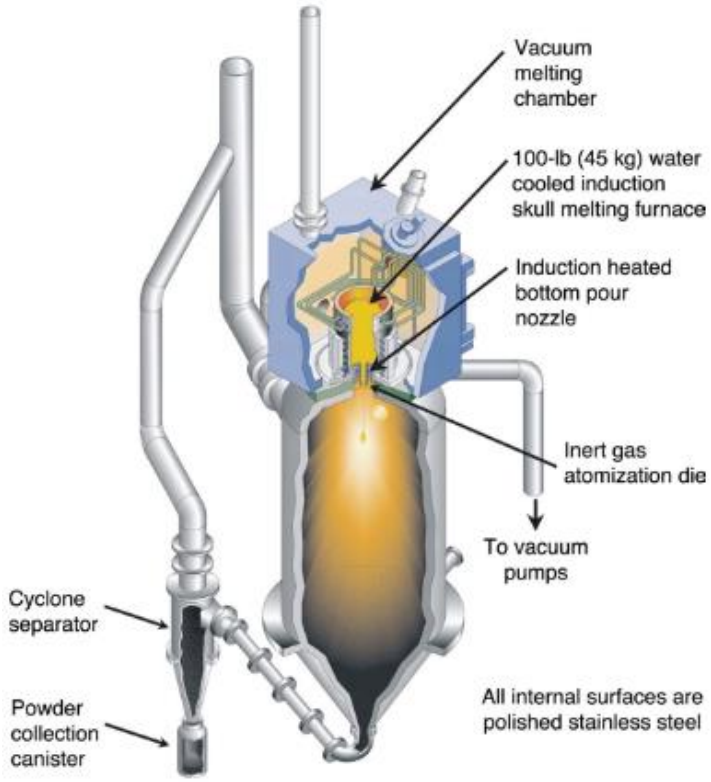

Figure 32. A gas atomisation system [89]

The production of spherical PA powder from the gas atomisation process begins with the introduction of solid PA metals, such as ingots and bars, as starting materials [89], [96]. The starting material is induction-melted in a water-cooled skull crucible in a vacuum. The molten metal is held in its molten state for a period (retention time) to allow complete homogenisation of the alloying elements in the bulk of the molten metal. The retention time is usually between 30–40 minutes, depending on the chemistry of the alloy; however, the metal should not be kept in its molten state for too long to avoid infiltration of impurities during homogenisation. After homogenisation, the molten metal flows into an induction-heated metal nozzle, which creates a concentrated stream of molten metal. The molten metal stream then flows

through the centre of a ring of high-pressure inert gas jets that atomise the metal stream into tiny droplets, which rapidly transform into solidified spherical metal powder particles upon cooling and solidification. As the atomisation gas is recycled from the bottom of the chamber into the system, it carries the metal powders, which are dropped into a collection canister via a cyclone separator [89], [117].

The GA process is the most-used atomisation process in the production of PA powders for AM. This is mainly due to its spherical-shaped powders, which give the feedstock good flowability and powder-packing density [13]. Good flowability means that it takes less than 35 seconds for 50 g of the powder to pass through the Hall flow meter while a good packing density generally ranges between 50 to 60% relative to the theoretical density of the material [118]. The high-pressure gas atomisation results in a turbulent molten metal spray plume consisting of droplets of varying sizes. Due to the low thermal mass of the smaller droplets in the spray plume, the smaller droplets remain in their molten state longer than the larger droplets. The turbulence within the spray plume results in multiple collisions between the molten-state smaller particles and the solidified larger particles, resulting in the production of spherical powders that have smaller spherical powders attached (satellites) on their periphery [89]. The main disadvantage of AM powders produced through the GA process is the occasional formation of satellited particles, which negatively affects the flowability of the powder. Additionally, this powder can contain traces of the high-temperature ceramic coating used on the induction coils and in the cavity of the spray nozzles. The use of skull melting to prevent contact between the molten metal and possible contaminants can minimise contamination during the melting stage [96]. For Ti6Al4V PA powder, the allowable ceramic impurity level has been specified together with other impurities in the ASTM F3001 and F2914 standards (Table 1) [107].

2.7.2 Plasma atomisation

The plasma atomisation process was invented by Pyrogenesis (Canada) in 1995 [119]. Plasma atomisation is an uncomplicated process that uses PA wire as the starting material to produce PA powder. PA powder is formed when the PA wire is fed into the apex point of two or more adjacent plasma torches [89]. When the wire comes into contact with the arcs created by the high-velocity plasma torches, it melts and breaks into droplets that solidify during their gravity-induced fall in an argon gas

atmosphere, resulting in highly spherical, chemically pure PA powders. The type of plasma used in this process can either be a DC or a high-frequency induction arc [96].

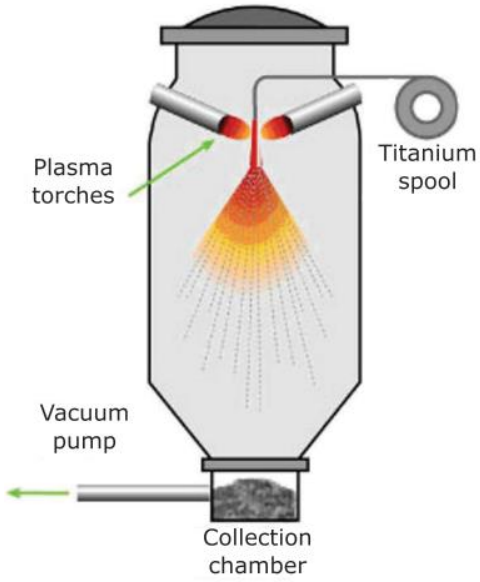

Figure 33. Schematic of the plasma atomisation process [119]

In comparison to the GA process, the PA process exhibits greater control over the powder production process. The plasma torches do not induce as much turbulence into the system compared to the high-pressure gas used in the GA process. As the molten droplets formed are of a constant size (narrow PSD), the solidification rate is the same for all the molten droplets. The powder is satellite-free as there are fewer particle collisions and agglomeration due to the absence of severe turbulence and the even solidification mechanism typical of this process [11], [89], [96].

2.7.3 Rotating electrode-type processes

Rotating electrode-type processes make use of a heat source to melt a rotating consumable metal electrode consisting of a PA feedstock [6]. The spherical PA powder production in these processes relies on the centrifugal force resulting from the consumable electrode that is rotated at speeds up to 15 000 rpm. There are two types of rotating electrode powder production processes, namely the rotating electrode process (REP) and the plasma rotating electrode process (PREP) [89].

In the REP (Figure 34), a non-consumable tungsten electrode arc is used to melt the rotating feedstock cathode. Due to the centrifugal force created by the rotation, the molten droplets are rapidly ejected from the cathode, and they solidify in flight from the cathode to the powder collection tub at the bottom of the chamber. This process produces spherical powder with a size distribution of between 50 to 100 µm; however, the powder has been reported to contain traces of contaminants that originate from the tungsten heat source [6], [96].

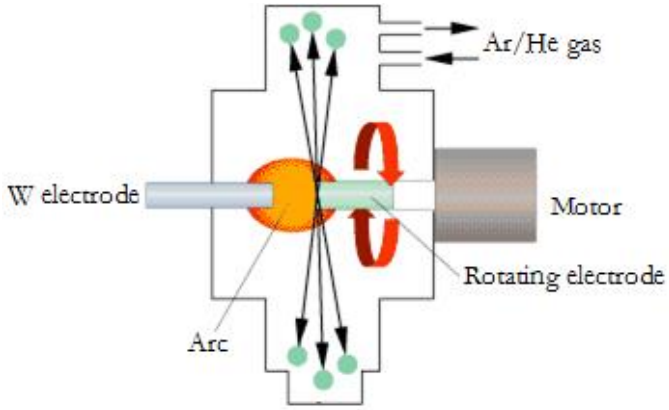

Figure 34. Rotating electrode process [120]

The PREP (Figure 35), developed by Starmet in 1988, is considered an unsullied version of the REP [89], [96]. In this process, the tungsten heat source, which caused contamination in the REP-produced powders, was replaced with a transferred arc plasma torch to ensure that no contaminants were transferred to the powder [96]. Like the REP, PREP also relies on centrifugal atomisation to produce powder. The process takes place in a stainless-steel chamber wherein a plasma arc is used to melt the alloy from the rotating PA feedstock. As the feedstock is melted, molten alloy droplets are ejected and rapidly cooled in an argon or helium atmosphere before dropping to the bottom of the chamber. This process has a dual advantage over other atomisation processes. Firstly, this process can produce powders with a composition that is close to the desired alloy chemistry because of the limited amount of contamination possible during production. Secondly, powder particles cannot form agglomerates or irregular shapes due to the limited contact with each other in their molten phase during atomisation [89], [96].

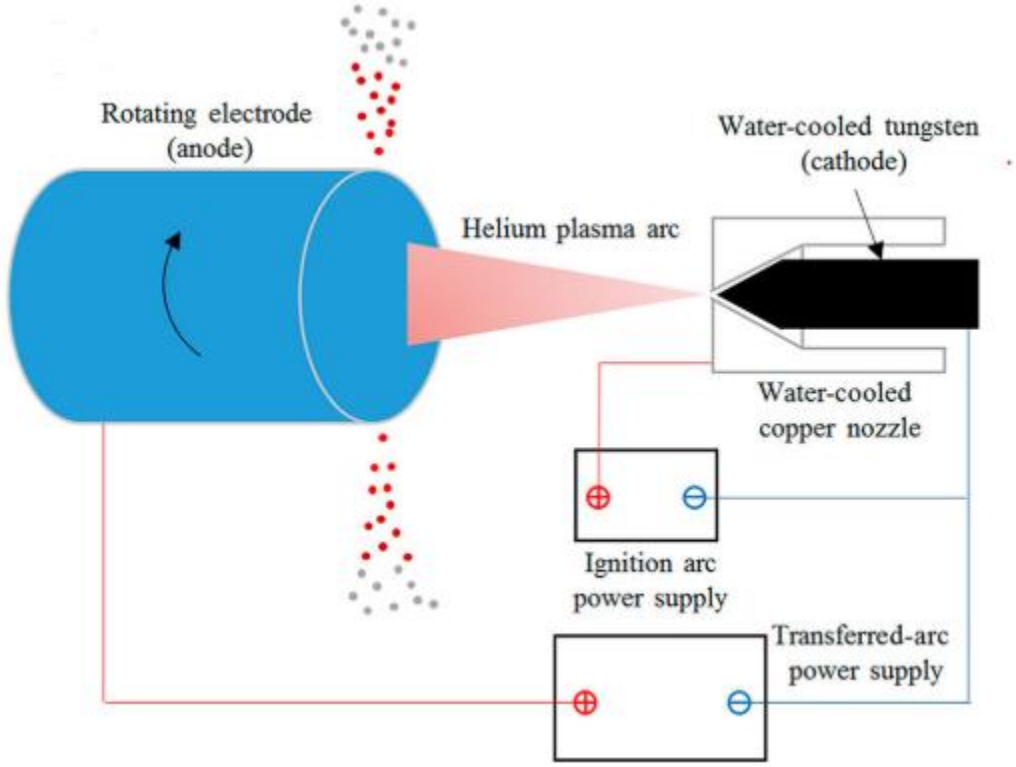

Figure 35. Schematic of the PREP system [11]

PREP-produced powders are highly spherical and coarse and can provide a good packing density. Factors such as the PA electrode diameter, rotational speed, and alloy chemistry influence the resultant powder particle size. For the Ti6Al4V alloy, the PREP process produces powders with a particle size distribution between 50 and 350 µm [11]. However, powders from both the REP and PREP cannot be used in some AM processes because of their high particle size distribution. The DMLS process and other LPBF processes use powders that have a particle size distribution between 20 and 50 µm for part production [13].

2.7.4 Comparison of the PA powder production processes

The above sections presented literature regarding the different PA powder production processes. Table 3 below is a summary of the characteristics of the different processes and the properties of the resultant powders.

Table 3. Comparison of the characteristics of the PA powder production processes used in AM

Feature	GA	PA	REP	PREP
Morphology	Spherical, may contain satellite particles [119]	Highly spherical, no satellites [119]	Highly spherical [89]	Highly spherical [11]
Flowability	Moderate to high [118]	High [13]	High [13]	High [13]
PSD (µm)	10–500 [11]	10–300 [11], [121]	50–300 [120]	50–350 [11]
Chemical purity	High purity if skull melting is used [122]	High purity [96]	May contain impurities from the electrode [96]	Very high [11]
Suitability for use in LPBF	Suitable [121]	Suitable [121]	Not suitable due to high PSD [121]	Not suitable due to high PSD [121]
Powder cost	Moderately priced	High-priced [121]	Moderately priced	High-priced

It can be deduced from Table 3 that the PA powder production processes can produce highly spherical PA powders with good flowability, except for the GA process. The powder produced from this process may exhibit satellite formation, negatively affecting its flowability [119]. The GA and PA processes produce powders with a PSD range required for the LPBF process. In contrast, the powders produced from the REP and PREP processes are more suitable for processes such as EBM and DED as they can process powders with a high PSD range [121]. In terms of chemical purity, the GA, PA and PREP-processed powders are chemically pure. In contrast, the powders produced from the REP process may contain impurities from the tungsten electrode used in this process [96]. The driving factor behind every manufacturing process is the cost associated with the starting material, as it will eventually affect the price of the final component [123]. The powder produced by the

PA process is generally more expensive than that produced through the GA process. This higher cost is due to the expense of the atomizing plasma and the wire feedstock used in the PA method, which negatively impacts the feasibility of using this powder for part production through LPBF.

Although GA powder is known to contain satellite powder particles, it is a more cost-effective alternative to the PA process [121]. Since the powder produced from the GA process meets most of the requirements for powders intended for use in LPBF, such as overall morphology, flowability and chemical purity, it can be used as feedstock in the LPBF process. The presence of satellites can be mitigated by sieving the powder using a sieve of the required powder particle size range [124]. Satellite particles are usually larger than completely spherical powder particles. Processing the powder through a sieve before use can effectively decrease the satellited powder content in the feedstock [124].

2.8 Powder-blending requirements for additive manufacturing

Powder blending is a process in which two or more powders of different properties are deposited into a mixer at certain weight percentages to obtain the most uniform particle distribution possible [125], [126]. The powder blending technique has been widely used in powder metallurgy (PM) technology to impart specific properties to the PM-produced parts due to the compositional flexibility provided by the addition of alloying elements [6]. Through powder blending and PM, parts can be produced from a blend of pure elemental powders or a mixture of elemental and master alloy powders. Besides the compositional flexibility offered by powder blending, this technique has also been used to improve the particle size distribution of the powder by blending powders of different sizes and shapes and then using the powder blend for PM part production. The powder blending technique has proved to be effective in improving the quality while lowering the production cost of the PM-produced parts [6], [9].

The powder feedstock conventionally used in MAM processes consists of pre-alloyed powders that are within a specified particle size range [13], [127]. To improve or impart certain properties to AM parts, powder mixtures consisting of PA and

elemental powders have been used in the LPBF process [100], [128]. Vrancken et al. [100] used a powder mixture consisting of PA Ti6Al4V and 10% Mo powders and in-situ alloyed it in the LPBF process in an attempt to modify the resulting microstructure and to improve the mechanical properties of the alloy. To determine the effect of Fe content on the Ti6Al4V microstructure, Simonelli et al. [128] used a powder blend consisting of PA Ti6Al4V and elemental Fe powders. These studies have provided evidence that the powder blending technique can be used in LPBF processes to prepare tailored powder blends that can impart certain properties to the final part. However, the studies described thus far used a powder blend consisting of PA Ti6Al4V powders whose composition was fixed, and elemental powders of a specific element. This kind of feedstock offers less room for compositional variance compared to a powder blend that consists of purely elemental powders [129]. A purely elemental powder blend would require thorough mixing to produce an alloy with a homogenous microstructure [8].

2.8.1 Powder-blending considerations

The metal powders that are normally used in AM machines have a high surface area-to-volume ratio and can be explosive [126], [130], [131]. For this reason, care must be taken during the storage and processing of these powders. Kalpakjian et al. [131] recommended some precautions that should be taken during powder blending, such as grounding the blending equipment, using anti-sparking tools, eliminating heat-producing friction, reducing the metallic dust cloud arising from the blending and preventing any open flames in the vicinity of the powder blending equipment. The humidity of the powder storage facility should also be taken into consideration, as the moisture content in the powders may result in particle agglomeration and disrupt the blending process. Due to the nature of these powders, the blending equipment should utilise a steady rotation or tumbling technique instead of a violently agitated technique to minimise the effects of friction on the interacting, abrasive powders [131].

The quality of a powder blend is dependent on several factors: the blending conditions, the blending time, the properties of the powders being blended and the blending equipment [8], [126]. For a powder blend intended to produce a high-quality alloy with a controlled composition, the powder blending should be performed under highly controlled conditions, such as in an inert gas atmosphere. This is to avoid

contamination and oxidation of the powders while blending [131]. There is no explicit rule for appropriate blending times in dry solid blending operations. This is because the starting powder for a particular blend has properties, such as particle size and morphology, that may vary from batch to batch and per manufacturer [126]. This, together with the variation in the blending equipment, indicates that the powder blending of dry solids can prove to be somewhat unpredictable. In a study by Simonelli et al. [8], the elemental powders were blended until the powder blend appeared to have a homogenous tone after a total blending time of 20 minutes. Short blending times should be avoided as they may result in the blended powder not being well-mixed and homogenous. Likewise, long blending times should also be avoided as they may promote de-mixing or segregation of the powder blend. The basic aim of powder blending is to create a homogenous powder blend. Therefore, the applied blending time should meet the main goal for the powder and blending equipment [8], [126], [129].

Physical properties of the powders, such as the particle size distribution, particle shape and true density, affect the powder blending process [8], [125], [131]. For a homogenous powder blend intended for use in AM processes, it is recommended that fine powder particles should be used as there is an increased probability of an even distribution of the alloying elements at a given time with reference to the laser-spot size as there would be if coarser powders were used [8]. However, a decrease in particle size could result in an increase in the inter-particle cohesive forces that may cause the particles to agglomerate, therefore forming an inhomogeneous powder blend [126], [129]. To overcome these inter-particle forces, the powder blend should be made up of powder particles with a balanced PSD (Gaussian distribution) that are within the size range of 20–45 µm to allow free movement between neighbouring particles [132].

Besides being a requirement for AM, it is generally much easier to blend spherical powders than it is to blend irregularly shaped powders if powders with a Gaussian PSD are used. Spherical powders with the required PSD range have the added advantage of increasing the packing density of the powder bed since there are fewer voids in the powder bed compared to the voids that would result from a powder blend consisting of irregularly shaped or coarse spherical powders [126]. Ideally, the

particles used for powder blending should be equally dense (true density). However, this is impractical as some particles may be denser than others due to their different compositions. During blending or the storage of the powder blend, the denser powder particles may be constantly drawn towards the bottom by gravitational force, resulting in the segregation of the powder blend.

All of the physical properties that have been discussed in this section ultimately affect the flowability of the powder blend [126], [127]. The flow of the powder blend can be classified as either mass or core flow using the Hall flow meter. In mass flow, the powder particles near the surface of the Hall flow meter and at the centre of the funnel will flow as a unit in the order in which they were poured into the funnel. Core flow refers to a type of flow wherein there is more particle movement at the centre of the funnel relative to the movement of the powder closer to the surface of the funnel, meaning that the central region of the funnel will discharge first, followed by the region closer to the funnel surface. The preferred flow in AM systems is the mass flow, which can be described as a non-interactive “first-in-first-out” [126] flow type. It is important that the powders within the AM powder blend are non-interactive and offer no hindrance to flow and spreading while maintaining a homogenous composition [126].

2.8.2 Blending methods

There are two main techniques used to blend powders, namely the simple mixing and satelliting techniques [8], [125]. The main difference is the use of a binding agent in the satelliting technique, which is meant to encourage cohesion between the powders being blended. The simple mixing technique, also known as the mechanical mixing [8] technique, involves the weighing of powders to a particular ratio and then depositing the powders into a steady rotating mixer. A typical result of such mixing is shown in Figure 36(a). Although uncomplicated, this blending technique may yield an inhomogeneous powder blend due to the absence of a binding agent during mixing. This inhomogeneity of the starting feedstock, if used in AM, will manifest in the final alloy as microstructural inhomogeneity, thereby affecting the mechanical properties of the alloy. Besides the inhomogeneity, this mixing technique results in powder mixtures that have poor repeatability because it is based on the principle of randomisation; no two powder blends can be the same [8].

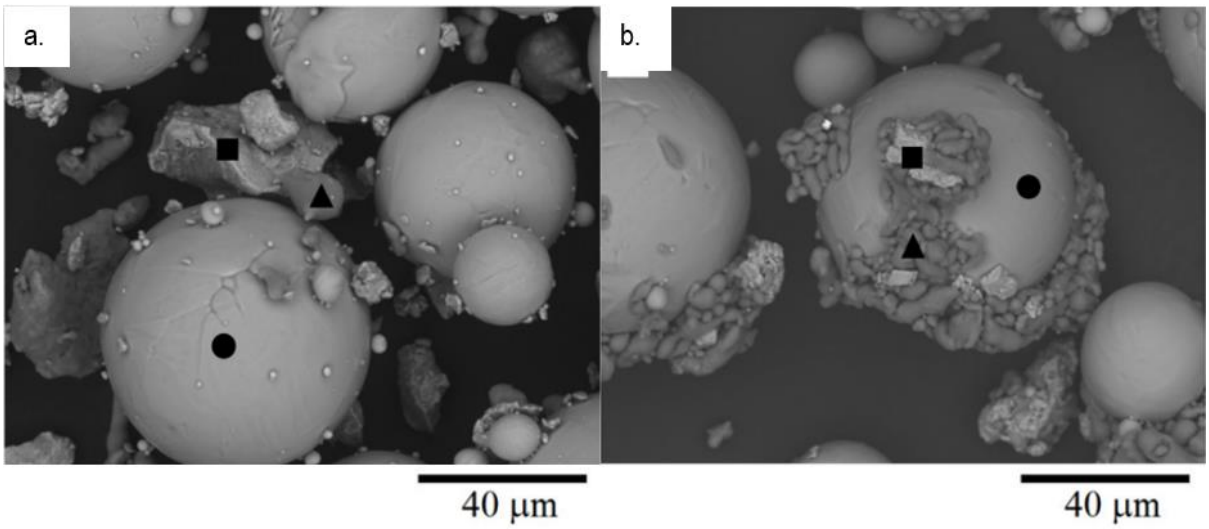

Figure 36. Powder blends produced by (a) simple mixing and (b) satelliting techniques. The circle, triangle and square represent the Ti, Al and V respectively. Edited with permission from the author [8]

The satelliting technique (result shown in Figure 36(b)), also known as “ordered mixing” [125], uses a similar approach to simple mixing with the only difference being the use of a binding agent. In this technique, the smaller alloying elemental powders are attached to the base elemental powder, which has a greater average PSD, using a binding agent such as polyvinyl alcohol (PVA). The resulting agglomerates are referred to as “ordered units” as each base powder particle has the alloying elemental powders attached to it, thereby improving the homogeneity of the powder blend and the overall homogeneity of the produced alloy. However, this technique results in a powder blend that has a decreased flowability compared to a simple mixed powder blend due to the new irregular shape of the agglomerates [8], [125].

2.8.3 Blending limitations

The dominating limiting phenomenon in powder blending is the segregation of the powder blend. Segregation in powder blending is the tendency of the powder blend to separate within the container when stored, handled, poured, or processed. This phenomenon occurs due to the different physical properties of the constituent powders with density, particle size and shape being the strongest contributing factors [8], [126], [129].

In an elemental powder blend intended for AM, it is certain that the powder particles used will not be equally dense. This difference in density results in powders with a greater density experiencing a greater gravitational force acting on them, which constantly draws these powders towards the bottom of the powder blend during storage and handling. The powder particles segregate based on their density, with the less-dense powder particles being on top, while the denser particles collect at the bottom of the powder blend [126], [129].

As with density, the powders used in the blend may have different powder particle sizes leading to a difference in the PSD of the powder blend. The finer particles will make their way to the bottom of the powder blend, leaving the larger powder particles at the top. [126]. The effect of the powder particle size is limited to a powder blend with a PSD greater than 30 µm. For a powder blend with a PSD of less than 30 µm, the interparticle cohesive forces between the particles act to keep the powder blend together thereby preventing segregation, at the expense of the flowability of the powder blend [126]. The effect of the powder particle shape, although not prominent, may also lead to segregation. If an interparticle void between a spherical and an irregular shape exists, finer powder particles may occupy the resulting void left by the misfit thereby affecting the homogeneity of the powder blend. Apart from the misfit, the difference in particle shape may lead to segregation during the spreading of the powder blend onto the build platform due to the poor flowability of irregularly shaped powders [8], [126], [129].

2.9 Comparison between BE and PA powders

It is widely known and accepted that using PA powders in AM processes enhances the likelihood of producing a part with a homogenous and superior microstructure [129]. However, the high cost of these powders renders them unjustifiable for application in less critical applications such as in the production of sporting equipment [9], [133]. In Table 4, the benefits and shortcomings of using PA and BE powders in AM systems are summarised.

Table 4. Comparison of the benefits and shortcomings of using blended elemental powders vs. pre-alloyed powders in additive manufacturing

Feature	Blended elemental powders	Pre-alloyed powders
Alloy compositional flexibility	Offer greater compositional flexibility. Any alloy composition can be readily blended from the available elemental powders. [8]	Do not provide any compositional flexibility. A new batch of powder will have to be bought for any new alloy production. [8]
Cost-Efficiency	Cost-effective for custom alloys and small production batches. [9], [129]	May be cost-intensive for some applications. [9], [129], [133]
Processing	Complex processing. The blending process can be complicated and unpredictable. No two powder blends can ever be 100% similar. [8], [9]	Simplified processing due to a constant composition in the powder bed. [8], [9]
Microstructural variations	Microstructure may be inconsistent if the starting feedstock composition is not homogenous. The outcome of the powder blending process affects the microstructure. [9], [129]	Consistent microstructure due to the controlled composition at the feedstock level. [8], [129]
Material handling and safety	Risk of unhealthy exposure to the different elemental powders during blending and processing. [134], [135]	Equal risk of toxic exposure to elements although already alloyed. [134], [135]

Risk of contamination	High risk of contamination if blending and processing conditions are not controlled. [8], [9]	Low risk of contamination that may only arise during processing. [8], [9]

It is evident from Table 4 that the PA and BE powders have their advantages and disadvantages when used as feedstock in AM processes. Although capable of producing parts with superior mechanical properties, PA powders are costly and offer less compositional variation [9], [129]. The BE route, on the other hand, offers compositional variance; however, the produced microstructure can be inhomogeneous due to the inhomogeneity of the powder blend. This inhomogeneity of the powder blend is the major factor prohibiting the widespread use of BE powders in AM systems [8].

2.10 Summary

In this chapter, an extensive review of the core topics relevant to the MAM of the Ti6Al4V alloy was presented. The review began with an overview of the different AM processes followed by an in-depth review of the DMLS process with a specific focus on process parameter optimisation.

The distinct properties of the Ti metal were discussed, and the effects of different alloying elements, such as Al and V, on the Ti phase diagram were analysed. This was followed by a detailed review of the Ti6Al4V alloy wherein the unique properties of this alloy were discussed. The Ti6Al4V alloy produced from wrought processes such as metal forging is known to be the best version of this alloy in terms of its mechanical properties. For this reason, the Ti6Al4V alloy produced through LPBF was compared with the wrought Ti6Al4V alloy on a microstructural level. The efficacy of techniques such as heat treatment in improving the mechanical properties of the LPBF Ti6Al4V alloy was analysed.

Lastly, the production of the PA powders which are commonly used as feedstock in the LPBF process, and the production of elemental powders as the proposed LPBF

feedstock was outlined. This led to a comparison of the limitations and advantages of using PA powder versus BE powder as feedstock in the LPBF process. The insight gained from this literature study served as the foundation to produce the Ti6Al4V alloy from BE powders.

Chapter 3 Materials and methods

3.1 Introduction and experimental procedure

The contribution to the greater body of the AM knowledge produced in this research should not only be openly available, but the results should also be reproducible. This chapter aims to provide a report on the different powder feedstock materials, the production machine, and the analytical equipment used to achieve the aims and objectives specified in Chapter 1. The flowchart shown in Figure 37 provides a visual representation of the process followed to produce and analyse the experimental specimens used in this study.

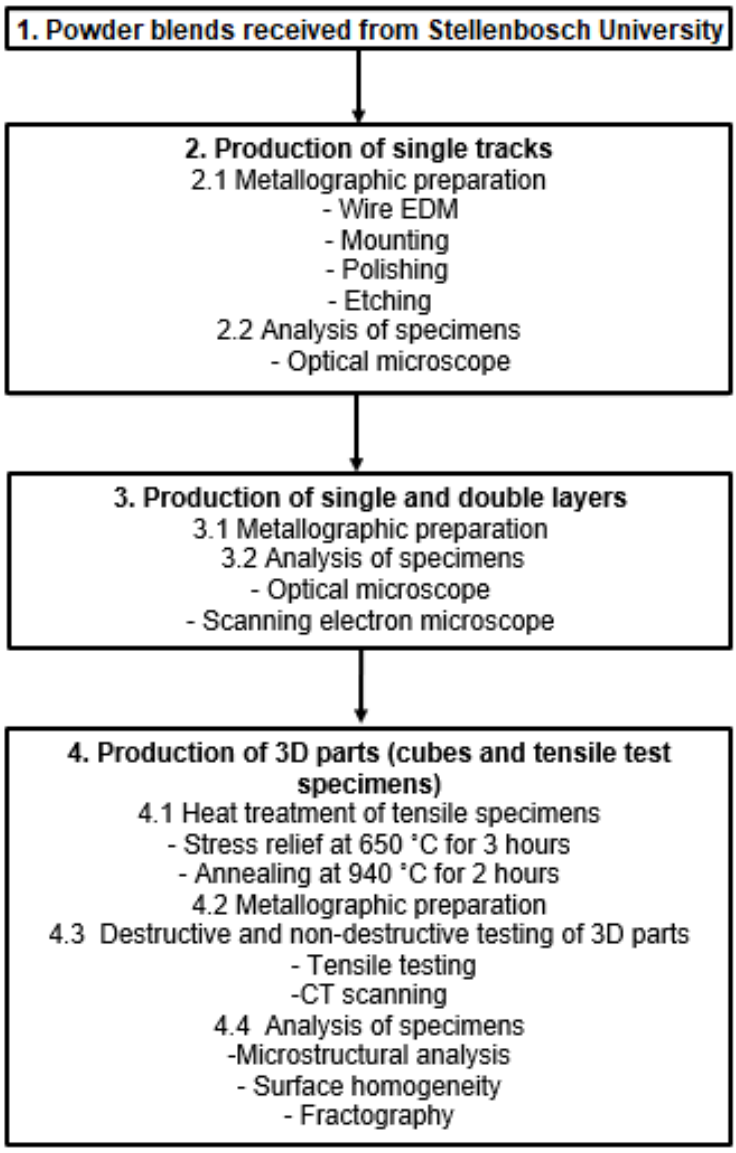

Figure 37. Schematic overview of the methodology followed in this study

3.2 Powder materials

The experimental component of this study is focused on the DMLS process parameter development and optimisation for two different powder materials. The first powder material is “powder blend 1” (PB 1) which consists of an elemental Ti and an Al-V MA which have been blended in the ratio of 90% Ti and 10% Al-V MA. The second powder blend, “powder blend 2” (PB 2) is a purely elemental powder blend consisting of elemental Ti, Al and V blended in the ratio of 90, 6, and 4 (wt.%), respectively. The powder blending and characterising was done at SU. The blended and characterised powders were delivered to CUT at proportions of 1215 and 1525 g for blend 1 and 2, respectively. The chemical composition analysis of the powder constituents of each blend was conducted using an Inductively Coupled Plasma Optical Emission Spectroscopy (ICP-OES) analyses by the South African Nuclear Energy Corporation Soc Limited (NECSA). The full report from the analysis, including the concentration of the interstitial elements, is provided in Appendix 1.

3.2.1 Powder blend 1 – CP Ti -10 MA

This powder blend was used in this study as a preliminary investigation into understanding the behaviour of elemental CP Ti powder in the DMLS process during in-situ alloying. Additionally, a MA of Al and V was used to obtain an indication of the amount of Al evaporation from the MA that might occur during in-situ alloying and to assess the feasibility of using a combination of elemental and PA powders in the DMLS process. The CP Ti powder was argon gas-atomised, while the MA powder was produced by an aluminothermic smelting process followed by ball milling. The particle size for the Ti powder was in the range of 20–45 µm, and the MA had a particle size ranging from 20–80 µm. A SEM micrograph of the powder blend is provided in Figure 38. The gas-atomised Ti powder was completely spherical, while the ball-milled MA powder had an irregular angular shape.

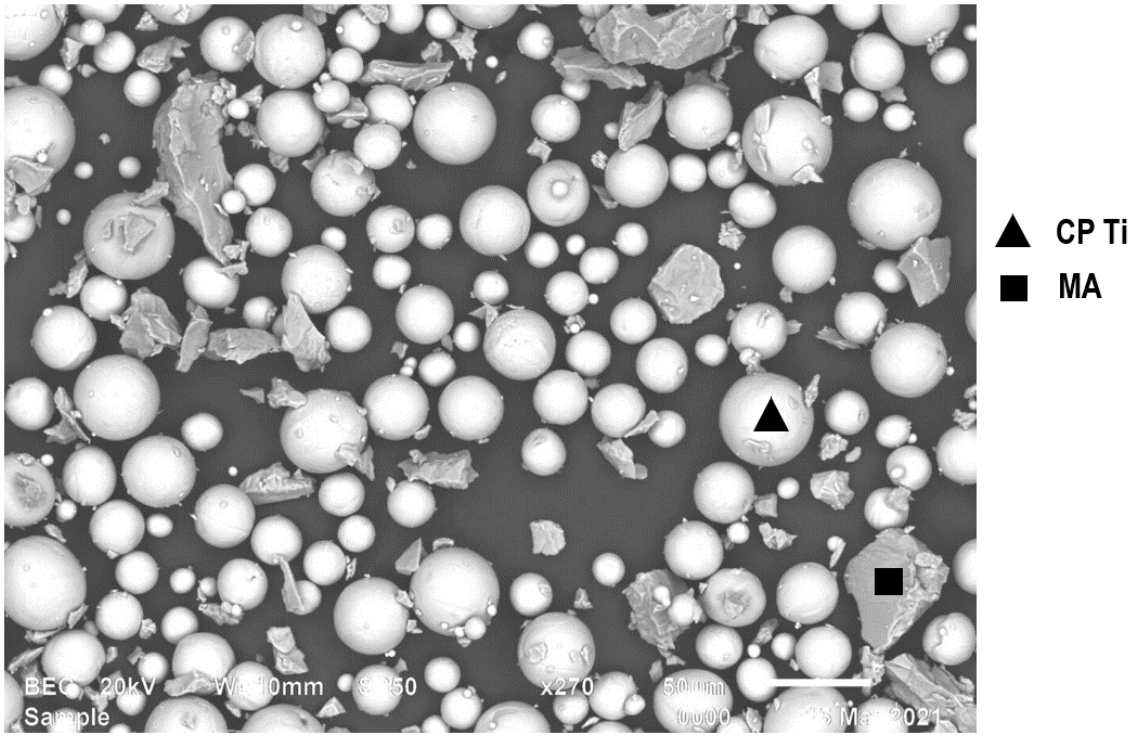

Figure 38. SEM micrograph of powder blend 1

The ICP-OES chemical composition analysis of the constituents of PB 1 is shown in Table 5. From this table, the compositional purity of the alloying elements is less than the expected composition due to the inevitable presence of interstitial elements. However, the composition of these metal powders is in accordance with the ASTM F2924-14 standard, as shown in Table 5.

Table 5. Chemical composition of the powders used in powder blend 1

Blend 1		
Constituent	**Chemical composition (wt.%)**	**ASTM F2924-14**
Elemental Ti	99.3	Remainder
Al (MA)	54.8	5.5–6.75
V (MA)	43.4	3.5–4.5

3.2.2 Blend 2 - Ti-Al-V

This purely elemental powder blend was the focus of the study. An indication of the feasibility of using elemental powder blends in the DMLS process was obtained using this powder blend. This powder blend consisted of CP Ti, Al and V powders that were blended to the ratio of 90, 6 and 4 wt.%, respectively. The CP Ti and Al powders were argon gas-atomised, while the V powder was produced by an aluminothermic smelting process followed by ball milling. The Al powder does not appear to be 100% spherical due to the low molten-state surface tension of the molten Al metal. Due to the low surface tension, the morphology of the molten spherical Al droplet is affected by the turbulent, pressurised gas, resulting in the formation of irregular spherical powders upon solidification [136]. A SEM micrograph of this powder blend is shown in Figure 39 below. The CP Ti powders can be identified by a highly spherical morphology, while the Al and V powders have an irregular spherical and round irregular morphology, respectively.

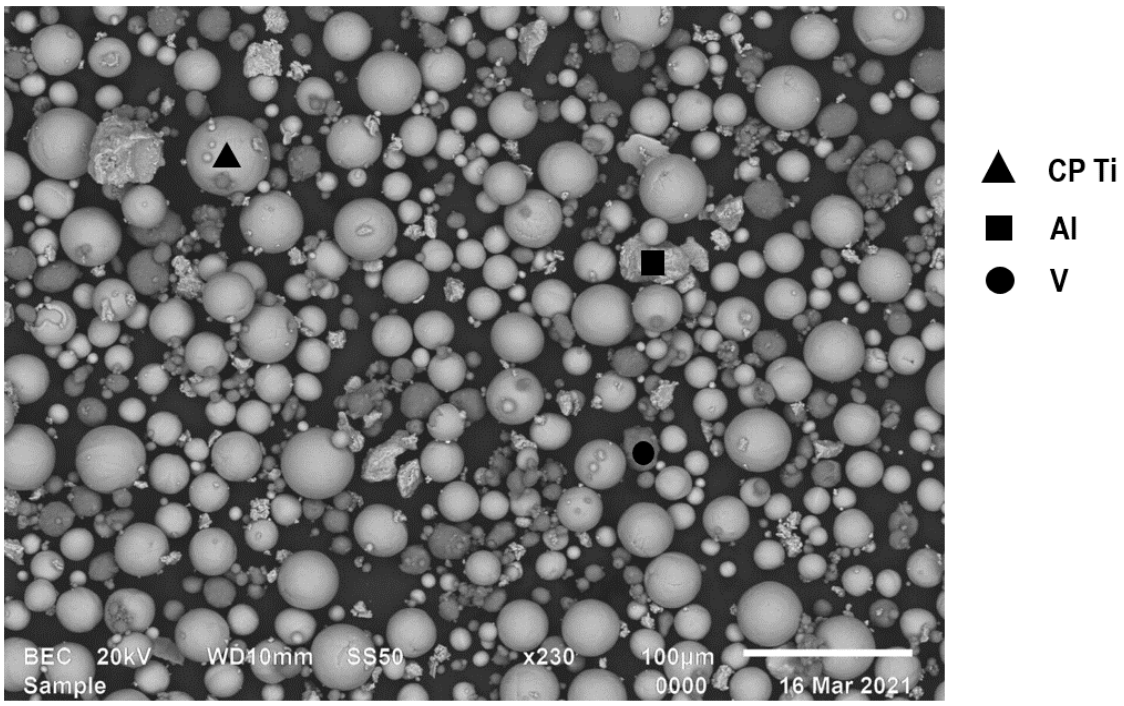

Figure 39. SEM micrograph of powder blend 2

The ICP-OES chemical composition analysis of the constituents of PB 2 is shown in Table 6. Contrary to PB 1, the powders used in PB 2 were much purer, with the alloying elements' compositional purity being only slightly less than their expected composition. The interstitial elements present in the powders were 0.1%, 0.8% and 1% of the total compositions of the CP Ti, Al and V powders, respectively. This shortfall in the alloying elements will be considered in the compositional analysis of the final parts. A detailed report of the ICP-OES analyses for PB 1 and PB 2 is provided in Appendix 1.

Table 6. Chemical composition of the powders used in powder blend 2

Blend 2		
Constituent	**Chemical composition (wt.%)**	**Deviation (wt.%)**
Elemental Ti	99.9	0.1
Elemental Al	99.2	0.8
Elemental V	99.0	1

3.3 Experimental design

The same experimental and analytical procedures were followed for the production and analysis of samples from both PB 1 and 2. A hierarchal experimental approach was followed to develop a full set of process parameters suitable for the production of the Ti6Al4V alloy from the powder blends [2]. Firstly, single tracks were produced from a range of primary process parameters (laser powers and scanning speeds) and analysed to identify a set of process parameters that produced optimum single tracks. The single-track analysis was conducted in two phases. In the first phase, optical microscopy was used to observe the top views of the single tracks and identify continuous and non-continuous single tracks. In the second phase, the continuous single tracks were analysed on the cross-sectioned substrate to observe their substrate penetration shape and depth together with the track height, width and angle of contact between the single track and the substrate surface. Secondly, using the identified process parameters from the single-track analysis, single and double layers were produced to identify an optimum hatch distance suitable to produce defect-free layers. The morphology and homogeneity of the layers were assessed before and

after the rescanning strategy was applied. The bonding relationship between the super-positioned tracks, together with the intra-layer bonding relationship between two layers, were determined from the cross-sectioned specimens. Lastly, the set of process parameters that were identified from preceding analyses were used to produce 3D specimens. All experiments were carried out using a powder layer thickness of 60 µm. An overview of the experimental design approach is shown in Figure 40 below.

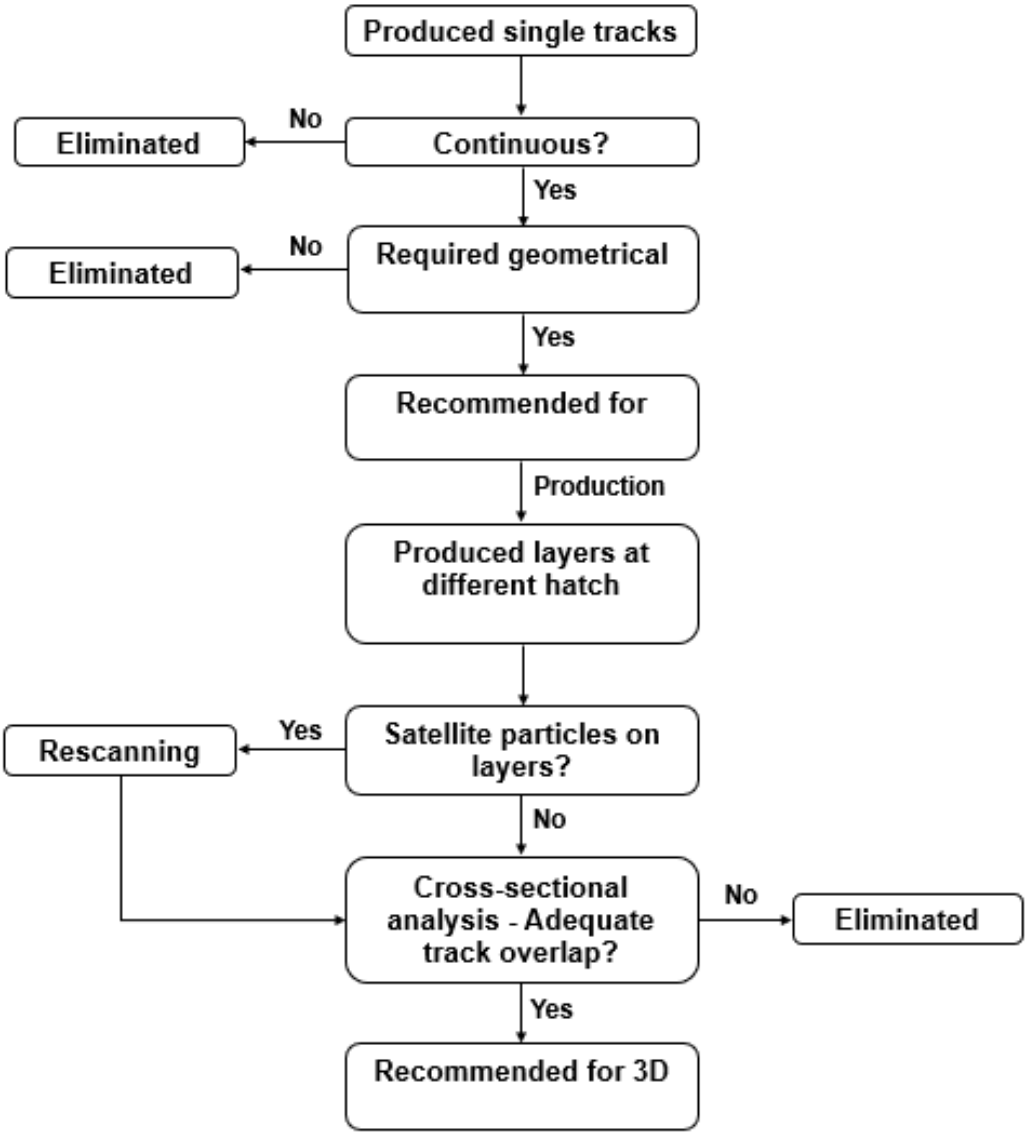

Figure 40. Flow chart overview of the experimental procedure followed to identify process parameters for 3D part production

3.3.1 Production of single tracks

Essentially, DMLS-produced parts consist of a horizontal and vertical array of single tracks that are placed according to the part geometry, as illustrated in Figure 5. Single tracks can be considered as the building blocks of DMLS-produced parts. Therefore, it is imperative that the process parameters that govern the production of optimum single tracks be investigated for each powder material. For this reason, a wide range of primary process parameters (laser power and scanning speed) were used to produce single tracks using the powder blends. Each powder blend is a different material with its specific properties. An experimental design was developed for each blend to ensure the optimisation of the process parameters that are tailored for each blend. Since this study is focused on the production of the Ti6Al4V alloy through the DMLS process, the experimental design was developed based on the process parameters that were found to produce optimum single tracks in studies using PA Ti6Al4V powders [24], [137]. The equation [138]:

$$E = \frac{P}{V} \tag{1}$$

where E is the energy density (J/m), P is the laser power (W), and V is the scanning speed (m/s), was used to determine the energy density to produce optimum single tracks from PA powders successfully. Once determined, different combinations of laser power and scanning speeds that radiated a similar energy density were formulated and used to produce single tracks from PB 1 and 2.

3.3.1.1 Single tracks – Powder blend 1

Single tracks were deposited on a 3 mm thick Ti6Al4V substrate from a CP Ti-10 MA powder blend using laser powers of 100, 150, 170 and 200 W and scanning speeds ranging from 0.4 to 1.8 m/s. For each laser power and the corresponding scanning speeds, three single tracks, 20 mm in length, were produced. A total of 28 combinations of laser powers and scanning speeds were investigated for this powder blend. Figure 41 below displays the layout of the single tracks on the substrate.

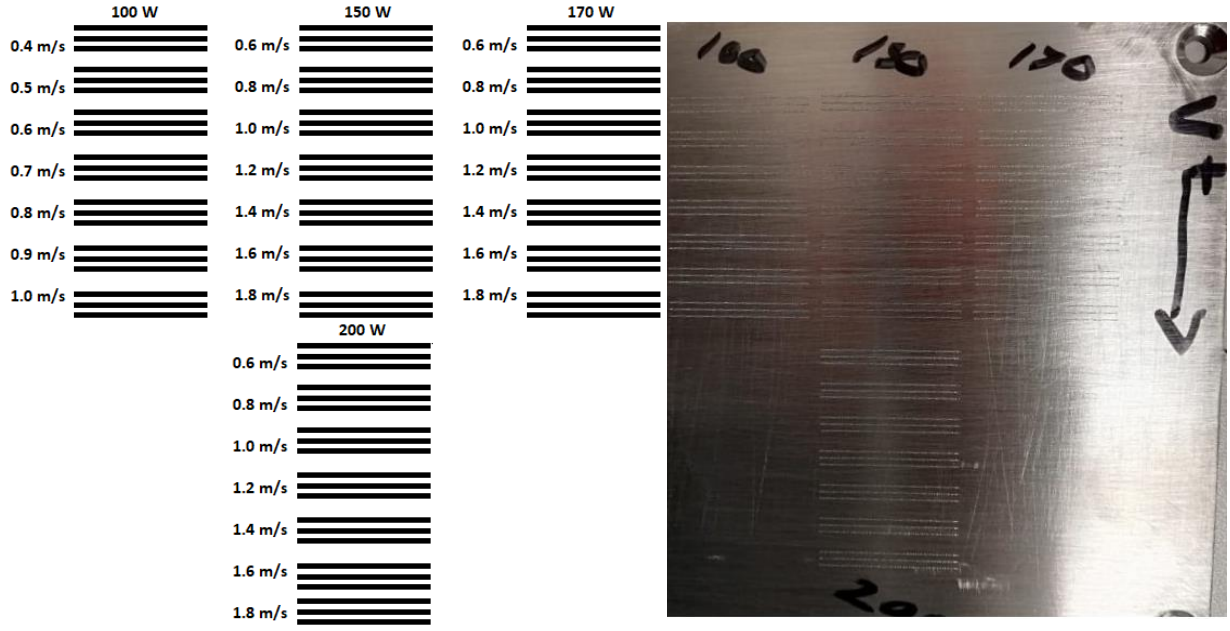

Figure 41. The layout of the single tracks produced from powder blend 1

3.3.1.2 Single tracks – Powder blend 2

The experimental design for the deposition of single tracks from the purely elemental powder blend (Figure 42) was broader than the experimental design used for PB 1.

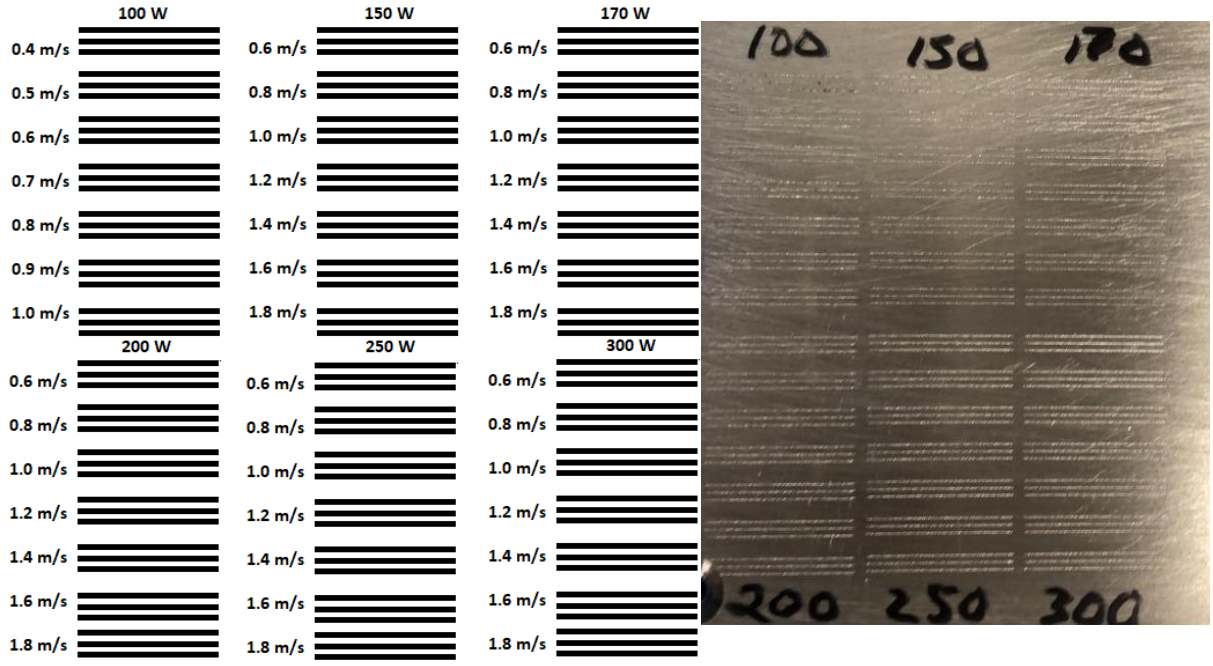

Figure 42. The layout of the single tracks produced from powder blend 2

A broader experimental design was required to try to obtain an experimental design as wide as possible as this powder blend consisted of elemental powders, which means that the laser-to-powder interaction may be more complicated than with PB 1. The single tracks were then deposited on a 3 mm thick Ti6Al4V substrate using laser powers ranging from 100 to 300 W and a scanning speed range of 0.4 to 1.8 m/s. Three single tracks were produced for each combination of laser power and scanning speed; a total of 42 process parameters were used to produce single tracks for analysis.

3.3.2 Production of single and double layers

Once the deposition of an optimum single track had been mastered, the next phase of process parameter development involved the production of a single layer using a variety of hatch distances to assess the intra-layer characteristics of the layer. A second layer is also crucial to obtaining an understanding of the inter-layer bonding between two layers at varied hatch distances [139]. A rescanning strategy was used to optimise the morphology of the layers by remelting the satellite particles that were formed on the surface of the layers.

3.3.2.1 Single and double layers – Powder blend 1

Two optimum process parameters were obtained from the single-track investigation. A total of six single layers and six double layers were produced for each process parameter. Each process parameter was paired with three hatch distances of 80, 90 and 100 µm, respectively. Therefore, four trial specimens were produced for each hatch distance. The average track width of the optimum single tracks that were produced from the preceding single tracks experiment was taken into consideration when selecting these hatch distances to ensure adequate track shifting and sufficient bonding between the super-positioned single tracks. The rescanning strategy (double scan) was applied to two of the four trial specimens for each hatch distance. The layout of this experiment is shown in Figure 43.

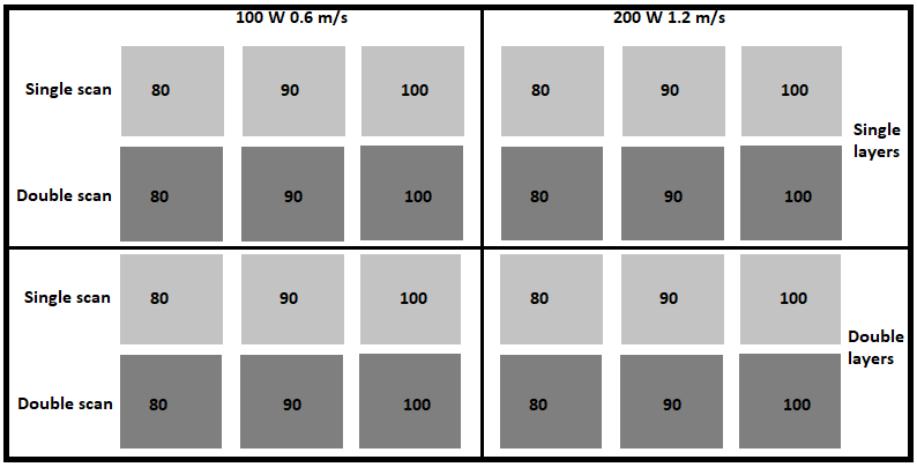

Figure 43. The experimental design to produce single and double layers from powder blend 1

3.3.2.2 Single and double layers – Powder blend 2

Single and double layers were produced on two 3 mm Ti6Al4V substrates using the two process parameters that were identified as optimum from the blend 2 single-track analysis as illustrated in Figure 44.

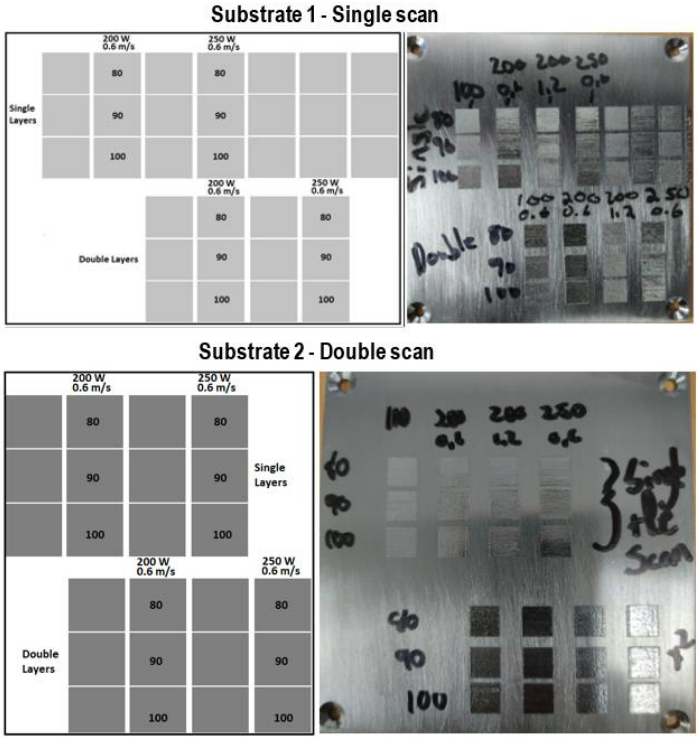

Figure 44. The experimental design to produce single and double layers from powder blend 2.

The first substrate consisted of a total of three single layers and three double layers that were produced at varied hatch distances of 80, 90 and 100 µm for each process parameter. The second substrate was used to produce three single layers and three double layers at hatch distances of 80, 90 and 100 µm using the rescanning strategy.

3.3.3 Production of 3D test specimens

For each powder blend, two sets of process parameters were developed from the preceding experiments and their respective analyses and used to produce 3D specimens. Starting with the deposition of single tracks and proceeding to single, double, and multiple layers, 3D-part production is essentially a repetition of the layer production process, with the only difference being the dimensions of each layer. The same experimental procedures and setups illustrated in section 3.3.3.1 were used to manufacture and prepare the 3D samples from PB 1 and PB 2 for analysis.

3.3.3.1 3D test specimens

The layout used to produce 3D specimens is shown in Figure 45 below. Three experimental cubes with dimensions of 8 x 7.5 x 7 mm (L x B x H) were produced on a 6 mm Ti6Al4V substrate for each process parameter, and the rescanning strategy was applied to the top layers of each cube. Two scaled-down tensile test specimens of respective diameters and lengths of 6 and 50 mm were produced for each process parameter set (PPS). These tensile test specimens were scaled down according to the ASTM E8M "*Standard Test Methods for Tension Testing of Metallic Materials*" standard to ensure that the production could occur inside the reduction chamber due to the limited amount of powder available.

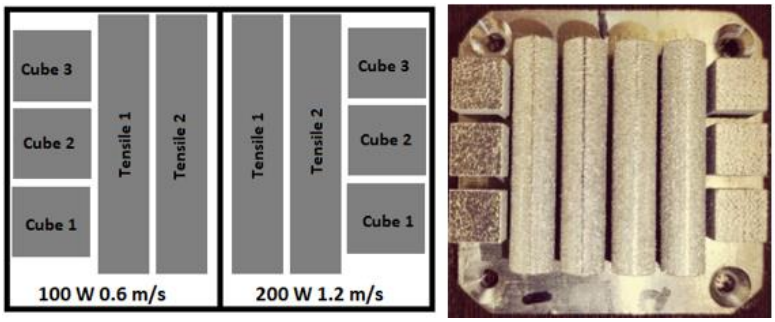

Figure 45. Experimental layout of the 3D specimens produced from the blends.

The production of the 3D cubes was successful; however, the production of the scaled-down tensile testing specimens was flawed as they had broken off from the substrate due to residual stresses in the build, refer to Figure 46. From this figure, it can clearly be seen (red arrows) that the front edges of the tensile test specimens had separated from the substrate, resulting in the tensile specimens being bent along their length. This failed attempt at producing the specimens necessitated the incorporation of stronger support structures into the build of the specimens.

Figure 46. 3D test cubes and the failed tensile test specimens

In the second attempt to produce the scaled-down tensile testing specimens, support structures were used to prevent the specimens and the substrates from separating. Four tensile test specimens of respective diameters and lengths of 6 mm and 50 mm were produced for each process parameter set on a 15 mm Ti6Al4V substrate. To relieve the residual stresses built up during the building process, the specimens were first stress-relieved at 650 °C for a soaking period of three hours and subsequently annealed at 940 °C for two hours before they were cut from the substrate**.** Figure 47 shows the layout used to produce the tensile test specimens and the support structures used in the build, which are illustrated by the red arrows. The support structures were designed to break off from the specimens easily while also being strong enough to withstand the residual stresses accumulated during the build.

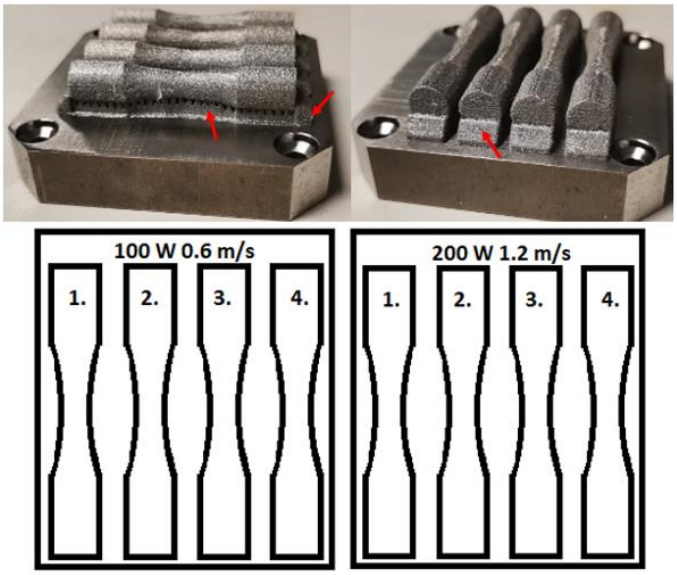

Figure 47. Second attempt at producing the scaled-down tensile test specimens

3.4 EOS M280

An EOSINT M280 (Electro Optical Systems GmbH, Krailling, Germany) machine (Figure 48) at the Centre for Rapid Prototyping and Manufacturing (CRPM) at CUT was used to produce single tracks, single and double layers, and 3D parts.

Figure 48. The EOSINT M280 machine

This EOSINT M280 DMLS machine consists of a production chamber that has a recoater arm assembly, a computer-controlled elevating and lowering system, a platform module, a laser optical system and a system that controls the shielding gas used in the process. These individual components work together to ensure the systematic production of quality parts. This machine uses a 400 W Yb-fibre laser beam with a spot size of 80 µm to fuse the metal powder during the part production process. The laser beam is controlled by a scanner with a maximum scanning speed of 7 m/s, which follows the directions provided by the layered STL blueprint for the part to be produced. During part production, the production chamber is filled with a shielding inert gas such as argon; therefore, highly reactive powder materials can easily be used as feedstock for part production.

The build volume of the EOSINT M280 machine is 250 x 250 x 325 mm. Since only a limited amount of powder for each powder blend (1215 g for blend 1 and 1525 g for blend 2) was received from SU, the build volume would be too large for the powder to form multiple layers and prohibit part production. For this reason, the EOSINT M280 machine was equipped with a reduction unit system (Figure 49), which allows the use of small amounts of powder to produce parts. All the experiments in this study were conducted within the reduction unit.

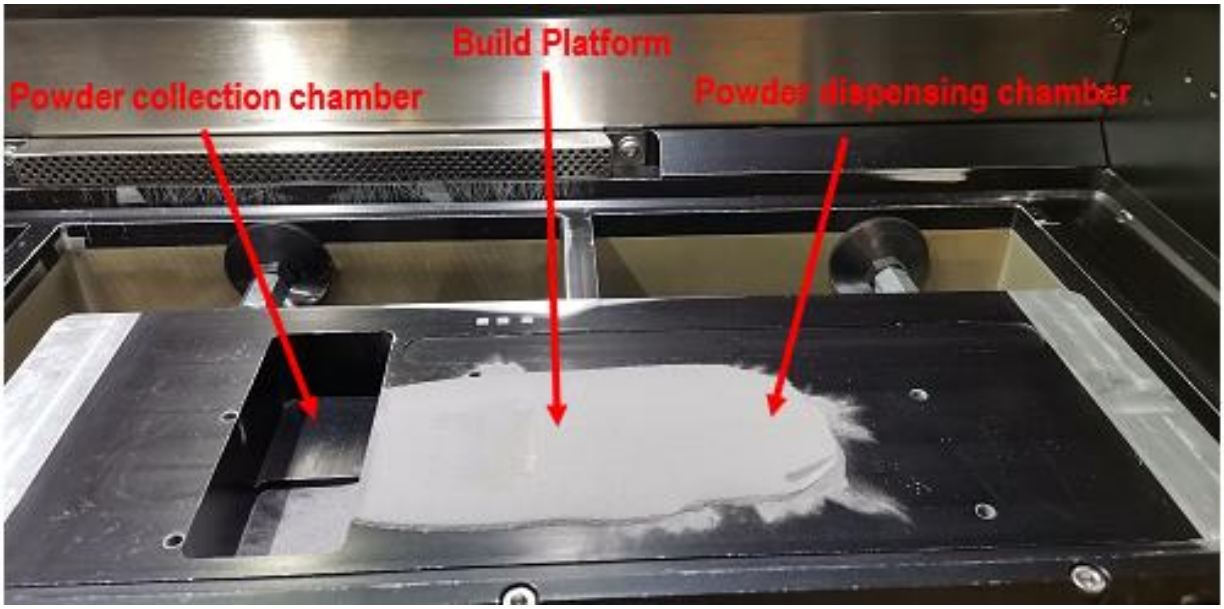

Figure 49. EOSINT M280 reduction unit.

3.5 Sample preparation: methods and equipment

3.5.1 Sample cutting

The single tracks, single and double layers, and 3D parts had to be cut to prepare them for their respective analyses. The single tracks and single and double layers had to be cross-sectioned across the lengths of the tracks while they were on the substrates to prepare them for their respective cross-sectional analyses. The 3D parts had to be removed from the substrates so that they could be machined and further analysed. To perform this cutting, a method that would not contaminate or radiate heat, thereby causing changes to the microstructural properties of the samples, had to be used to ensure that the samples remained in their “AB” condition.

The JiangSu Fangzheng electrical discharge machine (EDM) shown in Figure 50 was used to cut the samples. The computer numerical control (CNC) machine uses a 0.25 mm thick electrically charged wire to remove material from a workpiece. This process utilises deionized water in the cutting operation. While the workpiece is submerged in the water, the wire runs through the workpiece according to the specified cutting blueprint. The water controls the spark the wire makes when it meets the workpiece, while also cooling the cutting surface and flushing the material away from the workpiece.

Figure 50. JiangSu Fangzheng EDM.

3.5.2 Mounting

Once the samples had been wire-cut to their respective dimensions, they were mounted in resin. This was done to facilitate the easy handling of the samples during the analyses. It is important that the type of mounting process used does not deform or affect the properties of the samples.

The Struers CitoPress-15 electro-hydraulic hot mounting press machine (Figure 51) was used to mount the samples into resin. The CitoPress-15 has a mounting diameter of 30 mm and uses a combination of heat and pressure to consolidate the mounting resin powders. ClaroFast clear resin was used to mount the samples. The mounting parameters are shown in Table 7.

Figure 51. Struers CitoPress-15 hot mounting press machine

Table 7. Mounting process parameters for the ClaroFast clear resin

Quantity of resin powder	20 ml
Heating temperature	180 °C
Heating process time	4 minutes
Consolidation pressure	350 Bar
Cooling rate	Low
Cooling process time	6 minutes
Total process time	10.5 minutes

3.5.3 Polishing and etching

A Struers Tegramin-30 polishing and grinding machine (Figure 52) was used to remove the roughness and any impurities left on the surface of the samples. The Tegramin-30 is a microprocessor-controlled automatic machine that can grind and polish up to six samples at the same time. The grinding and mirror polishing is done using a series of grinding and polishing 300 mm MD-disk pads and different lubricating diamond solutions. The grinding and polishing disks are rotated at speeds up to 600 rpm. At the same time, the specimens are held in place by the specimen holder and pressed against the rotating surface of the MD-disc by pneumatically controlled actuators.

Figure 52. Struers Tegramin-30 grinding and polishing machine

The mirror-polished samples were etched using Kroll's Reagent in a ductless fume cabinet to reveal their surface structure. Kroll's reactant is a metallographic etchant used primarily for Ti and Ti alloys. The etchant was applied to the samples for an exposure period of 5 to 10 seconds until small bubbles started to nucleate on the surface of the samples. The samples were then immediately cleaned with ethanol to stop the etching process and dried.

3.5.4 Computer numerical controlled (CNC) machining

To obtain an accurate indication of the mechanical properties of a material, it is required that the specimens used for tensile testing should have a high surface finish (low surface roughness) to eliminate premature fracture due to stress concentrations associated with a high surface roughness [140]. The Ra (Arithmetic Mean Roughness) value, which is the arithmetic average of the change in the surface profile over a given length, measured from a central line [141], ranges from 10–25 µm [142] for LPBF-produced parts and 0.8–1.6 µm [143] for CNC-machined components. The high surface roughness in LPBF parts warrants the need for post-processing through CNC machining to reduce the surface roughness of the tensile test specimens.

In this study, the tensile test specimens were produced to a near-net-shape in the EOSINT M280 machine, as demonstrated in Figure 47. A Leadwell T/7AM CNC Turn-mill machine was used to machine the specimens to their final dimensions in accordance with the ASTM E8/E8M standard [140]. The ability of the CNC machine system to machine parts to a high tolerance while providing a high surface finish greatly influenced the decision to use this machine to prepare the specimens for tensile testing. Figure 53 shows the tensile specimens before and after they were machined. Through visual inspection, it can be seen that the AB tensile specimens had a higher surface roughness than the machined specimens.

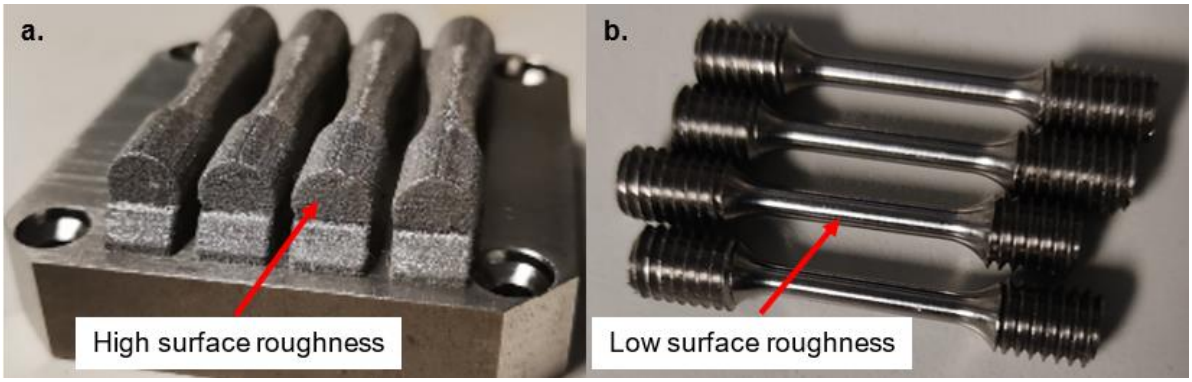

Figure 53. Tensile test specimens in their AB (a) and CNC-milled (b) conditions

3.5.5 Heat treatment

To relieve residual stress and improve the mechanical properties of the produced 3D parts, stress relieving and annealing heat treatments were performed using a T-M Vacuum Products Inc Super Series X furnace shown in Figure 54.

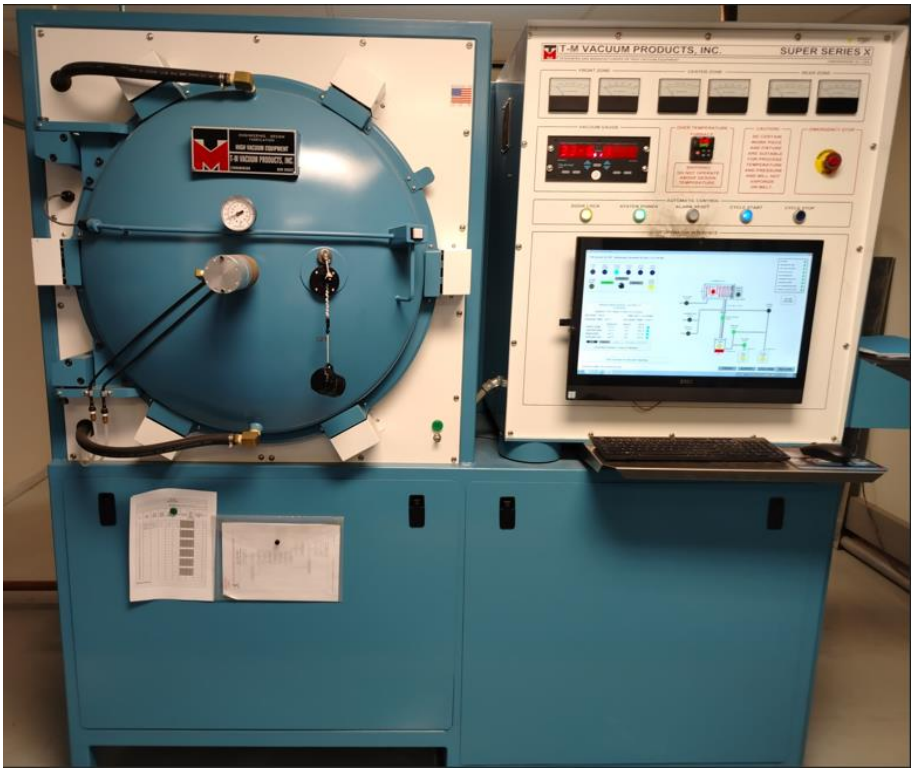

Figure 54. The T-M Vacuum Products Series X furnace.

The specifications of the stress relieving and annealing heat treatments are shown in Table 8.

Table 8. Heat treatment parameters.

Process	Temperature (˚C)	Duration (hours)	Cooling method
Stress relief	650	3	Furnace
Annealing	940	2	Furnace

3.6 Sample analysis and testing: methods and equipment

3.6.1 Optical analysis

A Zeiss-Axio Scope.A1 optical microscope (ZEISS, Oberkochen, Germany) shown in Figure 55(a) was used to analyse the surface morphology and the microstructure of the samples during their respective analyses. The Zeiss-Axio Scope.A1 can provide optical imaging of metallic materials for metallurgical analysis. Through the incorporation of the Zeiss-Axiocam camera portfolio and the Zeiss Zen 2 core imaging software, the user can have a real-time view on the desktop during analysis.

Figure 55. Analytical equipment used for optical analysis (a) Zeiss-Axio Scope.A1 optical microscope (b) and JEOL JSM-7800F scanning electron microscope (SEM) [144]

Secondary electron imaging (SEI) on the JEOL (Tokyo, Japan) JSM-7800F scanning electron microscope (SEM) shown in Figure 55(b) [144] was used to perform a more intense analysis of the surface morphology and microstructure of the samples. Additionally, the SEM was used to analyse the fracture surfaces of the tensile specimens. Contrary to the optical microscope that focuses a light source onto the sample, the SEM uses an electron gun to produce electrons which interact with the surface of the sample [145]. The SEM detects the features of the sample's surface, resulting in an image that displays the morphology of the sample in a 3D manner. The SEM can take images of particles as small as 2 ŋm up to 2 mm; hence, it can be used to provide more detailed images [145].

3.6.2 X-ray computed tomography

LPBF-produced parts are known to contain defects such as voids and porosity due to different process-induced phenomena, such as lack of fusion and keyhole mode instability [74], [146]. The production of parts that are 100% pore-free can be very challenging due to the inherent nature of this manufacturing technique. X-ray computed tomography was used to analyse the samples to provide a detailed assessment of the internal defects that may be present in the specimen without damaging the structure of the specimen (non-destructive analysis) [41].

For each PPS used to produce 3D specimens from the two powder blends, one cube was analysed for porosity, void formation and possible defects using X-ray computed tomography. A Phoenix Nanotom S [147] system, (see Figure 56) installed at SU was used to perform this non-destructive, quantitative analysis. This system uses X-ray computed tomography to provide a detailed analysis of the internal structure of metallic and non-metallic samples. The X-rays of the samples were generated using a voltage of 150 kV and a current of 100 µA at a voxel size of 7 µm. Using Datos reconstruction software, a volumetric dataset was reconstructed from 3200 images as the sample was rotated 360°. The reconstructed dataset can be visualised and analysed using the Volume Graphics VGSTUDIO MAX 3.5 software, in which information on pores and voids greater than eight voxels can be obtained. Appendix 2 provides the technical sheet of the analysis conducted on the experimental samples.

Figure 56. Phoenix Nanotom S X-Ray Tomography system installed at SU [147].

3.6.3 Tensile testing

To obtain an indication of the mechanical properties of the produced alloy, the machined and threaded tensile test specimens were strained using the MTS Criterion Model 43 tensile testing machine shown in Figure 57. To allow for proper alignment and to eliminate slack in the clamps, the tensile testing machine was pre-loaded at 0.06 kN before the actual tensile test started. The tensile tests were carried out at a strain rate of 0.4 mm/min until fracture occurred. Values of the mechanical properties such as the UTS, YS and ε were recorded. A comprehensive technical report of the mechanical testing is provided in Appendix 3.

Figure 57. The MTS Criterion Model 43 tensile testing machine.

3.7 Summary

This chapter described the materials and methods used to achieve the aims and objectives of the study stated in sections 1.3 and 1.4. The morphology, particle size and composition of the powder materials used were described. The details of the EOSINT M280 machine used to manufacture the samples, as well as the experimental parameters used to produce the samples, were provided. The manufactured samples, together with their respective production layouts on the substrates, were presented. The sample preparation and analysis methods, equipment and parameters were explained. The results obtained from the respective analyses of the samples will be provided in Chapter 4.

Chapter 4 Results and discussion

4.1 Introduction

In the previous chapter, the materials and methods used to produce and analyse the samples were described and presented. In this chapter, the results of the different analyses are presented and discussed in detail.

4.2 Powder blend 1

4.2.1 Single track analysis of powder blend 1

Laser powers of 100, 150, 170, 200 W, together with scanning speeds ranging from 0.4 to 1.8 m/s, were used to produce the single tracks. An example of continuous, semi-continuous and non-continuous single tracks produced from this powder blend is shown in Figure 58.

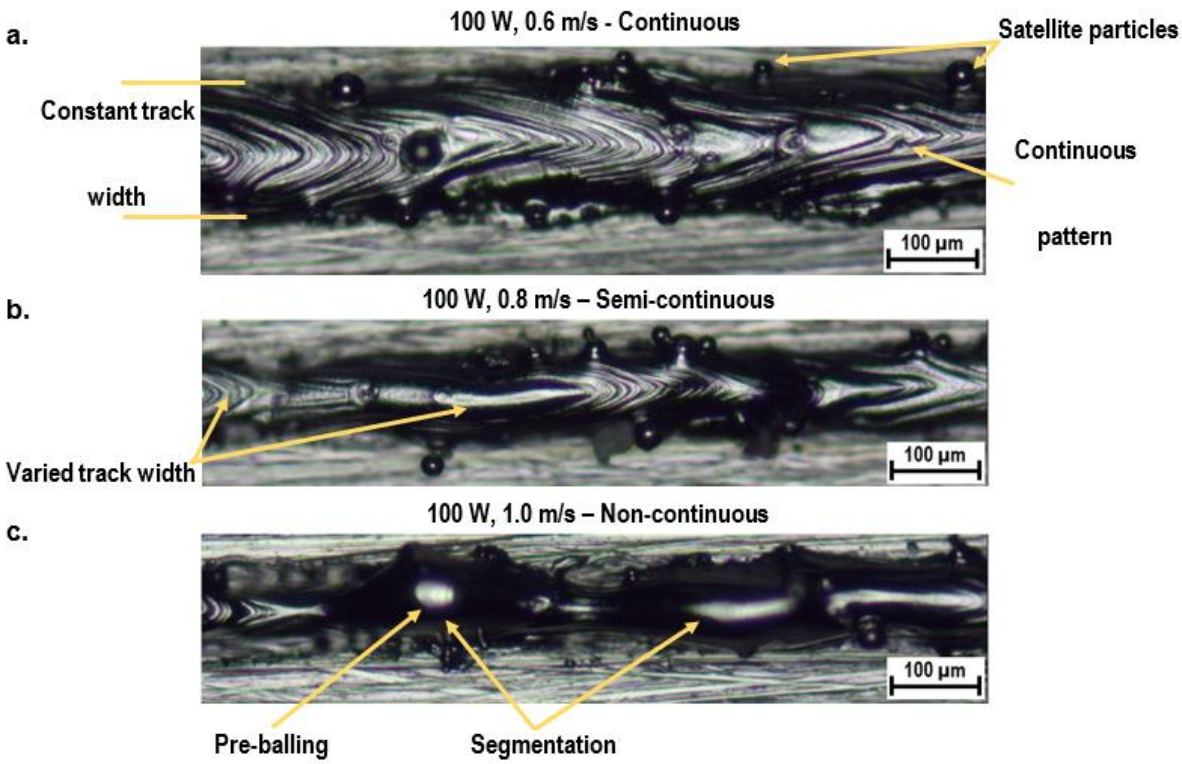

Figure 58. The typical morphologies of single tracks produced from PB 1.

From the top-view analysis, the process parameters that produced continuous and non-continuous single tracks were identified and displayed in Table 9. The green

blocks represent the continuous single tracks, while the yellow blocks represent continuous single tracks that were continuous, but with non-optimum track irregularities such as varied track width and irregular track morphology. The red blocks represent the non-continuous single tracks that exhibited irregularities, such as segmentation caused by the balling phenomenon.

Table 9. Summary of the PB 1 single-track continuity analysis

	Laser Power (W)			
	100	150	170	200
Scanning speed (m/s)	0.4	0.6	0.6	0.6
	0.5	0.8	0.8	0.8
	0.6	1	1	1
	0.7	1.2	1.2	1.2
	0.8	1.4	1.4	1.4
	0.9	1.6	1.6	1.6
	1	1.8	1.8	1.8

The single tracks produced at 100 W laser power (Figure 58(a)) were continuous at corresponding scanning speeds of 0.4 to 0.6 m/s. However, these single tracks exhibited irregularities such as the formation of satellite particles at their edges. For scanning speeds between 0.7 to 0.8 m/s (Figure 58(b)), the tracks had a varied track width, while pre-balling started to occur at scanning speeds above 0.8 m/s. At 150 W, the single tracks produced were continuous at a scanning speed range of 0.6 to 1.2 m/s. Scanning speeds between 1.2 to 1.4 m/s produced tracks with an irregular track width, while pre-balling became evident from scanning speeds higher than 1.4 m/s. The continuity of the tracks produced at 170 W ranged from 0.6 to 1 m/s before the track irregularities shown Figure 58(c) in took place. At the highest power of 200 W, the single tracks were continuous for scanning speeds of 0.6 to 1.2 m/s. Scanning speeds above 1.2 m/s resulted in irregular tracks that exhibited pre-balling.

As shown in Figure 58, single tracks produced using different scanning speeds at the same laser power can have different morphologies. This is due to the temperature dependant surface tension effect which tends to reduce the liquid melt pool to the

smallest surface area or energy state as it is deposited onto the substrate [148]. The linear energy density (power per selected speed) is higher at a lower scanning speed for any given laser power [139]. Therefore, the powder is exposed to the laser irradiation for a longer period at a lower scanning speed than at a higher scanning speed. The melt pool temperature will thus be higher at lower scanning speeds, resulting in a low melt pool viscosity and surface tension within the melt pool, resulting in the production of thick, deep-penetrated continuous tracks [149]. As the scanning speed increases for the same laser power, the melt pool temperature decreases and the surface tension and melt pool viscosity increase. The increased melt pool viscosity and surface tension tend to promote the production of thin and irregular single tracks that appear to be broken into different sections (pre-balling), as shown in Figure 58(c) [39]. Figure 59 illustrates the relationship between the linear energy density and the track width. As the linear energy density decreased, the track width decreased.

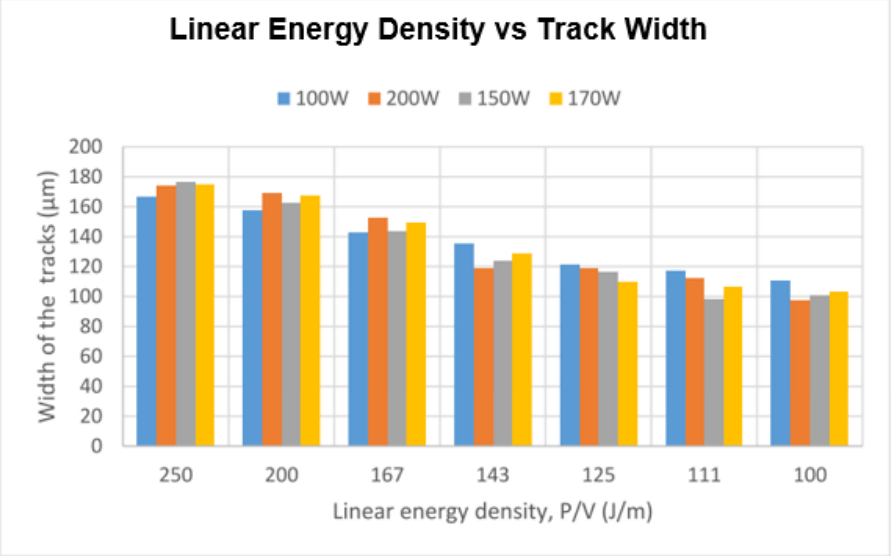

Figure 59. Plot of linear energy density vs track width

The relationship between the scanning speed and the track width can be seen in Figure 60. At low scanning speeds, the track widths are at their maximum, and they decrease with an increase in scanning speed. An increase in scanning speed results in a decrease in linear energy density and melt pool temperature, with a consequent increase in surface tension and melt pool viscosity, therefore decreasing the widths of the tracks.

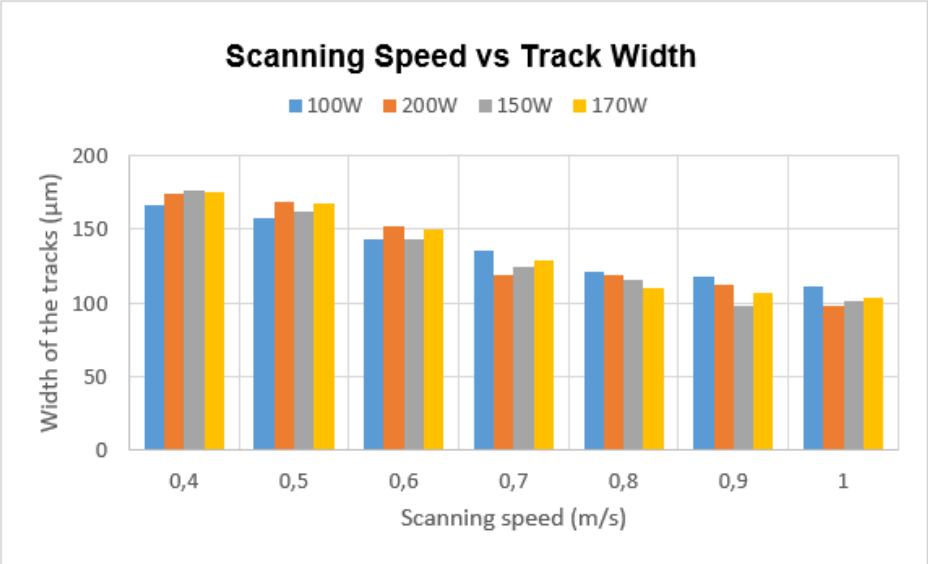

Figure 60. Plot of scanning speed vs track width

The cross-sectional views of the single tracks produced at maximum energy density for each laser power are shown in Figure 61.

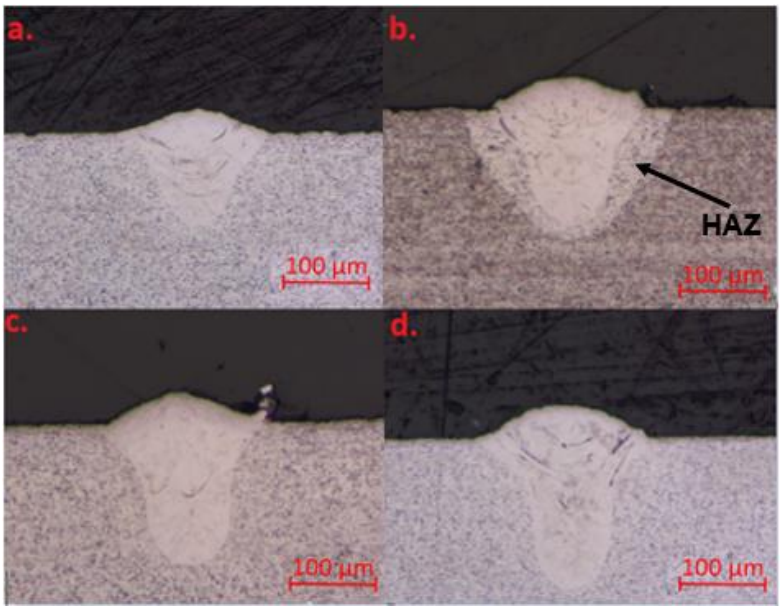

Figure 61. Cross-sectional views of single tracks produced at (a) 100 W, 0.4 m/s. (b) 150 W, 0.6 m/s. (c) 170 W, 0.6 m/s and (d) 200 W, 0.6 m/s

The penetration depth of the melt pool into the substrate can be observed by the formation of a semi-keyhole shape [137], [139]. The depth of this keyhole-shaped penetration is greater at a laser power of 200 W (Figure 61(d)) compared to that of

100 W (Figure 61(a)). It can be said that the penetration depth increases at a constant scanning speed as the laser power increases. This keyhole-shaped penetration is a direct result of the excessive laser irradiation that the powder was exposed to when producing these tracks; a greater volume of powder was melted, resulting in a deeper penetration into the substrate. Depending on the target application, this keyhole effect may be undesirable in DMLS-produced components because it leads to the formation of pores and irregular single tracks [39]. However, in the instance where parts with an increased density are required, the concentrated laser energy will promote the complete melting of the powders while also remelting the previous layers, thereby increasing the density of the part in-situ. The effect of the excessive laser irradiation can also be seen in Figure 61(b) where a heat-affected zone (HAZ) formed around the keyhole shape. This HAZ is a direct result of the combination of high laser power and low scanning speed, a combination that results in the excess heat being transferred to the surrounding area, thus forming the halo around the cross-section of the single track [39],[139]. During part production, the microstructure of the substrate (previously deposited layers) is a fine acicular α' microstructure. During the deposition of a new layer, the heat in the HAZ transforms the microstructure of the metal in the HAZ from a fine microstructure to a slightly coarser microstructure while the newly deposited layer and the material not affected by the HAZ consist of the fine acicular α' microstructure. This therefore leads to microstructural inconsistencies which translate into reduced mechanical properties such as strength and toughness [68].

The relationship between the penetration depth and scanning speed is graphically displayed in Figure 62. For any given laser power, the penetration depth is greater at a low scanning speed, and it decreases with an increase in scanning speed. The penetration depth is also dependent on the laser power - a higher laser power at a slow scanning speed will result in a much deeper penetration depth.

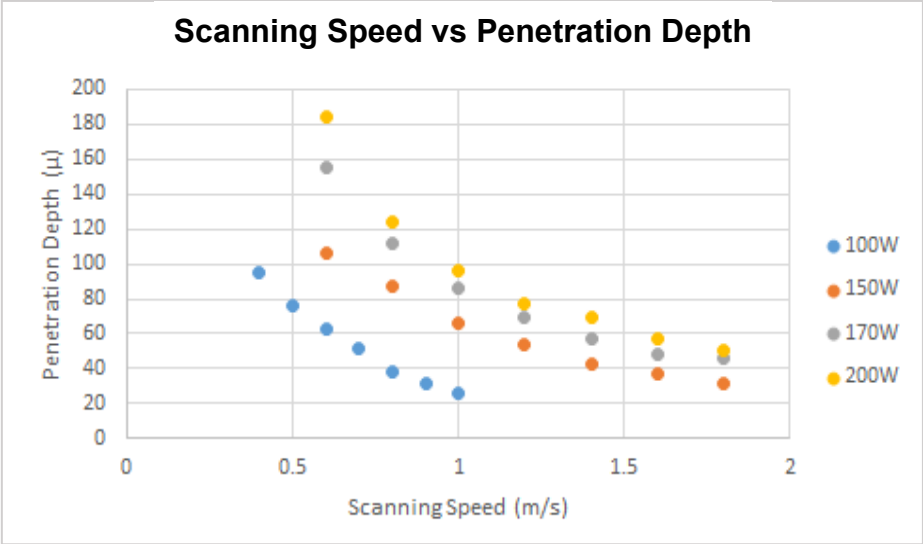

Figure 62. The relationship between scanning speed, penetration depth and laser power

Careful consideration must be taken when selecting the optimum process parameters for the DMLS process. The parameters need to be optimum to ensure the production of defect-free components. Through analysis of the results obtained, the combinations of laser power and scanning speed that produced the optimum process parameters were found to be 100 W with a corresponding scanning speed of 0.6 m/s (Figure 63(a)) and 200 W at a corresponding scanning speed of 1.2 m/s (Figure 63(b)). At these process parameters, the single tracks produced were continuous with a stable track width. The penetration depth of these tracks into the substrate resembled a semi-circular U-shape which is mandatory in the DMLS process to ensure defect-free components with good bonding into the substrate [39], [137], [139].

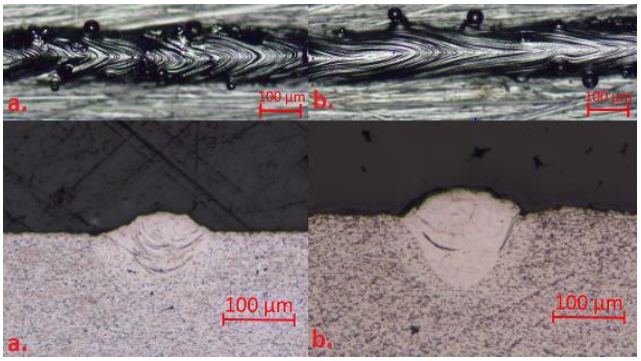

Figure 63. Single tracks produced at (a) 100 W; 0.6 m/s and (b) 200 W; 1.2 m/s.

The process parameter set that is suitable to produce single tracks with optimum track characteristics from a CP Ti and a 60Al-40V master alloy powder blend is 200 W and 1.2 m/s. Using these process parameters, the track width is more stable, and the track height is slightly greater than at 100 W and 0.6 m/s, which means that components will be built faster with these parameters. The higher power of this process parameter set is expected to result in a more homogeneous mixing of the alloying elements in the melt pool. The secondary process parameter set of 100 W and 0.6 m/s can still be used to produce components. However, dimensional accuracy may be a problem due to the unstable track width, and the production time will increase due to the height of the tracks. The difference in height of the tracks produced at different process parameters is shown in Figure 64. The graph shows there is no obvious relationship between the track height, scanning speed, and laser power.

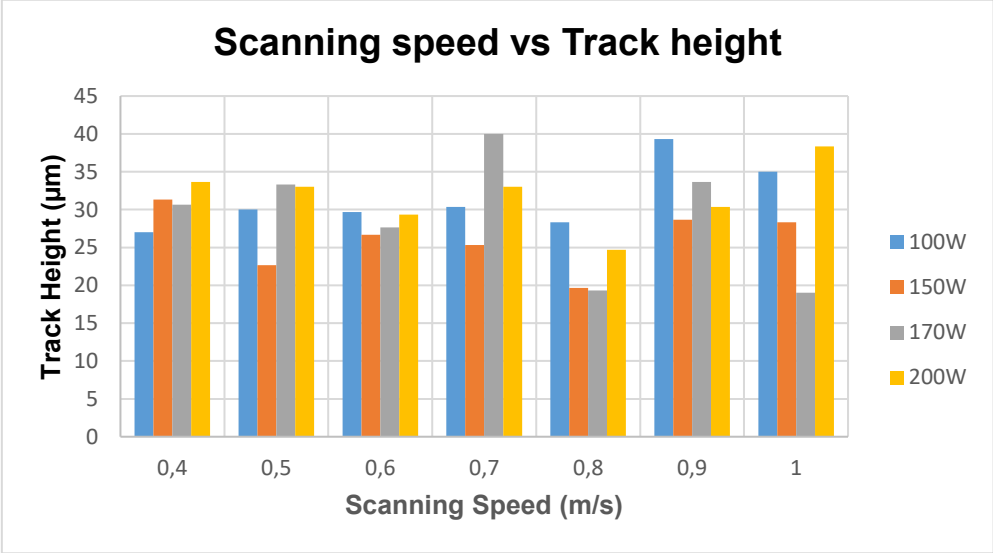

Figure 64. Plot of scanning speed vs track height at various laser powers.

4.2.2 Single- and double-layer analysis of powder blend 1

Analyses were conducted on the single and double layers produced from the process parameters identified in the single-track analysis of the respective powder blends. These analyses were aimed at understanding the effects of the hatch distance and re-scanning strategy on the layer morphology and homogeneity and the bonding relationship between the layers and the substrate.

Figure 65 and Figure 66 display the morphology of the layers at each hatch distance before and after the rescanning strategy (double scan). The single and double layers exhibited a similar kind of morphology; therefore, only the double layers are displayed for illustrative purposes.

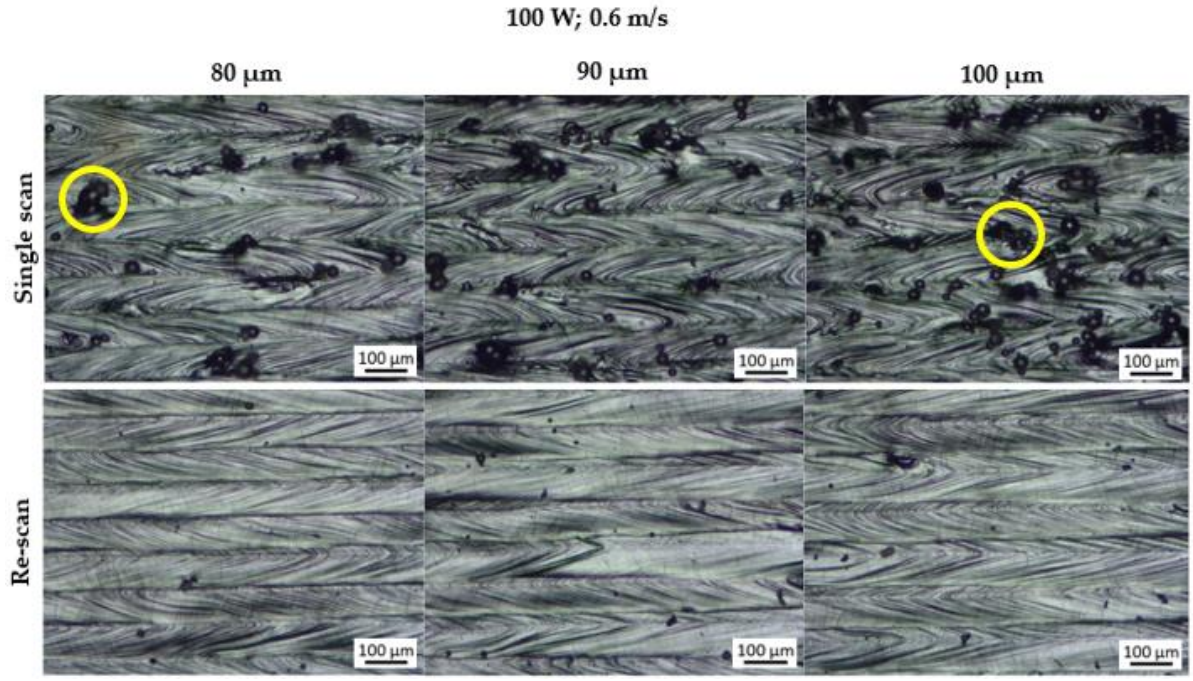

Figure 65. Optical micrographs of the top surface morphology of the double layers produced at 100 W, 0.6 m/s and hatch distances of 80, 90 and 100 µm.

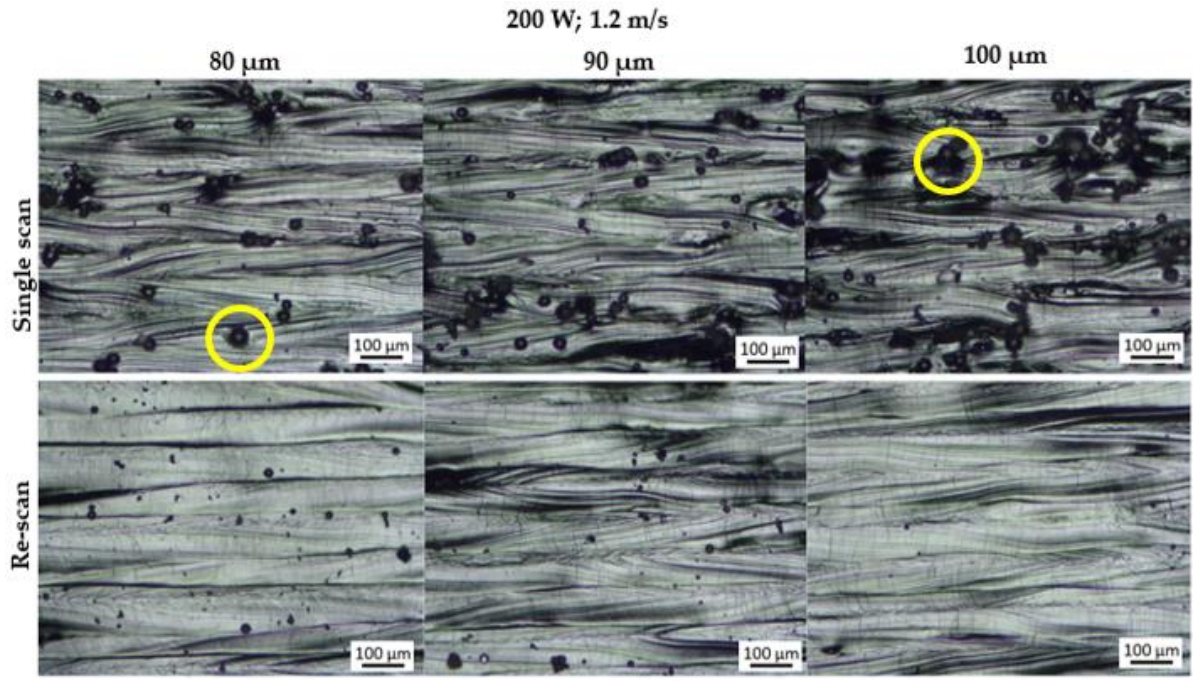

Figure 66. Optical micrographs of the top surface morphology of the double layers produced at 200 W, 1.2 m/s and hatch distances of 80, 90 and 100 µm.

The single-track analysis revealed that the single tracks exhibited satellites formed on their edges (Figure 58), which in turn resulted in satellites (encircled in yellow) forming on the surfaces of the single and double layers. This observation is in agreement with the findings of Yadroitsev et al. [2], where it was found that the surface morphology of the layers produced in LPBF depends on the characteristics of the single tracks. It was further observed that the layers produced at a hatch distance of 100 µm exhibited more satellites than those produced at 80 µm. Similarly, the findings from other studies also suggested that the number of satellite particles formed on a layer increases with an increase in the hatch distance [24], [150]. This is due to the incomplete powder melting at higher hatch distances because the single tracks overlap less with each other at a higher hatch distance in comparison to a smaller hatch distance thus reducing the cummulative energy density in the overlapping areas [2]. In a different study [151], these satellite particles had an adverse effect on the mechanical properties of the final 3D component. However, the rescanning strategy was effective in removing these satellite particles, ensuring a defect-free layer surface. Spatter particles are essentially imperfectly melted powder particles; hence, a second laser scan was able to melt and redistribute them into the layer completely. Yadroitsev et al. [2],

[152] explained that the difference between the thermophysical conditions of the powder and the solid material fueled the mechanism of removing these particles. They suggested that the absorbance of the solid material was lower than that of the powder material; therefore, in the second laser scan, the imperfectly melted powders absorbed more laser radiation, leading to complete melting and redistribution into the bulk material [152]. This observation by Yadroitsev et al. was confirmed by the observations and results obtained in the current study. The effect of this strategy is also illustrated in the SEM micrographs in Figure 67 of the double layers before and after the rescanning strategy.

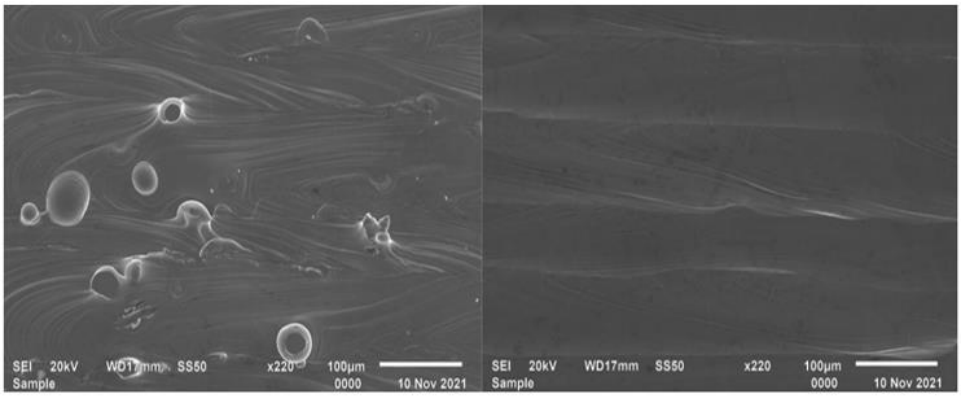

(a) (b)

Figure 67. SEM SEI micrographs of double layers produced in PPS 1 before (a) and after (b) rescanning.

Considering the average width of the tracks deposited from PPS 1 and PPS 2 (152 and 145 µm, respectively) [153], a hatch distance of 80 µm would allow a greater portion of the single tracks to overlap compared to hatch distances of 90 and 100 µm. The cross-sectional analyses of the double layers (Figure 68) indicate that the layers produced at a hatch distance of 80 µm did have a better track-to-track overlapping (binding) compared to those produced at 90 µm and 100 µm for both process parameter sets. It is worth mentioning that no gaps between the tracks and no delamination between the layers were observed throughout the range of hatch distances used for single- and double-layer production.

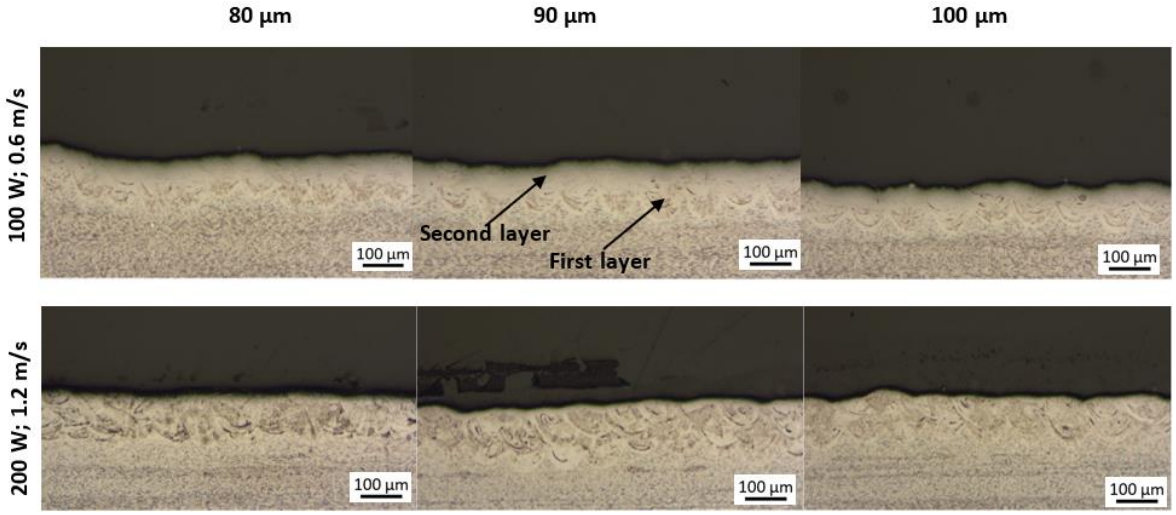

Figure 68. Cross-sectional views of double layers produced at 100 W; 0.6 m/s and 200 W, 1.2 m/s at hatch distances of 80, 90 and 100 µm

The effect of substrate denudation was observed in the cross-sectional analyses of the single and double layers. From Figure 69, the first few tracks that form the layer appear to be higher and wider than the tracks in the middle span of the layer. Similar studies [152], [154] suggest that the deposition of the first track will result in a denudation zone on the substrate during layer production. When the second track is deposited using a hatch distance that is less than the width of the denudation zone, it will then appear to be lower than the first track due to the decrease in available powder. Additionally, the last track in the layer will also be higher than the middle tracks because there is an excess of powder remaining in the powder bed available for the formation of this track on the periphery of the laser spot. Ultimately, the denudation effect results in dimensional inaccuracy and defects such as chains of pores within the final 3D component; therefore, an allowance for the variation of the track height should be made during the production of 3D components [2], [152], [154]. However, in the current study, defects such as porosity, solidification cracks and layer delamination were not observed in the sectioned areas of the samples. The absence of these defects signifies an optimum combination of process parameters suitable for the DMLS production of 3D components [150].

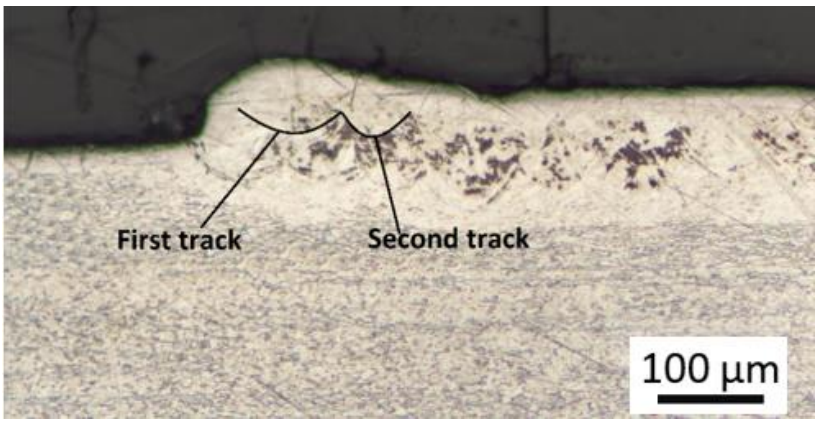

Figure 69. Denudation effect observed on a cross-section of the double layers

An indication of the degree of homogeneity of the in-situ alloyed Ti6Al4V layers can be seen in the single- and double-scan micrographs in Figure 70.

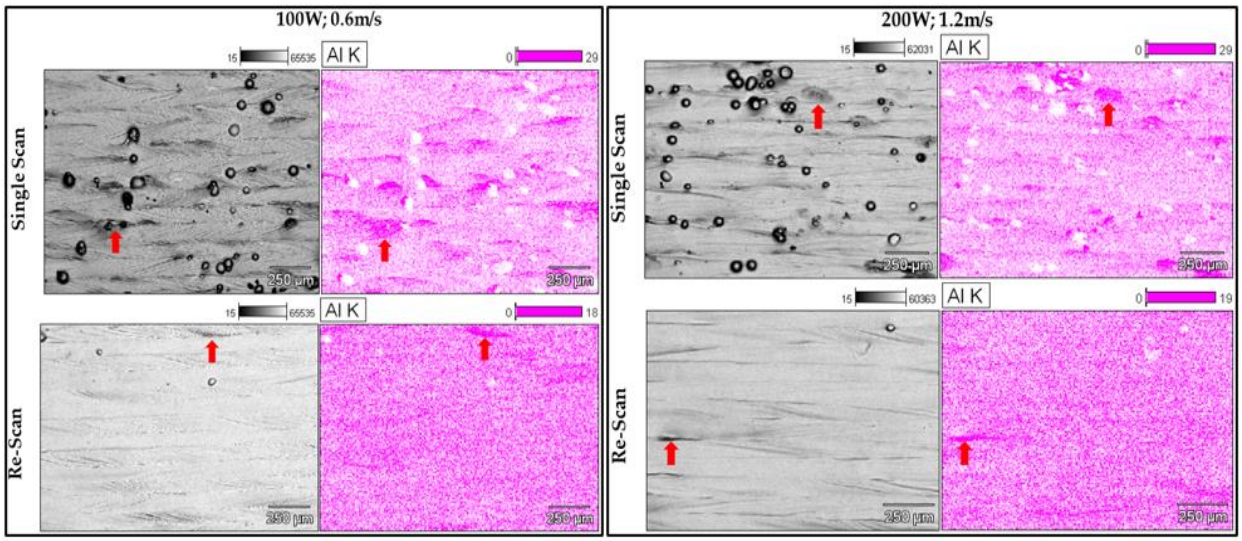

Figure 70. BEI images and Al K EDS maps of double layers at 100 W, 0.6 m/s and 200 W, 1.2 m/s for a hatch distance of 80µm

From the relative intensity scale (top right of the micrographs), a significant Al inhomogeneity exists mostly at the edges of the single tracks that formed the layer (indicated by red arrows). Two factors could contribute to this inhomogeneity. Firstly, Chan et al. [156] found that it could be due to the uneven distribution of energy by the laser beam, which created the melt pool from the metal powders. This uneven distribution, paired with the non-stationarity of the energy source, resulted in a non-uniform temperature in the melt pool when a single track was produced. The

temperature of the melt pool would be higher at its centre and lower at its edges [2]. Therefore, the degree of melting and mixing would be less thorough at the edge of the melt pool due to the relatively lower temperature. Additionally, the high solidification rate typical of the DMLS process promoted inhomogeneity by not allowing adequate time for diffusion before solidification [157]. The inhomogeneity could also be due to insufficient mixing of the powder blend before it was used in the DMLS process. The MA powder had an irregular morphology (Figure 38), which could limit the degree of powder blending and lead to the consequent inhomogeneity of the powder blend. Simonelli et al. [8] stated that the inhomogeneity of the starting material would cause inhomogeneity in the final product, which could only be removed by post-sintering processes. As expected, the rescanning strategy did homogenise the alloy by melting and redistributing the satellites into the bulk of the alloy. Nevertheless, areas relatively higher in Al concentration (indicated by the red arrows) can still be seen in the elemental mapping micrographs in Figure 70. It should be possible to improve the homogeneity of the alloy by improving the homogeneity of the powder blend before it is used in the DMLS process. This could be achieved by replacing the irregularly shaped MA powder with spherical MA powder, allowing more homogenous mixing of the powders.

4.2.3 Three-dimensional parts of powder blend 1

After the single-track and layer analysis, two PPS had been developed and used to produce the three-dimensional parts. Table 10 below provides a summary of the two process parameter sets.

Table 10. The process parameter sets employed for the production of 3D parts from PB 1.

Parameters	Laser power (W)	Scanning speed (m/s)	Hatch distance (µm)	Layer thickness (µm)
PPS 1 (PB 1)	100	0.6	80	60
PPS 2 (PB 1)	200	1.2	80	60

During the conventional DMLS production of the Ti6Al4V alloy, the PA metal powder is laser-melted to form a melt pool, which then rapidly solidifies [72]. Rapid

solidification is caused by the high cooling rate (up to 108 K/s) typical of the DMLS process [57], [158]. The resulting microstructure is a binary (α+β) microstructure consisting of acicular martensitic α needles (laths) within columnar prior-β grains [27]. The microstructures obtained from the polished and etched AB specimens produced from the powder blend are shown in Figure 71.

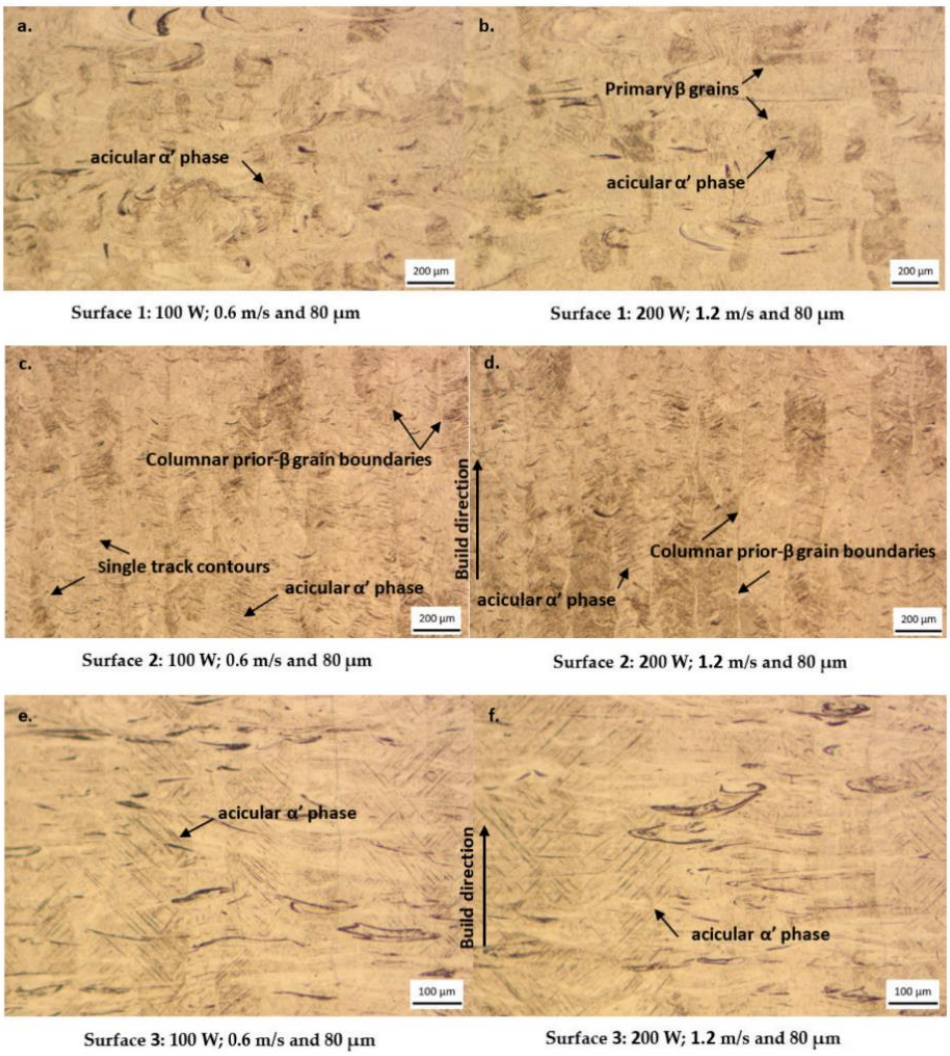

Figure 71. Microstructures of the cross-sectioned, polished and etched surfaces of the AB Ti6Al4V specimens produced from powder blend 1. (a, b) Surface 1, x-y plane. (c, d) Surface 2, x-z plane, along the building direction. (e, f) Surface 3, y-z plane, along the building direction.

The microstructures of the sectioned AB cubes generally consisted of a fine needle-like acicular martensitic α' phase contained within columnar prior-β grains, typical of the additively manufactured Ti6Al4V alloy, as reported by other authors [8], [57], [159]. This martensitic microstructure is distinctive for DMLS-produced parts due to

the rapid cooling and solidification rates found in this process [113], [114]. The microstructure of Surface 1 (Figure 71(a), (b)) consists of the acicular α' phase within the primary β grains. Some single-track contours can be seen in the microstructures shown in Figure 71 (c) and (d). From these micrographs, it is evident that the hatch distance set to produce these specimens was optimum, as the u-shape single track contours overlap completely with each other. This observation is consistent with the one made in the double-layer cross-sectional analysis shown in Figure 68. The columnar prior-β grains, which have grown in a direction parallel to the building direction, can be seen on these micrographs. Within these columnar prior-β grains, fine acicular martensitic α' laths are visible. Like the micrographs of Surface 1 and Surface 2 of the cubes, fine acicular martensitic α' laths within the prior-β grains were identified on the micrographs of Surface 3 (Figure 71(e), (f)). No layer delamination or interlayer pores were observed. The micrographs shown in Figure 71 demonstrate the microstructural anisotropy found in the AB Ti6Al4V parts. Since the mechanical properties of Ti6Al4V parts are highly dependent on the microstructure [61], this could result in some anisotropy in the mechanical properties of the built part.

The large temperature gradients that exist during the DMLS production of Ti6Al4V parts normally induce thermal residual stresses within the produced parts. These residual stresses can cause the parts to warp or deform when they are removed from the building platform [59]. Therefore, the tensile test specimens were stress-relieved (SR) at a temperature of 650 °C with a soaking period of three hours. In this study, the SR treatment was effective in alleviating the internal thermal residual stresses, and no deformation or warping of the parts was observed when they were wire-cut from the substrate. The annealing heat treatment performed at 940 °C for two hours on the tensile test specimens caused the decomposition of the martensitic α' phase into a more ductile microstructure, which generally consisted of a lamellar α+β phase (Figure 72) with retained prior-β grains.

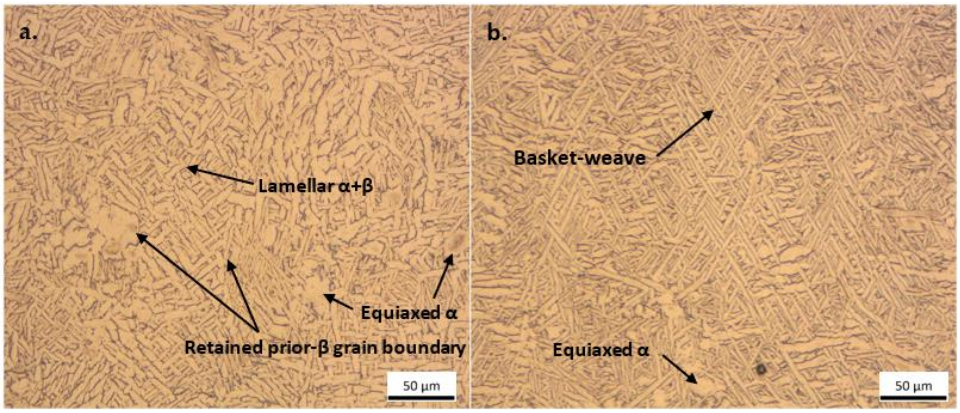

Figure 72. Microstructures obtained after stress relieving at 650 °C for three hours and annealing at 940 °C for two hours for (a) PPS 1 and (b) PPS 2.

The surface morphology and the variation in surface homogeneity of the parts produced from this powder blend can be seen in Figure 73(a), (b).

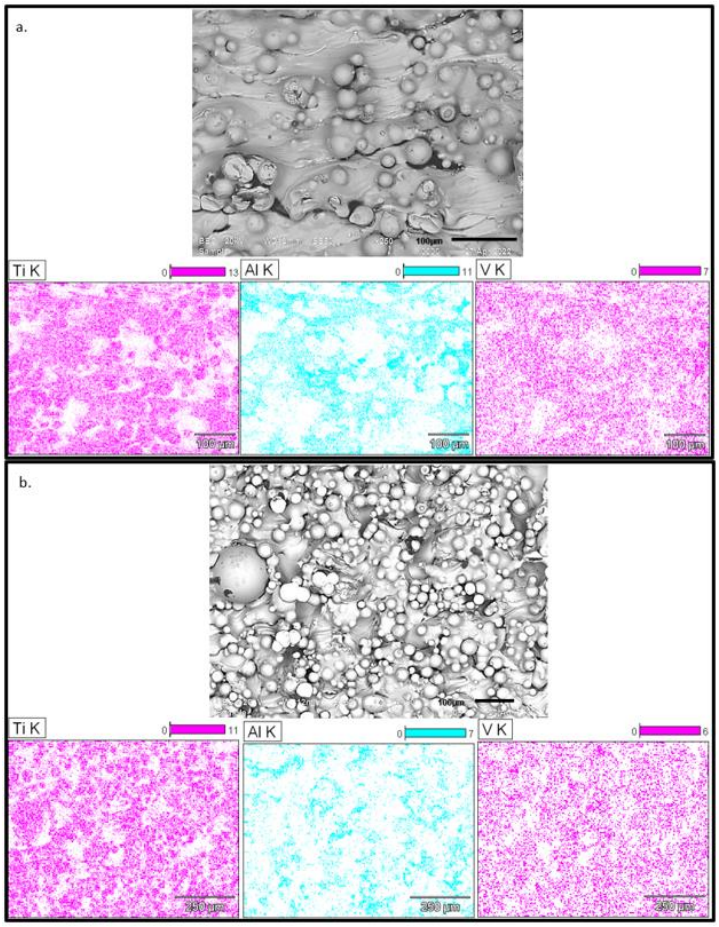

Figure 73. BEI image and Ti, Al and V K EDS maps of the morphology and homogeneity of the surfaces of cubes produced in (a) PPS 1 and (b) PPS 2.

Ideally, DMLS-produced parts should have a high surface quality and require minimum surface post-processing [57]. Due to the intrinsic characteristics of the DMLS process, the parts usually exhibit varying surface quality with respect to surface homogeneity for in-situ alloyed parts [65]. The different constituents of the powder blend cause the variation in surface homogeneity when they agglomerate as imperfectly melted powders on the surfaces of the parts due to the excessive heat energy from the laser beam.

In a powder bed consisting of a PA feedstock, each individual powder particle is essentially already an alloy consisting of the composition required in the final built part [127]. When these PA powders are imperfectly melted, they agglomerate on the surfaces of the part during layer-wise production. These imperfectly melted PA powders do not result in micro-inhomogeneity on the surface of the parts, as they bear the same composition as the bulk of the part being produced. This is not the case for a powder blend intended for in-situ alloying. The powders surrounding the part being built do not have the same composition as the bulk of the in-situ alloyed part. Therefore, the excess heat energy from the melt pool may reach any of the randomly distributed constituents of the powder blend, which can agglomerate on the surface of the part as imperfectly melted powders, resulting in micro-inhomogeneity on the surface of the part. An SEM-EDS analysis conducted on the AB surfaces of the cubes produced from PPS 1 revealed that the imperfectly melted powders that agglomerated on the outer surfaces of the cubes are indeed the different constituents of the powder blend, as seen in Figure 73(a), (b). This observation warrants the need for surface post-processing on parts that were in-situ alloyed in the DMLS process. Partially molten Ti powder particles can be clearly identified by their spherical morphology in the BEI images of the surfaces of the AB cubes Figure 73(a), (b). In contrast, the MA powders cannot be directly identified. Still, a variation in contrast can be seen. This variation, in contrast, can be attributed to the inconsistent composition within the analysed area. A Ti powder particle that has a particle size in the upper limit of the particle size range is visible in Figure 73(b). The Ti K EDS map in Figure 73(b) confirmed that this powder particle was indeed a Ti powder particle. A great deal of surface inhomogeneity can be seen in the elemental EDS maps performed on the surfaces of the cubes, which is a clear indication of the inhomogeneity of the surfaces of the in-situ alloyed parts.

The chemical composition of the produced Ti6Al4V cubes is provided in Table 11.

Table 11. ICP-OES composition determined for cubes produced with PPS 1 and PPS 2 compared with the ASTM F2924-14 specification

Element	PPS 1	PPS 2	ASTM F2924–14
Ti	91.4	90.8	Remainder
Al	4.73	5.11	5.5–6.75 ± 0.4
V	3.53	3.72	3.5–4.5 ± 0.15
O	0.19	0.21	0.2 ± 0.02
N	0.00433	0.00619	0.05 ± 0.02
Fe	0.07	0.05	0.3 ± 0.1

The major obstacle anticipated with the in-situ alloying of the Ti6Al4V alloy was the evaporation of the Al during powder fusion due to its low melting temperature of 660.2 °C [133], [160], [161]. The use of the Al–V MA powder was intended to restrain the Al evaporation by virtue of the higher resultant Al–V alloy melting temperature compared to the low melting temperature of the elemental Al powder. However, the results obtained from the ICP-OES analysis suggest that some evaporation of the Al powder did take place during production. As shown in Table 11, the measured Al concentrations were 4.73 and 5.11 wt.% for PPS 1 and PPS 2, respectively. Taking into consideration the actual concentration of the Al in the MA powder (54.8 wt.%, see Table 5), PPS 1 and PPS 2 yielded evaporation percentage values of 13.7% and 7.2%, respectively. The PPS 1 Al concentration was below that specified in the standard, while PPS 2 had an Al value within the tolerance specified in ASTM F2924–14 [109]. These values are lower than the Al evaporation value (23.3%), which has been reported in a similar in-situ study by Dong et al. [133].

The unexpected occurrence was the decreased V content present in the AB Ti6Al4V alloy. With reference to the starting composition of the MA powder (see Table 5), it is evident that PPS 1 and PPS 2 yielded V evaporation values of 18.66% and 14.29%, respectively, which are similar to the V evaporation values (17.5%) reported by Dong et al. [133]. This decrease in V content can be attributed to the evaporation of the V_2O_5 compound that formed during sintering as a result of the reaction between the V and the O_2, as has been presented by Dong et al. [133].

The oxygen and nitrogen concentrations were within the limits specified in the standard. Oxygen and nitrogen are interstitial elements in Ti6Al4V, and their concentration should always be controlled not to exceed 0.2 and 0.05%, respectively, because an excess in these elements would lead to an alloy with increased strength but decreased ductility [105]. These compositional results demonstrated that it was indeed possible to in-situ alloy a Ti-MA powder blend to produce a part with the Ti6Al4V alloy composition. However, an appropriate concentration of the starting feedstock and the careful selection of a process parameter set would be required to produce the correct alloy.

The results obtained from the CT scans of the 3D cubes produced with PPS 1 and PPS 2 are displayed in Figure 74 and Figure 75, respectively. DMLS-produced parts are usually affected by two types of pores: gas pores and LOF pores [57], [74]. Gas pores are usually randomly distributed in the part and are typically spherical with a diameter ranging between 1 and 100 µm. The LOF pores are usually larger than the gas pores (100–150 µm), and they tend to take up a planar (perpendicular to building direction) and irregular shape within the layers of the parts [57], [74], [146]. The cubes produced from PPS 1 had some randomly distributed ovoid pores with diameters less than 90 µm, as seen in Figure 74(b). The diameters of these randomly distributed pores were less than 100 µm, and they can be considered to be gas pores, although they were not completely spherical [74]. The remainder of the pores were irregularly shaped, with diameters ranging from 100 to 245 µm, and were LOF pores. Figure 74(c) displays the largest LOF pore found in the cube. This pore had a diameter of 245 µm and exhibited small, rounded inclusions that formed on the surface of the cavity of the pore (yellow dotted circles). These inclusions resemble the morphology of the spherical elemental Ti powder, which was used in the powder blend (Figure 38). It is safe to assume that this LOF pore resulted from the lack of fusion of the powder blend constituents.

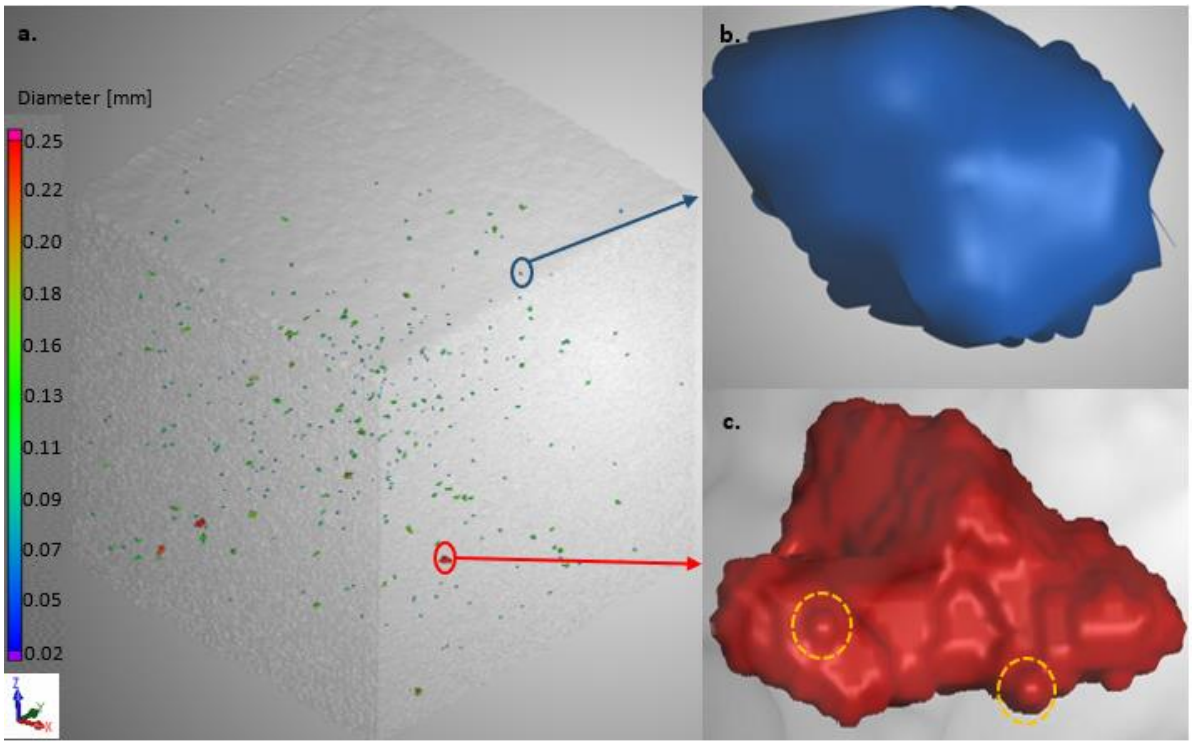

Figure 74. Micro CT scans of the AB Ti6Al4V cubes produced from PPS 1: (a) the overall porosity distribution within the cube, (b) gas pore, (c) lack-of-fusion pore. The colour codes of the pores displayed in (b) and (c) correspond to the diameter scale shown in (a)

The cube produced from PPS 2 (Figure 75) contained a mixture of gas pores and LOF pores similar to those seen in the cube produced in PPS 1. According to the diameter scales displayed in Figure 74(a) and Figure 75(a), the sizes of the gas and LOF pores in the cubes produced in PPS 1 and PPS 2 were in the same size range. The sizes of the gas pores produced with PPS 2 ranged from 30 to 90 µm, while the LOF pores, on the other hand, had diameters ranging from 100 to 330 µm. However, despite the pores that were contained in the cubes, the overall density of the produced cubes was very satisfactory. The CT scanning results revealed that the cubes produced from PPS 1 and PPS 2 yielded total densities of 99.9%. These density values are higher than the in-situ alloyed Ti6Al4V density values reported by other authors [133], [160].

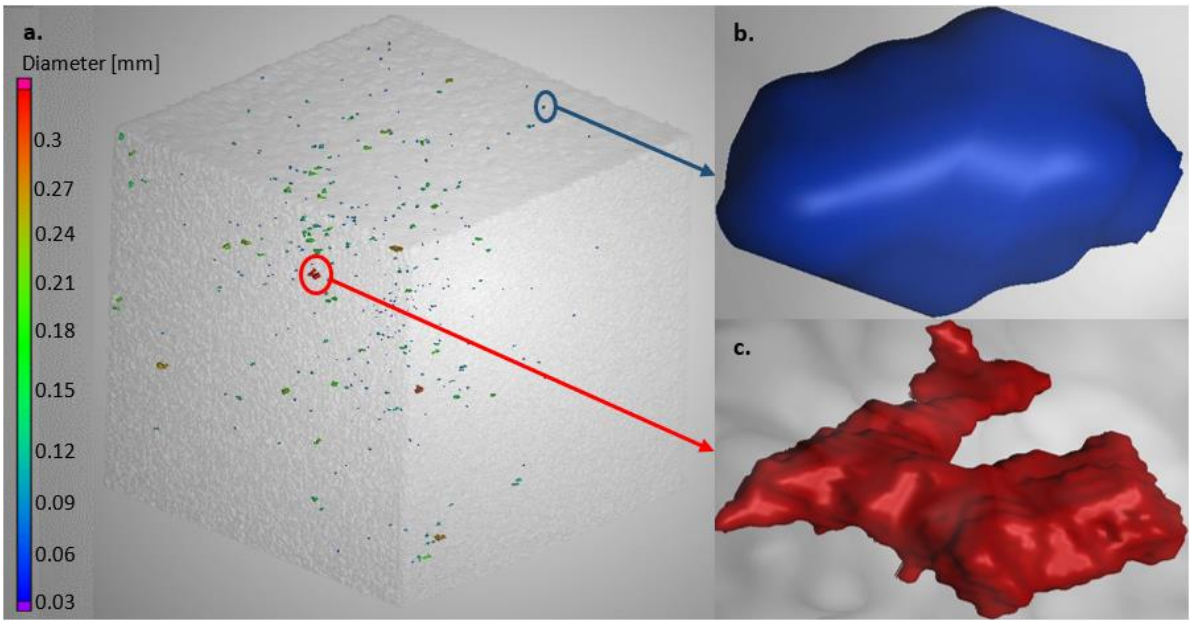

Figure 75. Micro CT scans of the AB Ti6Al4V cubes produced from PPS 2: (a) the overall porosity distribution within the cube, (b) gas pore, (c) lack-of-fusion pore. The colour codes of the pores displayed in (b) and (c) correspond to the diameter scale shown in (a)

The mechanical properties obtained from the stress-relieved and annealed tensile test specimens and the properties specified in ASTM F2924-14 [109] are displayed in Table 12. From Table 12, the tensile specimens produced from the two process parameter sets yielded mechanical property values that were higher than the specified values for AM Ti6Al4V parts. A study conducted by Vrancken et al. [84] focused on the effect of different heat treatments on the microstructure and the resultant mechanical properties of DMLS-produced Ti6Al4V. In this study, Vrancken reported values of 948 ± 27 MPa, 899 ± 27 MPa and 13.59 ± 0.32% for the ultimate tensile strength (UTS), yield strength (Ys) and elongation at break (ε), respectively, for tensile specimens that were duplex annealed at 940 and 650 °C for one and two hours, respectively. Becker et al. [61] reported UTS and ε values of 871 MPa and 11.5%, respectively, for Ti6Al4V specimens duplex annealed at 950 and 700 °C for one and two hours, respectively. The values obtained in the current study are comparable with the values reported by Vrancken et al. and Becker et al. However, in this study, a single anneal HT was used instead of a duplex anneal HT. Depending on the target application, a single anneal HT can be used if a part with high strength and adequate ductility is required. The duplex anneal HT, on the other hand, can be

used if a part that has a lower tensile strength and higher ductility is required [61], [84]. The mechanical properties of the alloy are comparable to the mechanical properties of the wrought Ti6Al4V alloy presented in a review article by Teixeira et al. [58]. From the results obtained, it is evident that the pores present in the cubes displayed in Figure 74 and Figure 75 did not have a significant effect on the mechanical properties of the Ti6Al4V alloy produced from the two process parameter sets.

Table 12. Mechanical properties obtained from the heat-treated tensile specimens produced by PB 1 compared to the ASTM F2924–14 standard.

Property	Process parameter set 1	Process parameter set 2	ASTM F2924–14
UTS (Mpa)	932.3	942.9	895
Ys (Mpa)	932.2	942.9	825
ε (%)	12.9	17	10
Area reduction (%)	30.6	35.9	15

The fracture surfaces of the tensile specimens displayed a few areas with brittle features and some LOF pores within an overall dominant ductile fracture surface, as seen in Figure 76. The overall fracture surface of the machined tensile specimen presented in Figure 76(a) displays the ductile crack initiation and shear lip (final fracture) areas of the fractured tensile specimen. The crack initiation zone appears to be circular and more fibrous than the shear lip area, which is an indication that a slow transverse propagation of cracks occurred in this region. A shear lip area, which is inclined to the crack initiation and propagation plane, can be seen around the failure nucleation area, indicating that pronounced necking occurred before the final, fast shear-type fracture occurred. These features observed from the overall fracture surface are representative of a ductile type of fracture. A higher magnification of the fibrous failure nucleation area (Figure 76(b)) revealed a surface with randomly propagated micro-cracks and micro-voids (secondary cracks) that formed during the application of the tensile load. In Figure 76(c), spherical unmolten Ti powders resulting in a LOF pore can be seen. This observation confirms the assumption that

the small, rounded inclusions observed in Figure 76(c) were indeed unmolten spherical Ti powders, resulting in a LOF pore. Randomly scattered dimples within a ductile fibrous region can be seen in Figure 76(d). These dimples are indicative of void nucleation and coalescence, which is common in ductile fracture [162]

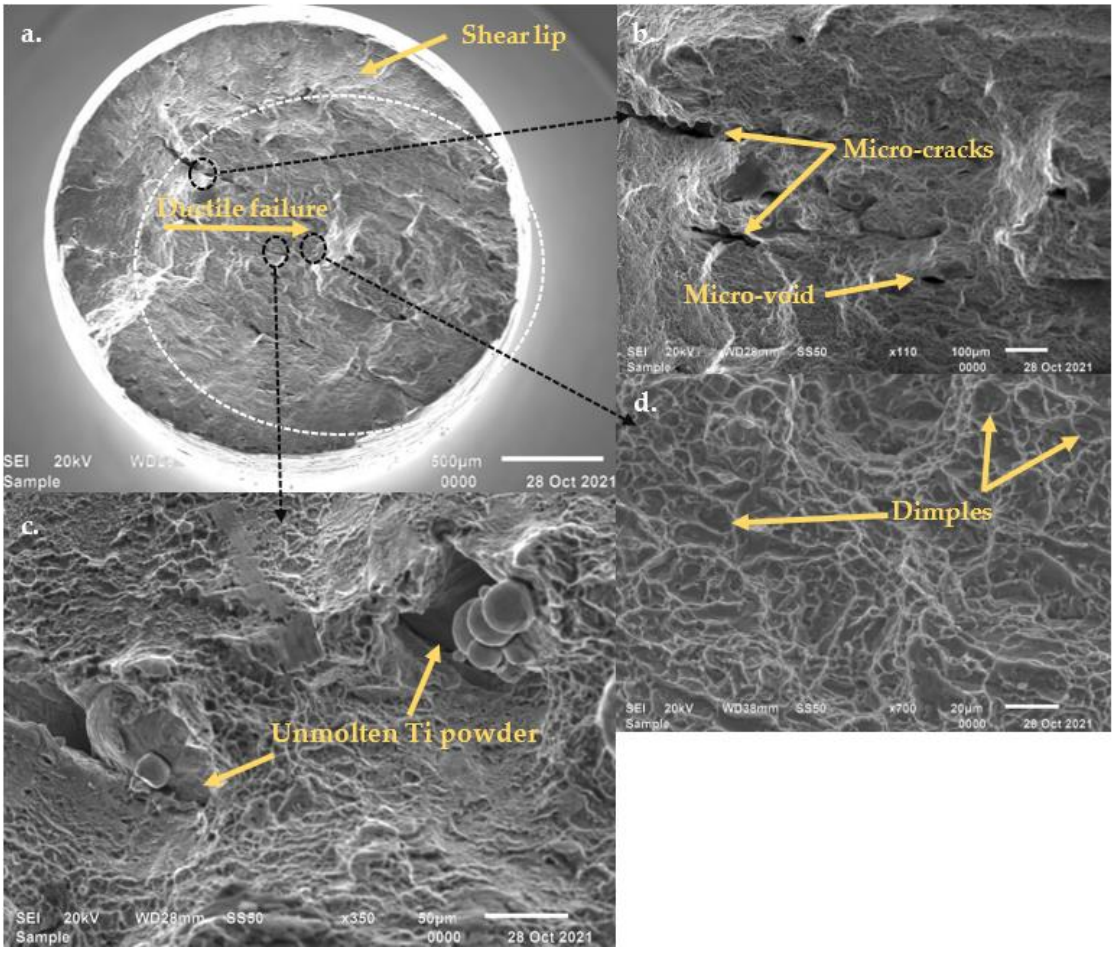

Figure 76. SEM SEI micrographs of the fracture surface of a tensile test specimen produced by PPS 1: (a) the overall fracture surface showing the shear lip and ductile failure in the central part of the fracture surface (crack initiation), (b) micro-cracks and voids, (c) unmolten Ti powder particles, (d) ductile region with dimples

.

The MA powder used in this study was irregularly shaped and not spherical, as is the requirement for powders used in AM processes [163]. The individual powder particles within a feedstock interact and exert frictional forces onto each other; the morphology

of the individual powders, therefore, directly affects the flowability and spreadability of the powder feedstock [33]. Spherical powders are the preferred feedstock for AM processes due to their good flowability when they are delivered onto the powder bed by the recoater arm. Irregularly shaped powders within the feedstock negatively affect the flowability and spreadability of the powder, resulting in the deposition of uneven layers during production and, ultimately, porosity in the components. The recommendation is that a Ti-MA powder blend consisting of plasma-spheroidised MA powders be used to improve the flowability and packing density of this powder blend.

4.3 Powder blend 2

4.3.1 Single track analysis of powder blend 2

Laser powers of 100, 150, 170, 200, 250 and 300 W, together with scanning speeds ranging from 0.4 to 1.8 m/s, were used to produce the single tracks. The top view of an optimum single track should be continuous with no evident defects and irregularities, such as a varied track width or broken sections along the length of the track (balling). Examples of continuous, non-continuous and non-optimum single tracks that exhibited bead formation and the balling effect are given in Figure 77(a), (b) and (c), respectively.

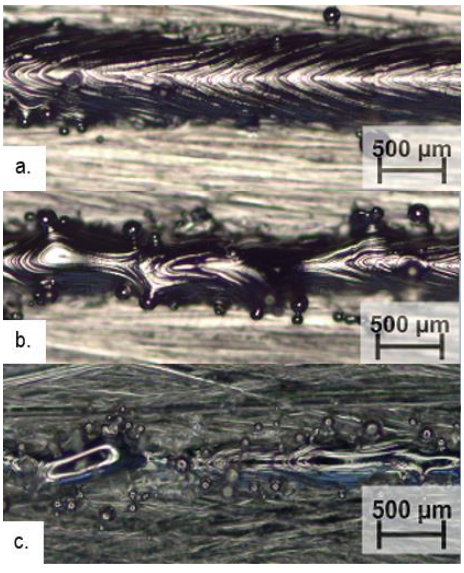

Figure 77. Optimum continuous single track produced at 250 W, 0.6 m/s (a), non-continuous single track produced at 250 W, 1.0 m/s (b), and a non-optimum bead formation single track produced at 200 W, 1.8 m/s (c)

From the top-view analysis, the process parameters that produced continuous and non-continuous single tracks were identified and displayed in Table 13 below. The green blocks represent the continuous single tracks, while the yellow blocks represent continuous single tracks that were continuous, but with non-optimum track irregularities such as varied track width and irregular track morphology. The red blocks represent the non-continuous single tracks that exhibited irregularities, such as broken sections caused by the balling phenomenon.

Table 13. Summary of the PB 2 single-track continuity analysis.

	Laser Power					
	100	150	170	200	250	300
Scanning speed (m/s)	0.4	0.6	0.6	0.6	0.6	0.6
	0.5	0.8	0.8	0.8	0.8	0.8
	0.6	1	1	1	1	1
	0.7	1.2	1.2	1.2	1.2	1.2
	0.8	1.4	1.4	1.4	1.4	1.4
	0.9	1.6	1.6	1.6	1.6	1.6
	1	1.8	1.8	1.8	1.8	1.8

The continuity of the single tracks produced at the 100 W laser power ranged between scanning speeds of 0.4 to 0.5 m/s (Figure 77a). At 0.6 m/s, the tracks were continuous, but their morphology was irregular and not satisfactory (Figure 77(b)). The morphology of the single track affects the morphology of the layer and, ultimately, the properties of the final part. It is imperative that the morphology of the single track is taken into consideration when conducting single-track parameter investigations [137]. For scanning speeds above 0.6 m/s, the single tracks were not continuous (Figure 77c). For laser powers of 150, 170 and 300 W, the single tracks were continuous for scanning speeds between 0.6 and 0.8 m/s. At the scanning speed range between 1 and 1.2 m/s, the single tracks were continuous, but with the irregularities shown in Figure 77(b). Scanning speeds above 1.2 m/s produced single tracks that had irregular track widths, which indicated the effect of surface tension and the pre-balling phenomenon [151]. At 200 and 250 W, the continuity of the single tracks ranged between 0.6 and 0.8 m/s. Non-optimum single tracks were formed at scanning speeds of 1–1.4 m/s at 250 W laser power. Scanning speeds of 1–1.8 m/s

and 1.6–1.8 m/s at laser powers of 200 and 250 W respectively, yielded non-continuous single tracks.

The width of the tracks decreased with increasing scanning speed (Figure 78); this observation has also been reported in other single-track studies [139], [153], [164]. It is due to the relationship between the energy density (power per selected speed) and the surface tension. The surface tension is a temperature-dependent property between the melt pool and the substrate that tends to decrease the surface area of the melt pool [165]. At a lower scanning speed for any laser power, the energy density is high, resulting in more heat energy being transferred onto the metallic powder and the substrate. The surface tension on the substrate will be lower due to the thermal conduction from the heat energy source, allowing the resulting melt pool to flow freely and forming a continuous stream that will solidify into a single track. As the scanning speed increases gradually, the heat energy decreases, therefore increasing the surface tension between the melt pool and the substrate, resulting in a reduction in the surface area of the melt pool and, ultimately, a thin, solidified single track. In extremely high scanning speed cases, the surface tension will tend to break the melt pool into segments, resulting in thin cylindrical beads that can be further reduced to a series of round individual balls. This is a result of the balling phenomenon [166], [167].

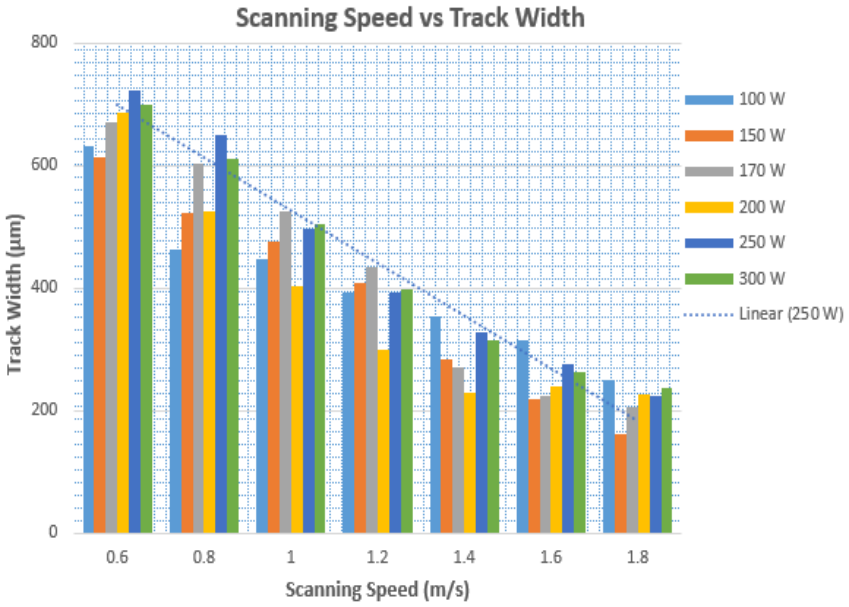

Figure 78. Plot of scanning speed vs track width

The effect of the energy density can also be seen in the cross-section of the single tracks (Figure 79). At an excessively high scanning speed, the penetration of the single track into the substrate can take up a shape that resembles a keyhole (Figure 79a.). At a high energy density, the dynamic viscosity of the melt pool is low, and a thermocapillary recirculating flow is set up in the melt pool due to the change in the surface tension between the melt pool and the substrate [151]. This recirculating flow results in the accelerated penetration of the melt pool into the substrate [151]. Since the temperature of the melt pool is highest at the centre and lower at the edges of the melt pool, the penetration resembles a keyhole shape with the deepest penetration at the centre. The keyhole penetration is undesired in the DMLS production of parts. It can lead to pore formation in the final component when the vapour pockets formed in the deeply penetrated melt pool collapse [2], [29]. At an adequate energy density, the penetration shape of the single track into the substrate can resemble a semi-circular U-shape, which signposts a good combination of laser power and scanning speed (Figure 79(b)). This kind of penetration occurs when the energy density is sufficient to allow the heat transfer within the powder bed to occur through normal absorption, conduction and convection heat transfer methods without any boiling or vaporisation of the melt pool [39]. This type of conductive mode is highly desired in the DMLS process as it results in adequate bonding between the track and the substrate. A low energy density will not be sufficient to melt the metal powders and weld them into the substrate, resulting in a single track that has poor or no penetration into the substrate (Figure 79)).

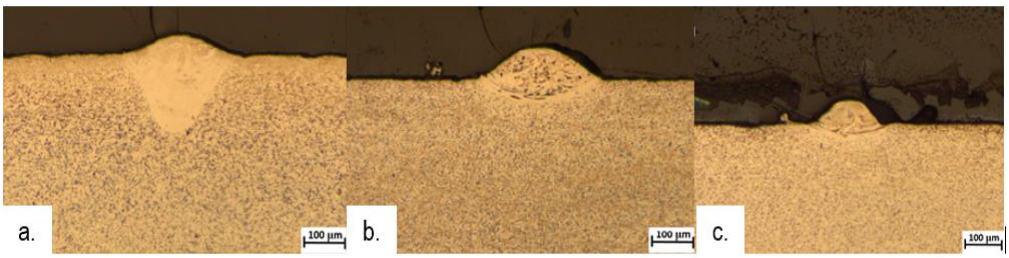

Figure 79. Keyhole formation at 170 W, 0.6 m/s (a), semi-circular U-shape at 200 W, 0.6 m/s (b), and insufficient substrate penetration at 200, 1,8 m/s (c)

The results of the cross-sectional analysis that was conducted on the single tracks that were considered to be optimum in Table 13 are presented in Table 14. As in Table 13, the process parameters highlighted in green were optimum, while those in red were considered non-optimum and consequently disqualified. At 100 W and scanning speeds between 0.4 and 0.5 m/s, the single tracks had an optimum U-shape penetration, but the penetration depth was not satisfactory. The track height and angle of contact of these tracks were satisfactory. At 150 W and corresponding scanning speeds of 0.6 and 0.8 m/s, the single tracks exhibited a keyhole (0.6 m/s) and semi-keyhole (0.8 m/s) penetration into the substrate. The penetration depth of the single track produced at 0.6 m/s was excessive, which is typical of this kind of penetration [150], and the track height was poor, owing to the excessive penetration of this single track into the substrate. The single track produced at 0.8 m/s had a fairly good penetration depth and track height despite the formation of the semi-keyhole penetration shape. The angle of contact of the single tracks produced at 150 W, 0.6 and 0.8 m/s, was greater than 90°. The continuous single tracks produced at 170 W and corresponding scanning speeds of 0.6 and 0.8 m/s exhibited a keyhole penetration shape with an excessive substrate penetration depth and poor track height. The angle of contact was greater than 90°. The cross-sections of the single tracks produced at 200 and 250 W and corresponding scanning speeds of 0.6 and 0.8 m/s exhibited an optimum semi-circular U-shape penetration with a good penetration depth and track height. The single tracks produced at these process parameters had an optimum contact angle greater than 90°. At 300 W and corresponding scanning speeds of 0.6 and 0.8 m/s, the single tracks had an optimum semi-circular U-shape penetration. The penetration depth of the single track produced at the corresponding scanning speed of 0.6 m/s was good, and that of the single track produced at 0.8 m/s was not satisfactory. The track height and angles of contact for the single tracks produced at both process parameters were greater than 90°.

Table 14. Summary of the single-track cross-sectional analysis

Process parameter	Penetration shape	Penetration depth	Track height	Contact angle
100 W, 0.4 m/s	Semi-circular	21 (Poor)	35 (Good)	≥ 90
100 W, 0.5 m/s	Semi-circular	19 (Poor)	35 (Good)	≥ 90
150 W, 0.6 m/s	Keyhole	74 (Excessive)	26 (Poor)	≥ 90
150 W, 0.8 m/s	Semi-keyhole	38 (Good)	36 (Good)	≥ 90
170 W, 0.6 m/s	Keyhole	111 (Excessive)	30 (Poor)	≥ 90
170 W, 0.8 m/s	Keyhole	83 (Excessive)	29 (Poor)	≥ 90
200 W, 0.6 m/s	Semi-circular	54 (Good)	45 (Good)	≥ 90
200 W, 0.8 m/s	Semi-circular	52 (Good)	30 (Poor)	≥ 90
250 W, 0.6 m/s	Semi-circular	35 (Good)	36 (Good)	≥ 90
250 W, 0.8 m/s	Semi-circular	31 (Good)	30 (Poor)	≥ 90
300 W, 0.6 m/s	Semi-circular	39 (Good)	44 (Good)	≥ 90
300 W, 0.8 m/s	Semi-circular	30 (Poor)	35 (Good)	≥ 90

From the single-track analyses, process parameters that produced single tracks that exhibited an optimum combination of track continuity and the required cross-sectional characteristics were identified at laser powers of 200, 250 and 300 W at the corresponding scanning speed of 0.6 m/s. However, a light halo can be seen on the etched cross-section of the single track produced at 300 W and 0.6 m/s (Figure 80(c)). This halo is a heat-affected zone and an indication of the excessive energy density that the powder and substrate were exposed to during the production of the single track [139], [168].

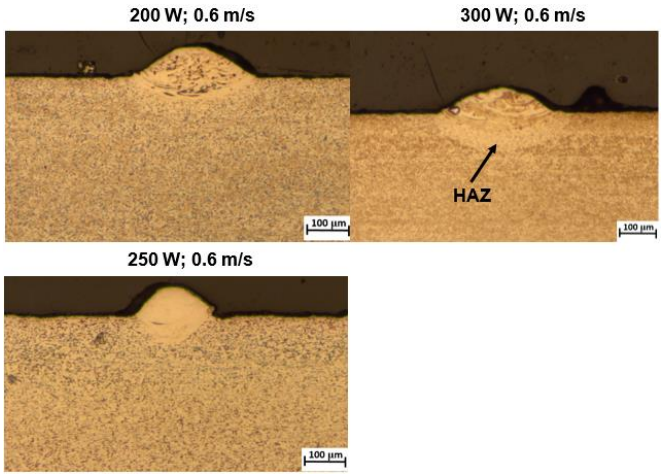

Figure 80. Cross-sectional views of the optimum single tracks produced at 200 W, 0.6 m/s, 250 W, 0,6 m/s and 300 W, 0.6 m/s.

Since the elemental powder blend used in this study consists of elemental Al powders, the chosen process parameters need to give off minimum heat energy while not compromising the quality of the single track. The excessive heat energy given off by the 300 W and 0.6 m/s process parameters could potentially cause accelerated evaporation of the low melting point Al powder. For this reason, this process parameter was disqualified from the analysis. The process parameters that were considered optimum from the analyzed results are 200 and 250 W at the corresponding scanning speed of 0.6 m/s. It is anticipated that the 200 W, 0.6 m/s process parameter will result in a better conservation of the elemental Al powder due to its lower heat energy compared to that of the 250 W, 0.6 m/s process parameter set. The top and cross-sectional views of these single tracks are presented in Figure 81. These process parameters were used to produce single and double layers.

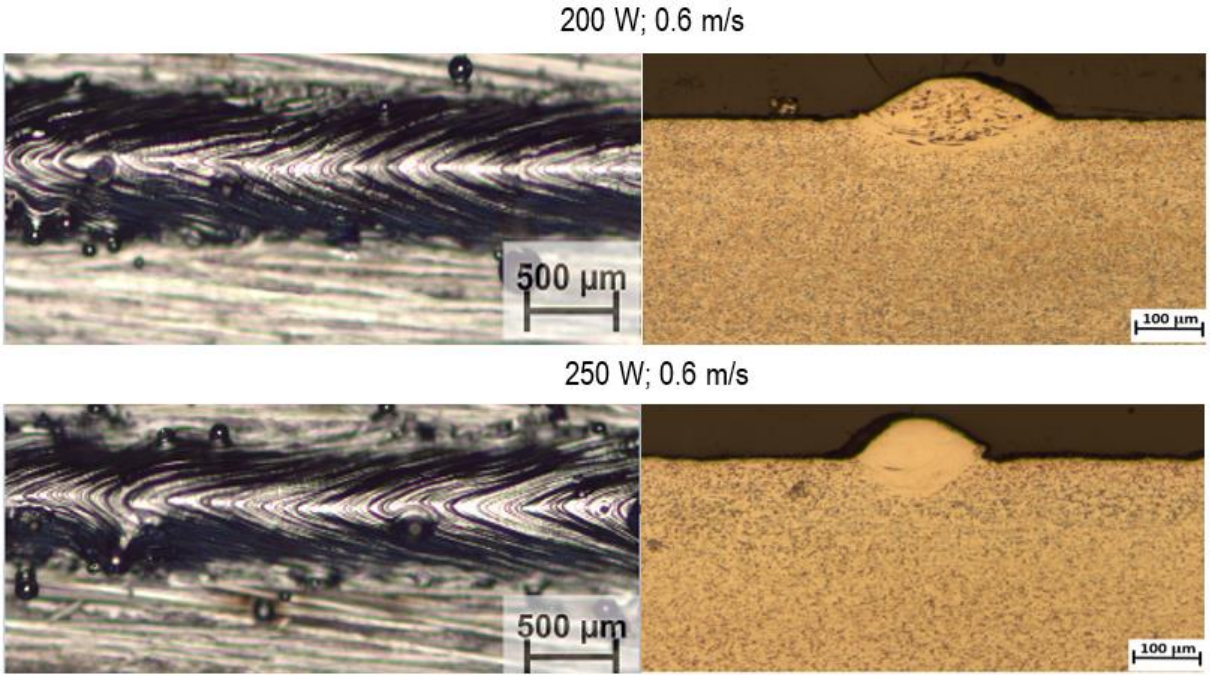

Figure 81. The optimum single tracks produced at 200 W, 0.6 m/s and 300 W, 0.6 m/s

4.3.2 Single- and double-layer analysis

The morphology of the layers that were achieved before and after the rescanning strategy is presented in Figure 82. The morphology of the single layers was identical to that of the double layers. Additionally, a much clearer indication of the morphology, homogeneity, and bonding relationship of the layers can be obtained from multiple layers than from a single layer. Therefore, the results presented will be based on the production of the double layers.

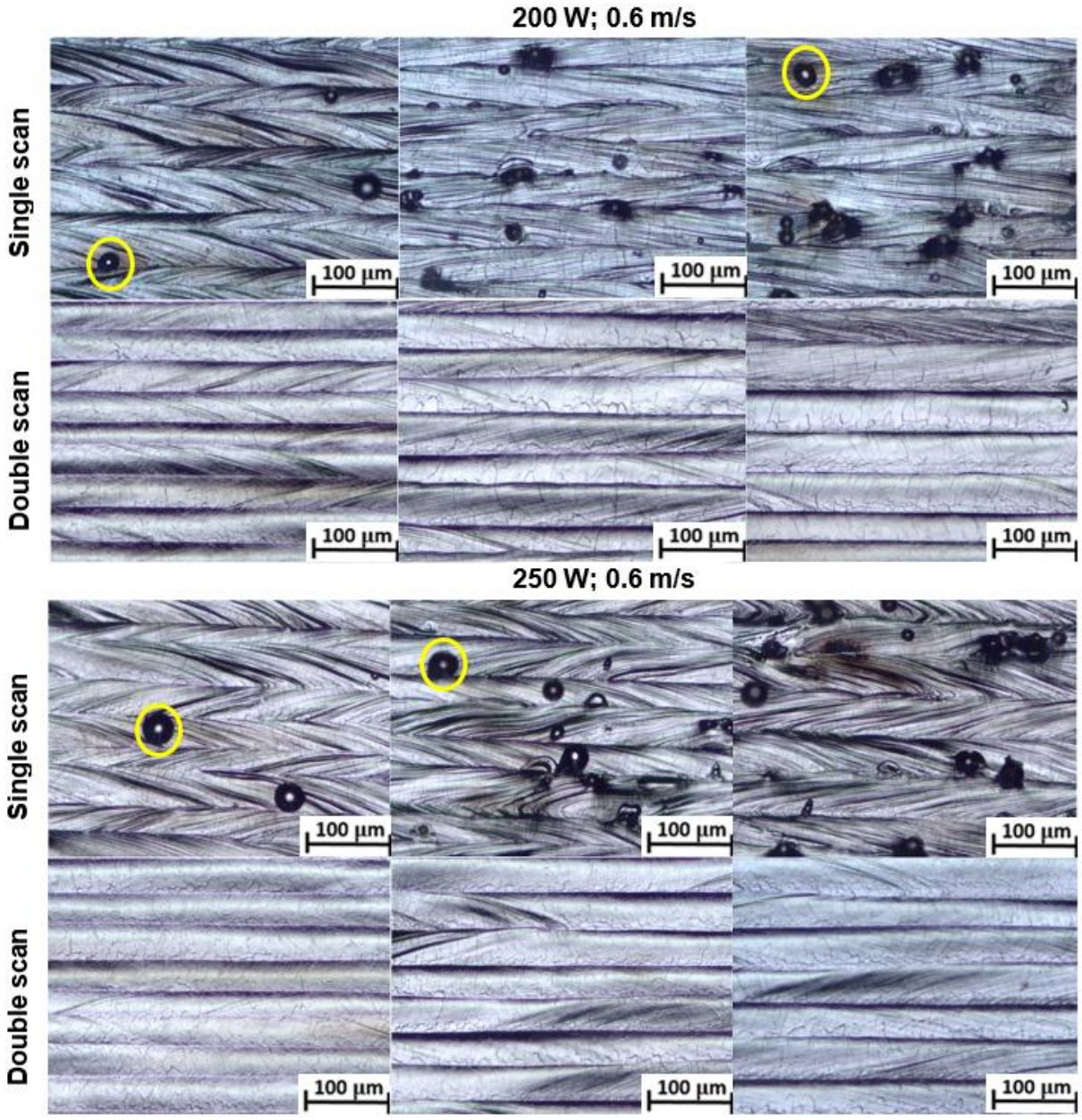

Figure 82. The morphology of the single and double layers before and after the rescanning strategy

The single-scanned double layers exhibited satellite particles at the edges of the super-positioned single tracks (encircled in yellow). Krakhmalev [150] reported that the number of satellite particles formed on the surface of the layers increased with the increasing hatch distance. This can be clearly seen in Figure 82 as it was also observed in Figure 65 and Figure 66. More satellite particles were formed on the surface of the layers produced at a hatch distance of 100 µm compared to those formed on the surface of the 80 µm hatch distance. These satellite particles are essentially just imperfectly melted powder that formed on the periphery of the single tracks [2], [151]. During single-track production, the uneven distribution of the laser beam radiates more energy at the centre of the single track than at the edge of the single track [24], [156]. Therefore, the powder at the edge of the single track will not be exposed to the same amount of energy as the powder at the centre [24], resulting in imperfectly melted powder at the edge of the track that becomes spheroidised due to the effect of the surface tension. Since the morphology of the layers is dependent on the morphology of the single tracks [2], the layers will exhibit satellite particles at the edge of the super-positioned single tracks. The rescanning strategy could re-melt these satellite particles and redistribute them into the bulk of the layer material.

The effect of the varied hatch distances on the bonding and overlapping of the single tracks can be seen from the edges of the super-positioned single tracks in Figure 83. At the hatch distance of 80 µm, the overlapping of the single tracks is much greater than that of the 100 µm hatch distance. Yadroitsev [169] stated that the value of the hatch distance should not be greater than the average width of the single track to obtain sufficient bonding between the single tracks. Care should be taken not to select a hatch distance that is a great fraction smaller than the track width as the amount of melted powder decreases as the hatch distance decreases. Although this would result in a smoother surface, it could also potentially increase production time [2].

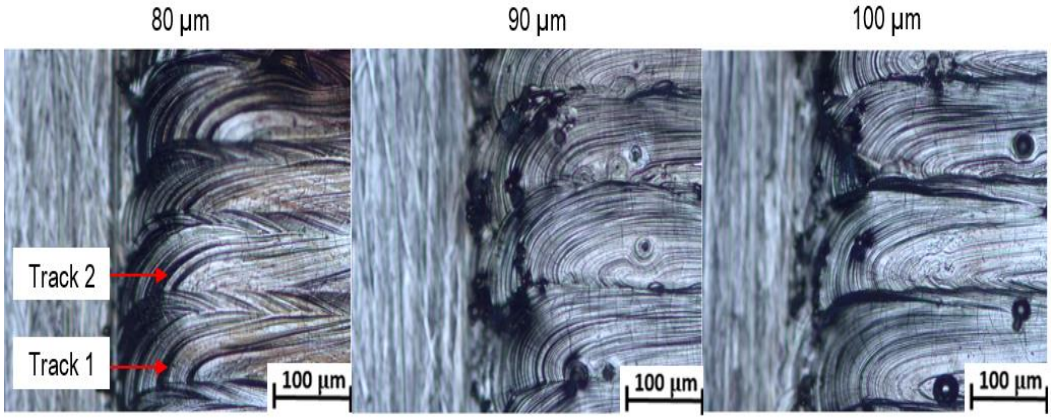

Figure 83. Top view of the bonding relationship of the super-positioned single tracks

The same bonding relationship that was observed in Figure 83 was observed in the cross-sectional analysis of the double layers (Figure 84). The layers produced at the 80 µm hatch distance had a greater track-to-track bonding compared to the cross-sections of the layers produced at greater hatch distances. Defects such as intra-layer porosity and delamination of the layers were not seen in this analysis.

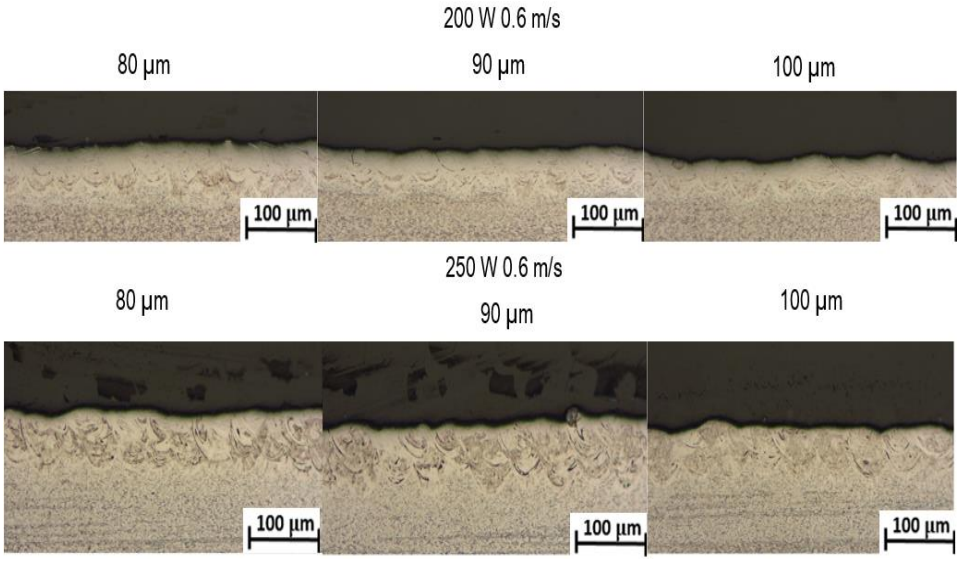

Figure 84. Cross-sectional view of the double layers

The homogeneity of the layers before and after the rescanning strategy is shown in Figure 85. It was expected to be difficult to obtain good material homogeneity due to the elemental nature of the powder blend used in this study. However, the homogeneity of the material before the rescanning strategy was applied was quite

fair, although areas that are rich in Al can be seen on the surface of the layer. This can be attributed to the low melting point and specific density of the elemental Al in the melt pool. The molten Al tends to rise above the molten Ti and V; hence, there are areas rich in Al [170]. The distribution of the Ti and V in the bulk material was fair, although there are areas that are rich in V. The rescanning strategy was able to redistribute the Al metal into the bulk of the alloy, resulting in a homogenous alloy.

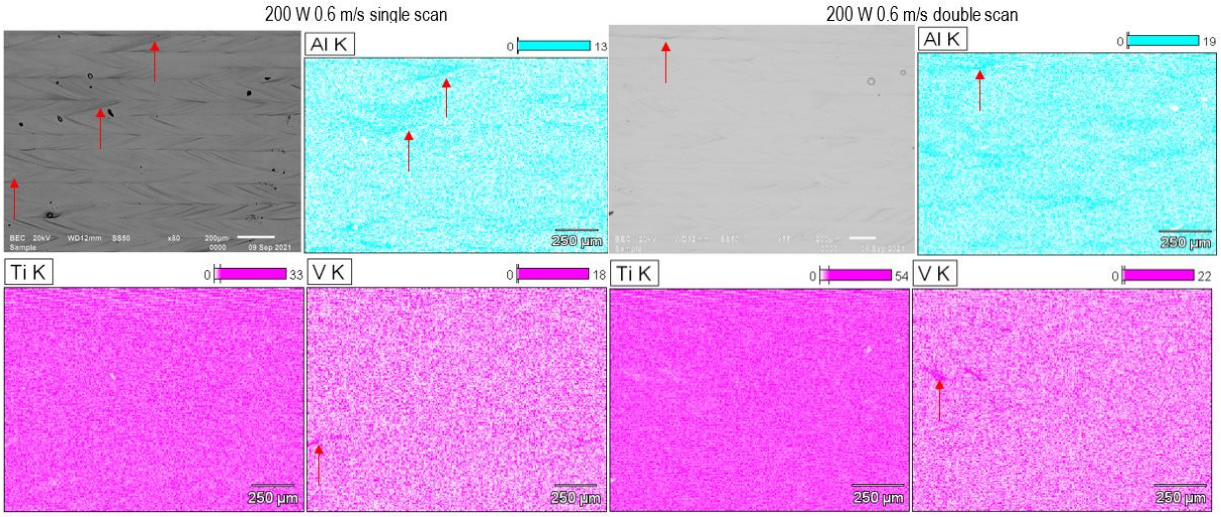

Figure 85. BSE images and Ti, Al and V K EDS maps of double layers at 200 W, 0.6 m/s at a hatch distance of 80µm

4.3.3 Three-dimensional parts of powder blend 2

After the single-track and layer analysis, two PPS had been developed and used to produce the three-dimensional parts. Table 15 below provides a summary of the two process parameter sets.

Table 15. The process parameter sets employed for the production of 3D parts from PB 1.

Parameters	Laser power (W)	Scanning speed (m/s)	Hatch distance (µm)	Layer thickness (µm)
PPS 3 (PB 2)	200	0.6	80	60
PPS 4 (PB 2)	250	0.6	80	60

The high cooling rate typical of the DMLS process (up to 10^8 K/s) results in the rapid solidification of the molten pool into the bulk of the alloy during the production of the Ti6Al4V alloy. This rapid solidification results in a binary (α+β) alloy microstructure that is dominated by a metastable martensitic α phase [57], [158]. Figure 86 displays the microstructures obtained from the polished and etched surfaces of the AB Ti6Al4V cubes.

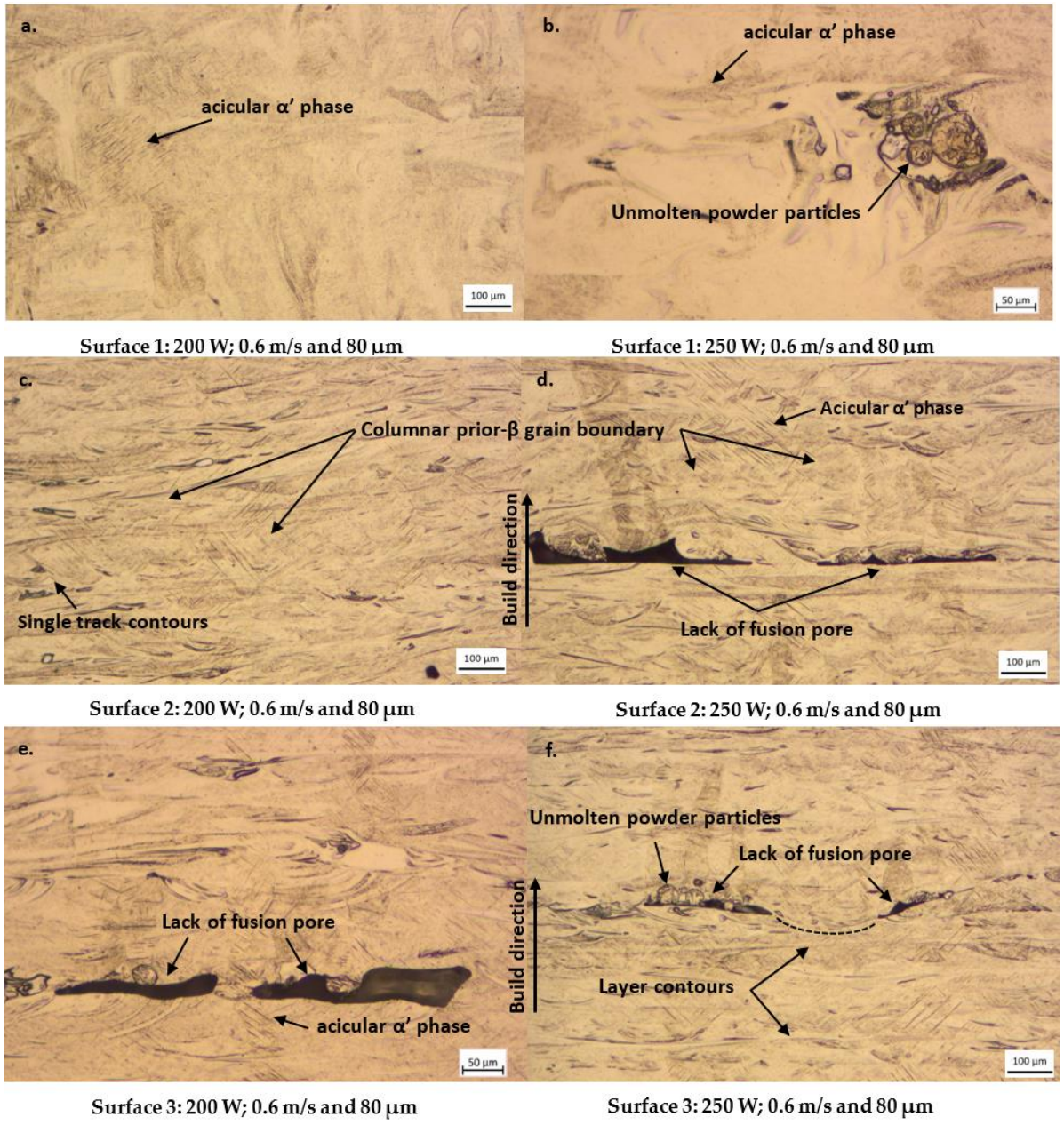

Figure 86. The microstructures of the cross-sectioned, polished, and etched surfaces of the AB Ti6Al4V specimens. (a–b) scanning surface, (c–d) surface 2 parallel to the BD, (e–f) surface 3 parallel to the build direction

The microstructures of the AB cubes were generally dominated by martensitic α-phase needles, which were contained within prior-β grains. Figure 86(a–b) displays the microstructure of the scanning surface of the AB cubes. The metastable acicular martensitic α-phase needles, which formed due to the rapid cooling from the β phase, can be seen [158]. Additionally, unmolten powders are visible on the surface microstructures of the cube produced at PPS 4 (Figure 86(b) and (f)), which may result in localised chemical inhomogeneity within the part. Prior-β grains that span parallel to the build direction are visible in Figure 86(c–d). These prior-β grains form due to the epitaxial grain growth from the previous layer as the heat is conducted from the scanning surface to the previously deposited layers [61]. Within these prior-β grains, martensitic α needles that are inclined at an angle of 45° (approx.) can be seen. U-shaped single-track contours that overlap completely with each other are visible on these surfaces, which signposts optimum hatch distance selection. The LOF pores seen within the contours of the deposited layers (Figure 86(d–f)) have some powder particles agglomerated around them, which suggests that the powders did not completely melt due to insufficient laser energy or a misfit between the interacting powder particles due to their different morphologies. The contours of the deposited layers that span perpendicular to the build direction can be seen in Figure 86(f).

The martensitic microstructure is usually accompanied by high residual stresses within the built part. These residual stresses are caused by the large temperature gradients that develop during the DMLS manufacturing of Ti6Al4V parts. If these residual stresses are not relieved, the parts can possibly yield to these stresses and consequently deform when they are removed from the substrate. The SR and HT treatments applied to the tensile specimens were effective in relieving the residual stresses and decomposing the metastable martensitic microstructure of the AB specimens into a more ductile and stable lamella α+β microstructure displayed in Figure 87.

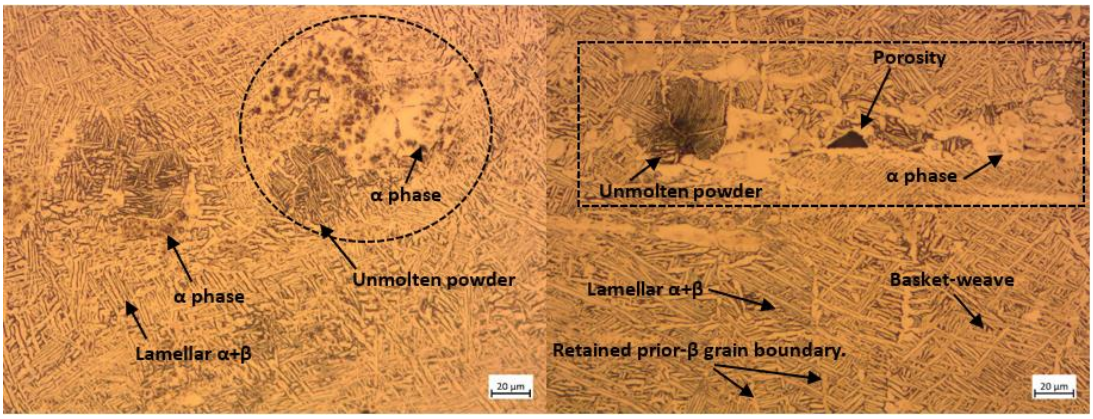

Figure 87. Microstructures obtained after stress-relieving at 650 °C for three hours and annealing at 940 °C for two hours for (a) PPS 3 and (b) PPS 4

The microstructure of the AB cubes produced from PB 1 (Figure 71) and PB 2 (Figure 86) have some similarities and differences. The AB microstructure from both the powder blends exhibited the metastable martensitic α phase typical of DMLS-produced Ti6Al4V parts. The microstructure of the cubes produced from PB 2 exhibited some unmolten powder particles and LOF pores. The unmolten powders may result in compositional inhomogeneity, while the LOF pores may negatively affect the mechanical properties of the alloy.

The heat treatment performed on the samples was able to decompose the brittle martensitic microstructure into a more ductile α+β microstructure, as shown in Figure 72 and Figure 87. Similar to the HT microstructures produced from PB 1, the HT microstructure produced from PB 2 exhibited a combination of lamellar α+β and equiaxed α phases. An analysis of the heat-treated microstructures of the parts produced from PB 2 revealed areas of localised chemical inhomogeneity (dotted lines) seen in Figure 87. It is evident that there was an incomplete fusion of the alloying elements in these areas as seemingly spherical unmolten powders surrounded by a rich α phase can be seen. This micro-inhomogeneity may consequently negatively affect the mechanical properties of the alloy.

The surface homogeneity of the 3D cubes produced from PB 2 is shown in Figure 88.

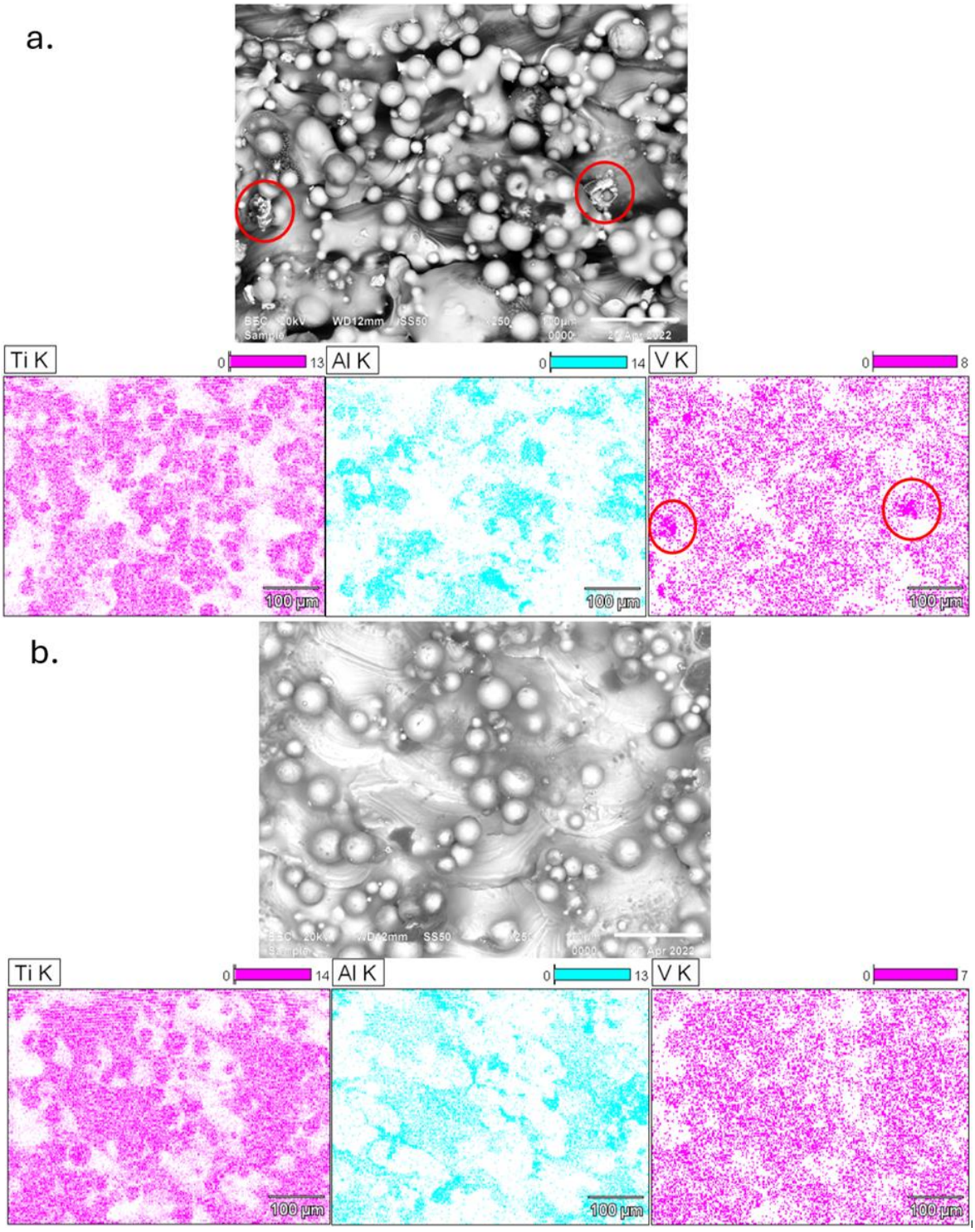

Figure 88. BEI image and Ti, Al and V K EDS maps of the morphology and homogeneity of the surfaces of AB cubes produced in (a) PPS 3 and (b) PPS 4.

Partially molten spherical Ti powders can be seen on the surface of the cube, which correspond with the Ti concentrations depicted in the Ti K EDS map. A partially molten V-powder particle (circled in red) can be seen on the SEM micrograph and V K EDS map in Figure 88(a). Unmolten Al powder particles cannot be clearly seen on the SEM micrographs, and this could be attributed to the low melting point of Al compared to Ti and V. The Al may have completely melted onto the surface of the cube instead of adhering as unmolten powder particles. In comparison with the surface morphology of the 3D cubes produced from PB 1, PB 2 resulted in a slightly higher degree of surface inhomogeneity due to the agglomeration of the different powder constituents to the surface of the cube. This inhomogeneity seen on the surfaces of the cubes warrants the need for surface post-processing on the in-situ alloyed parts.

The compositional results obtained from the ICP-OES analysis of the alloy produced from PB 2 are compared to the ASTM F2924-14 “Standard Specification for Additive Manufacturing Titanium-6 Aluminum-4 Vanadium with Powder Bed Fusion” [109] and tabulated in Table 16.

Table 16. ICP-OES composition determined for cubes produced with PPS 3 and PPS 4 compared with the ASTM F2924-14 specification [109]

Element	PPS 3	PPS 4	ASTM F2924–14
Ti	90.7	90.7	Remainder
Al	6.05	5.98	5.5–6.75 ± 0.4
V	3.19	3.3	3.5–4.5 ± 0.15
O	0.3	0.32	0.2 ± 0.02
N	0.012	0.01	0.05 ± 0.02
Fe	0.05	0.05	0.3 ± 0.1

The Al composition was within the specified range, while the V composition was below the specified compositional range for both process parameter sets. The composition of the interstitial elements, such as O and Fe, were above the specified compositional range for both PPS 3 and 4. The N composition was within the

specified compositional range for both PPS 3 and PPS 4. Since this in-situ alloying study involved the LPBF of three elemental powders, of which Al had the lowest melting point (660 °C) [171], it was anticipated that there would be a loss of the Al element due to evaporation. However, as the ICP-OES analysis results suggest, there was no Al lost due to evaporation, but there was a 20 and 17.5% loss of V for PPS 3 and 4, respectively. The V had the highest melting point (1929 °C) [171] out of the three powders; therefore, evaporation due to the heat radiated by the laser is unlikely. The analyses of the samples produced in this study assume that the powders were blended to the correct composition. Therefore, further investigation into the underlying cause of the loss of the V element is required.

The thermophysical properties of the powders are presented in Table 17 [171]–[174]. A review of these properties suggests that there should be a loss of the Al element instead of the V element. Al has the lowest melting point, which means that it would be approaching its boiling point (2470 °C) [171] by the time the Ti and V begin to melt. It has the highest thermal conductivity and heat capacity; therefore, it requires the least amount of heat energy to melt. It has the lowest molten density, meaning it is most likely to experience more laser radiation as it will tend to rise to the top of the molten pool. Having reviewed the thermophysical properties of the powders, the authors are unable to provide a valid scientific explanation behind this loss of V. They can argue that segregation of the powder blend might have taken place during the transportation, storage, and handling of the powder blend. Meyer [126] stated that the density of powder particles, amongst other factors, is the greatest contributing factor to segregation. From Table 17, it can be seen that the V powders had the greatest density, and they are more prone to experience a greater gravitational force acting upon them during transportation, storage and handling compared to Ti and Al, resulting in the V powders segregating to the bottom of the container. The powders were mixed in SU in early 2020 and received just at the beginning of the Covid-19 lockdown. They were only utilised for printing in different stages in 2021 and 2022. This suggests that the powder blend experienced a great deal of standing time during storage after being transported and handled, which may have led to its segregation. This segregation resulted in a higher V concentration towards the bottom of the container compared to the top of the container from where the powder was scooped for production. With reference to the high O_2 content in the compositional results,

another possible explanation behind this loss of V can be the evaporation of the V2O5 compound that forms during sintering, as explained in section 4.2.3 [133].

Table 17. The thermophysical properties of the employed metal powders [171], [173]**.**

Thermophysical property	Ti	Al	V
Melting point (°C)	1660	660	1929
Thermal conductivity (W/(m.K))	17	237	30.7
Heat capacity (J/kg.K)	520	900	490
Molten density (g/cm^3)	4.13	2.357	5.5
Solid density (g/cm^3)	4.5	2.7	6.11

Compared to the compositional results obtained from PB 1, PB 2 yielded a greater Al composition, while PB 1 yielded a greater V composition. The composition of the parts produced from PB 1 was generally much closer to the intended composition, with PPS 2 yielding parts that conform to the ASTM F2924-14 specifications. The higher Al content in PB 2 would suggest that these parts would exhibit a higher creep strength and weldability compared to the parts produced from PB 1. The lower V content in parts produced from PB 2 suggests that these parts would be less responsive to the standard Ti6Al4V heat treatment, which might result in parts with relatively high strength and low ductility. The compositional results for PB 2 (Table 16) can be confirmed by the microstructure seen in Figure 87. In the heat treatment of Ti6Al4V, the α and β phases compete for space during phase nucleation. Since Al is an α-phase stabiliser and V is a β-phase stabiliser, a slightly greater amount of α phase occupies the microstructure of the heat-treated Ti6Al4V [6].

The results obtained from the CT scans of the 3D cubes produced with PPS 3 and PPS 4 are displayed in Figure 89 and Figure 90, respectively. The cube produced from PPS 2 shows some randomly distributed gas pores ranging from 40 to 90 µm and some LOF pores ranging from 100 µm to 380 µm. The overall porosity distribution in the cube is shown in Figure 89(a), while Figure 89(b) and Figure 89(c) provide an example of the LOF and gas pores, respectively. By visual inspection, the cube is highly dense with only one detrimental LOF pore (Figure 89b) seen among some

randomly distributed gas pores. The volume analysis revealed that the cube was 99.9% dense. It is anticipated that parts produced from this PPS will yield excellent tensile strength values [74].

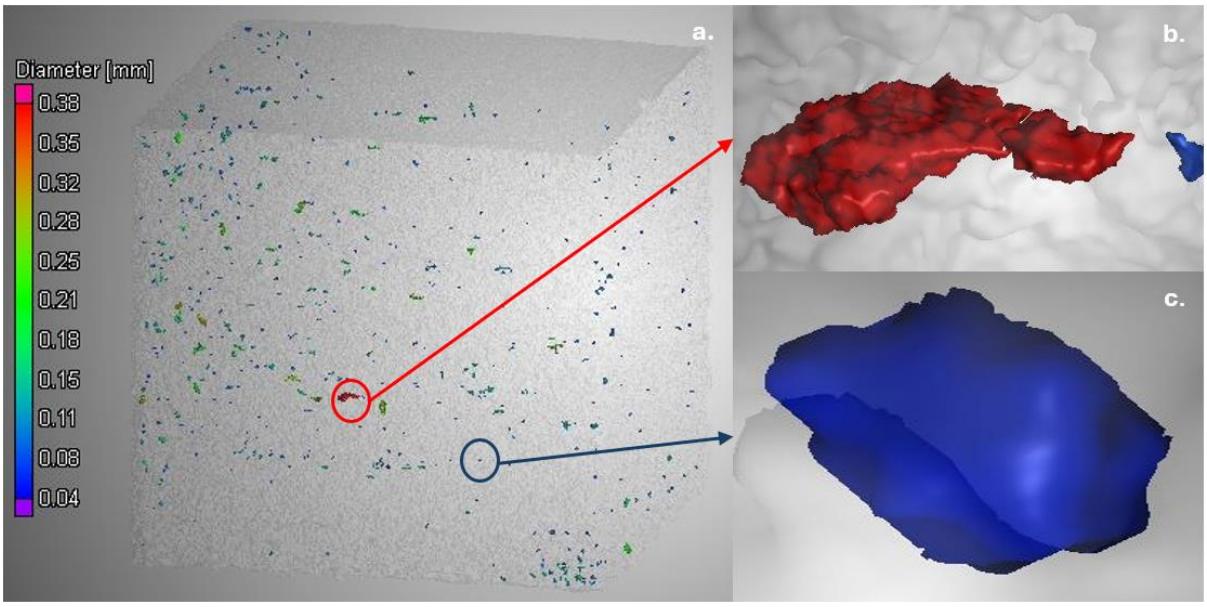

Figure 89. Micro CT scans of the AB Ti6Al4V cubes produced from PPS 3: (a) the overall porosity distribution within the cube, (b) lack-of-fusion pore, (c) gas pore. The colour codes of the pores displayed in (b) and (c) correspond to the diameter scale shown in (a)

The CT scan of the cube produced from PPS 4 (Figure 90) revealed that the cube had an excessive amount of gas pores with diameters ranging between 40 and 90 µm, some LOF pores with diameters ranging between 100 to 240 µm and one detrimental LOF pore (Figure 90c) with a diameter ranging between 250 and 380 µm. From Figure 90b, the gas pores appear to be layered in a direction perpendicular to the build direction. This is a direct indication that the LED used to produce this cube was excessive. The formation of these gas pores is due to the formation of the keyhole mode during single-track deposition, as explained in sections 4.2.1 and 4.3.2. A high LED results in the production of a single track with deep penetration that resembles a keyhole [47]. The molten pool within this keyhole contains entrapped air bubbles that collapse upon solidification, resulting in gas pores at the bottom of every single track as they are deposited during layer formation [40]. This provides an explanation as to why the gas pores appear to be in a straight line

perpendicular to the build direction. In small quantities, gas pores are usually considered harmless in DMLS-produced samples; however, in such high quantities, they may be detrimental to the mechanical properties of the part, especially if the tensile force applied to them is parallel to the build direction [74], [175]. From Figure 90(c), an area in the cube that contains the largest LOF pore amongst smaller-sized lack of fusion- and gas pores can be seen. This area can potentially act as a failure nucleation location because of the concentration of the different pores present in that area. Nonetheless, the volumetric analysis revealed that the cube had a density of 99.7%. It is anticipated that the samples produced from PPS 4 will also exhibit excellent tensile strength values despite the presence of the gas pores.

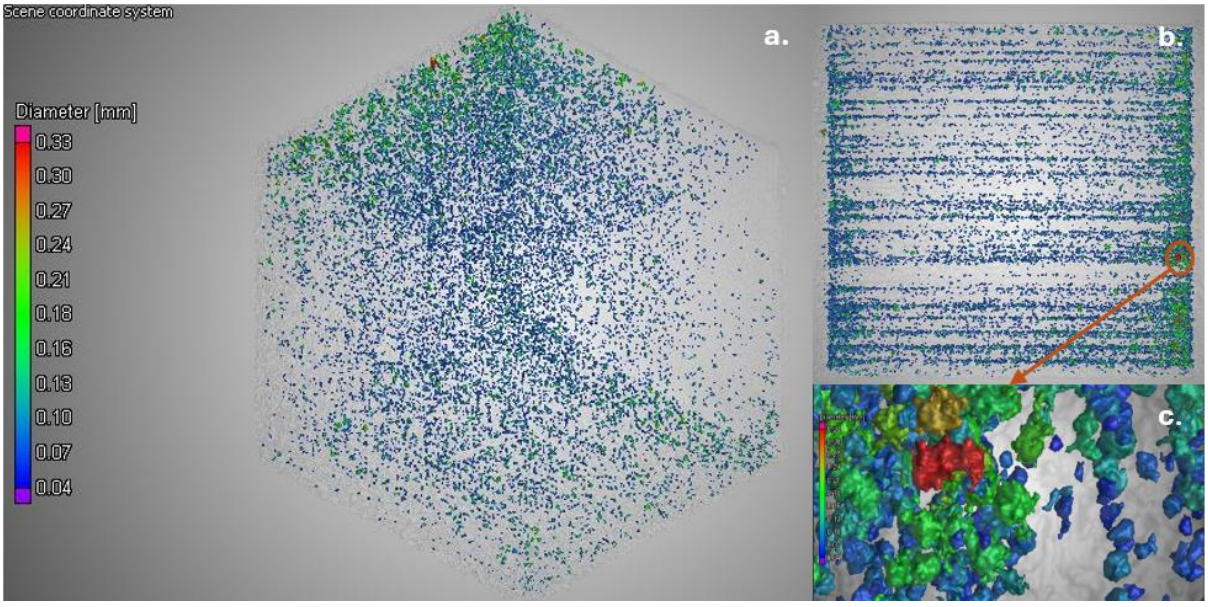

Figure 90. Micro CT scans of the AB Ti6Al4V cubes produced from PPS 4: (a) the overall porosity distribution within the cube, (b) the layered distribution of the pores within the cube, (c) the porosity at a particular section in the cube. The colour codes of the pores displayed in (b) and (c) correspond to the diameter scale shown in (a).

The elemental Ti powder used in the blending of PB 1 and PB 2 was highly spherical, while the Al-V MA used for PB 1 was characterised as “sharp irregular angular” [118]. The Al and V used for PB 2 were characterised as “irregular spherical” and “round irregular angular” [118], respectively. Ideally, the powders for the DMLS process should be spherical [163]. Due to the morphology of the constituents of PB 1, it was

anticipated that the cubes produced from PB 1 would be more porous than the cubes produced from PB 2 due to the misfit between the spherical Ti and the irregularly shaped Al-V MA in PB 1. However, the CT scanning results suggest that the cubes produced from PB 2 are more porous than the cubes produced from PB 1. The cube produced from PB 2 using PPS 3 was slightly more porous compared to the cubes produced from PB 1, while the cube produced from PB 2 using PPS 4 was more porous due to the excessive LED used to produce this cube. Despite the higher presence of pores in the cubes produced from PB 2, it is anticipated that the mechanical properties of these cubes may not be severely affected as the densities of the cubes are above 99%.

The mechanical properties obtained from the stress-relieved and annealed tensile test specimens and the properties specified in ASTM F2924-14 [109] are displayed in Table 18.

Table 18. The mechanical properties obtained from the heat-treated tensile specimens produced by PB 2 compared to the ASTM F2924–14 standard

Property	Process parameter set 3	Process parameter set 4	ASTM F2924–14
UTS (Mpa)	1112.45	1092.88	895
Ys (Mpa)	1024.1	1092.84	825
ε (%)	9.63	10.66	10
Area reduction (%)	21.24	20.82	15

The UTS, Ys and area reduction of the tensile specimens produced from PB 2 was greater than the UTS and Ys values specified in the ASTM F2924-14 standard and those reported for the specimens produced from PB 1 in Table 12. PPS 3 resulted in an ε value slightly less than the ε value specified in the ASTM F2924-14 standard, while PPS 4 resulted in an ε value that is slightly greater than the value specified in the standard. The tensile specimens produced from PB 1 exhibited a greater amount of ductility than the specimens produced from PB 2. In essence, the tensile specimens produced from PB 2 yielded greater strength values (UTS and Ys)

accompanied by a relatively low ductility than the tensile specimens produced from PB 1.

The SR and HT processes performed on the samples produced from PB 1 and PB 2 were performed using the same temperatures of 650 °C and 940 °C, respectively, although the composition of the specimens were not the same as shown in the compositional analyses in Table 11 and Table 16. During the compositional analysis, it was noted that the specimens produced from PB 1 exhibited low concentrations of the Al element, while the specimens produced from PB 2 had low concentrations of the V element compared to the compositional quantity required in the ASTM F2924-14 standard. In the heat treatment of the Ti6Al4V alloy, Al acts as an α-phase stabiliser for concentrations between 2–7 wt.% while V acts as a β-phase stabiliser for concentrations between 2–20 wt.% [6]. The concentration of the elements favouring the α or β phase determines the reactivity of the sample to HT processing [6]. With reference to the pseudo-binary Ti6Al4V phase diagram shown in Figure 27, it can be seen that the lower the Al composition, the higher the β-transus temperature, while an increase in the V composition tends to lower the β-transus temperature. The Ti6Al4V heat treatment relies on raising the temperature of the alloy to, or close to the β-transus temperature (± 995 °C) [84], [114] where 100% of the alloy material consists of the β-phase from which the grains are refined to a more ductile α+β phase during cooling to room temperature [84]. The quantity of beta stabilisers present determines the precise amount of beta that can be transformed from a certain temperature [6], [114]. The specimens produced from PB 1 had a greater concentration of the V element; therefore, they were more reactive to the HT. The samples produced from PB 2 contained a lesser amount of the V element; therefore, they were less reactive to the heat-treatment processes, resulting in an alloy with a high strength-to-density ratio compared to the ASTM F2924-14 standard and the samples produced by PB 1. The higher hardness values for samples produced from PB 2 can also be attributed to the higher O_2 content present in the samples.

SEM SEI images of the fracture surface of a machined tensile test specimen produced from PB 2 is displayed in Figure 91. The ductile crack initiation and shear lip areas can be seen in the overall SEI image of the fracture surface displayed in Figure 91(a). Quasi-cleavage facets that signpost brittle failure can be seen in Figure

91(b) and (c). The fracture surfaces of the tensile specimens produced from PB 2 exhibited a mixture of ductile and brittle failure. This type of failure can be attributed to the lack of response to the HT processes due to the lower concentration of the V element.

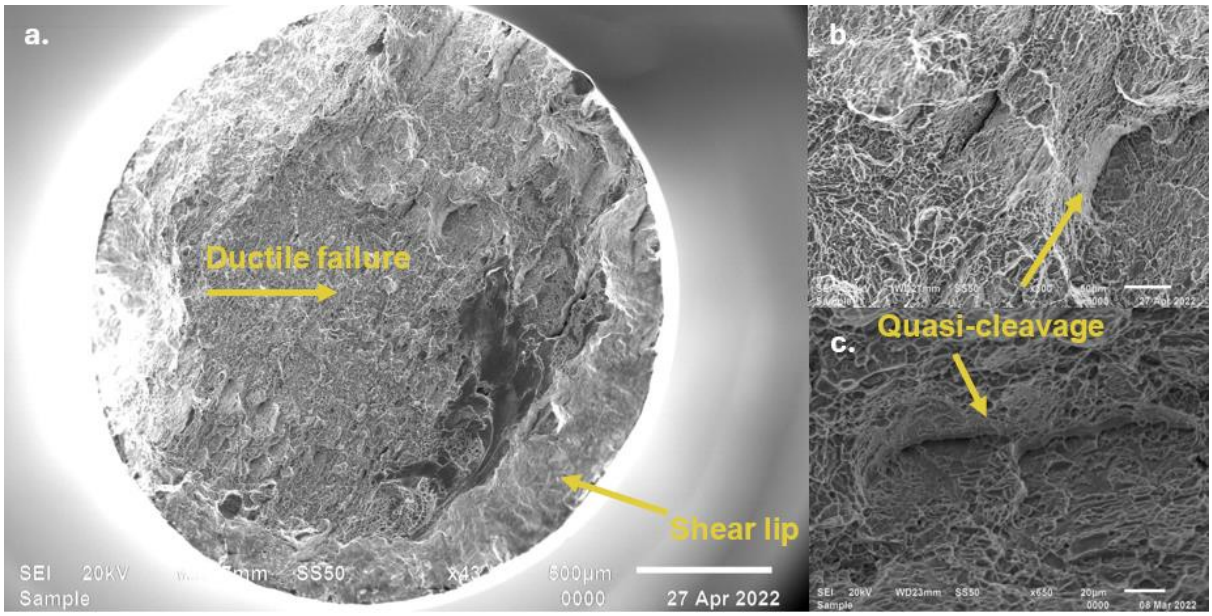

Figure 91. SEM SEI micrographs of the fracture surface of a tensile test specimen produced by PPS 3 using PB 2: (a) the overall fracture surface showing the shear lip and ductile failure in the central part of the fracture surface, (b) and (c) quasi-cleavage facets amongst dimple failure

4.4 Summary

This chapter focused on the analysis of the experimental samples produced according to the methodology outlined in Chapter 3 using two different powder blends, one being a powder blend consisting of CP Ti and an Al-V MA and the other a blend consisting purely of elemental powders of Ti, Al, and V. The analyses conducted ranged from single track and single- and double-layer analysis to the analysis of the produced 3D parts. The main aim of the single-track, single- and double-layer analyses was to determine a set of process parameters that could be used to produce high-quality 3D parts. The 3D-part analysis, on the other hand, focused on determining the integrity of the produced alloy through the analysis of the microstructure, mechanical properties and other factors that may have an impact on the integrity of the alloy.

The analyses conducted on the 3D samples produced from the two powder blends suggest that the parts produced from PB 1 yielded an alloy composition that conformed to the ASTM F2924-14 specification for a Ti6Al4V alloy produced from LPBF. Due to their composition, the parts produced from PB 1 were more responsive to the standard Ti6Al4V HT processes, thereby yielding an adequate strength-to-ductility ratio. The composition of the parts produced from PB 2, on the other hand, did not conform to the ASTM F2924-14 specification for LPBF Ti6Al4V parts. As a result, the parts produced from PB 2 were less responsive to the standard Ti6Al4V HT processes, thereby yielding a high strength-to-ductility ratio. In the following chapter, an overview of the overall outcome of the research and recommendations for future work are presented.

Chapter 5 Conclusions and future work

5.1 Introduction

The previous chapter analyzed the experimental samples produced and their resulting findings. This chapter presents the conclusions derived from the aim of the study, which was to evaluate the feasibility of using a powder blend consisting of a combination of elemental Ti and Al-V MA powders and a powder blend consisting of purely elemental Ti, Al, and V powders as feedstock for producing Ti6Al4V parts through the DMLS process. During the quest to fulfil the research aim, new ideas for possible research were generated and have been recommended for pursual in the recommendations for future work section.

5.2 Conclusions

The conclusions of this study can be drawn based on the extent to which the aims and objectives set out in Chapter 1 have been achieved.

1. **Determine the optimum process parameters that could be used to manufacture the Ti6Al4V alloy from BE powders through the DMLS process using the EOSINT M280 machine.**

   A hierarchal design approach, which has been commonly used in LPBF process parameter optimisation studies was used to determine the process parameters that could be used to produce 3D parts from the two powder blends employed in this study. Through this approach, single tracks were produced to identify different combinations of laser power and scanning speeds that produced single tracks which were continuous with the required cross-sectional characteristics at a given layer thickness. These combinations of laser power and scanning speed were then paired with a range of hatch distances to identify the best suitable hatch distance, which can be used to form defect-free layers. Once the correct hatch distance was found, a full set of process parameters that could be used to produce 3D parts was developed. Table 19 below describes the process parameters developed from this study. A total of four process parameter sets (two sets per powder blend) were developed.

Table 19. The process parameters developed in this study

Parameters	Laser power (W)	Scanning speed (m/s)	Hatch distance (µm)	Layer thickness (µm)
PPS 1 (PB 1)	100	0.6	80	60
PPS 2 (PB 1)	200	1.2	80	60
PPS 3 (PB 2)	200	0.6	80	60
PPS 4 (PB 2)	250	0.6	80	60

2. **Study the microstructure and mechanical properties of the Ti6Al4V samples manufactured from BE powders through the DMLS process using the EOSINT M280 machine.**

The AB microstructure of the specimens produced from both the powder blends used in this study was a binary (α+β) microstructure consisting of acicular martensitic α' laths contained within columnar prior-β grains. This microstructure is known to result in parts that have a high strength accompanied by a low ductility. For this reason, the specimens were heat-treated (annealing) to modify the microstructure and improve the mechanical properties. The resulting microstructure was a more ductile microstructure which consisted of a lamellar α+β phase with retained prior-β grains.

3. **Compare the mechanical properties and the microstructure of the Ti6Al4V alloy samples manufactured by the DMLS process using the EOSINT M280 machine with those from conventional wrought material methods and those obtained using PA powder.**

Tensile testing was conducted on the tensile test specimens to obtain an indication of the mechanical properties of the alloy produced from PB 1 and PB 2. The values of the UTS, Ys, ε and area reduction were found to be superior to those of the parts produced from the wrought and LPBF PA production routes.

5.3 Recommendations for future work

Based on the outcomes of this study, the following recommendations for future work can be made:

1. Spherical Al-V MA powders should be used and blended with spherical CP Ti powders to eliminate the occurrence of the LOF pores, thus improving the density and mechanical properties of the produced Ti6Al4V alloy.
2. To validate the argument that the segregation due to storage time influences the chemical composition of the powder blend, research based on the immediate use of powder blends post-blending is required. The parts produced from the recently blended powders can be analyzed to determine their chemical composition and heat-treated mechanical properties and then compared to the results obtained in this study.
3. To investigate the low- and high-temperature fatigue properties of the Ti6Al4V parts produced from the two Ti6Al4V powder blends.

References

[1] M. Christopher, Leyens ;Peters, “Titanium and Titanium Alloys,” in *Metal Matrix Composites*, 1st ed., C. Leyens and M. Peters, Eds. Weinheim,: Wiley-VCH Verlag GmbH & Co. KGaA, 2006, pp. 1–35.

[2] I. Yadroitsev, P. Krakhmalev, and I. Yadroitsava, “Hierarchical design principles of selective laser melting for high quality metallic objects,” *Addit. Manuf.*, vol. 7, no. 2015, pp. 45–56, 2015, doi: 10.1016/j.addma.2014.12.007.

[3] A. E. Patterson, P. D. Collopy, and S. L. Messimer, “State of the Art Survey of Additive Manufacturing Technologies, Methods, and Materials Manufacturing Constraints in Optimization and Design View project Mathematics and Design View project,” Huntsville, 2018. doi: 10.13140/RG.2.2.33894.47684/2.

[4] ASTM Internatioonal, “F2792-12a - Standard Terminology for Additive Manufacturing Technologies,” 2013. doi: 10.1520/F2792-12A.2.

[5] T. Wohlers and T. Gornet, “History of Additive Manufacturing,” Washington, DC, 2014. doi: 10.1017/CBO9781107415324.004.

[6] J. M. J. Donachie, *Titanium- A Technical Guide*, 2nd ed. Ohio: InTech, 2012.

[7] T. Hua, C. Jing, Z. Fengying, L. Xin, and H. Weidong, “Microstructure and Mechanical Properties of Laser Solid Formed Ti6Al4V from Blended Elemental Powders,” *Rare Met. Mater. Eng.*, vol. 38, no. 4, pp. 574–578, 2009, doi: 10.1016/S1875-5372(10)60028-8.

[8] M. Simonelli *et al.*, “A comparison of Ti-6Al-4V in-situ alloying in Selective Laser Melting using simply-mixed and satellited powder blend feedstocks,” *Mater. Charact.*, vol. 143, no. November 2017, pp. 118–126, 2018, doi: 10.1016/j.matchar.2018.05.039.

[9] O. M. Ivasishin, V. M. Anokhin, A. N. Demidik, and D. G. Sawakin, “Cost-effective blended elemental powder metallurgy of titanium alloys for transportation application,” *Key Eng. Mater.*, vol. 188, no. 2000, pp. 55–62,

2000, doi: 10.4028/www.scientific.net/KEM.188.55.

[10] D. de Beer *et al.*, “A South African Additive Manufacturing Strategy,” Pretoria, 2016. [Online]. Available: https://site.rapdasa.org/wp-content/uploads/2017/02/South-African-Additive-Manufacturing-Strategy.pdf.

[11] Z. Z. Fang *et al.*, “Powder metallurgy of titanium – past, present, and future,” *Int. Mater. Rev.*, vol. 63, no. 7, pp. 407–459, Oct. 2018, doi: 10.1080/09506608.2017.1366003.

[12] S. J. Oosthuizen and J. J. Swanepoel, “Development status of the CSIR-Ti Process,” in *IOP Conference Series: Materials Science and Engineering*, 2018, vol. 430, no. 1, doi: 10.1088/1757-899X/430/1/012008.

[13] J. Wroe, “Introduction to Additive Manufacturing Technology: A Guide for Designers and Engineers,” Shrewsbury, UK, 2015. [Online]. Available: www.epma.com/am.

[14] J. F. Sargent and R. X. Schwartz, “3D Printing: Overview, Impacts, and the Federal Role,” Washington, DC., 2019. [Online]. Available: https://crsreports.congress.gov.

[15] S. Ezeiruaku, “Review of Additive Manufacturing and Characterization of Additive Manufacturing Machine,” Master’s dissertation, Dept. Manu. Eng., Univ. of New Mexico, 2016.

[16] M. Shellabear and O. Nyrhilä, “DMLS – Development History and State of the Art,” in *Lane 2004*, 2004, pp. 1–12.

[17] M. K. Thompson *et al.*, “Design for Additive Manufacturing: Trends, opportunities, considerations, and constraints,” *CIRP Ann. - Manuf. Technol.*, vol. 65, no. 2, pp. 737–760 2016, doi: 10.1016/j.cirp.2016.05.004.

[18] W. E. Frazier, “Metal additive manufacturing: A review,” *J. Mater. Eng. Perform.*, vol. 23, no. 6, pp. 1917–1928, 2014, doi: 10.1007/s11665-014-0958-

z.

[19] M. Rafiee, R. D. Farahani, and D. Therriault, “Multi-Material 3D and 4D Printing: A Survey,” *Adv. Sci.*, vol. 7, no. 12, pp. 1–26, 2020, doi: 10.1002/advs.201902307.

[20] D. Herzog, V. Seyda, E. Wycisk, and C. Emmelmann, “Additive manufacturing of metals,” *Acta Mater.*, vol. 117, pp. 371–392, 2016, doi: 10.1016/j.actamat.2016.07.019.

[21] K. V. Wong and A. Hernandez, “A Review of Additive Manufacturing,” *ISRN Mech. Eng.*, vol. 2012, no. 1, pp. 1–10, 2012, doi: 10.5402/2012/208760.

[22] H. Mendoza, “Effects of a Binary Argon-Helium Shielding Gas Mixture on Ultra-Thin Features Produced by Laser-Powder Bed Fusion Additive Manufacturing Thesis,” Master’s degree, Dept. Manu. Eng., Ohio State Univ., 2021.

[23] J. P. Kruth, M. C. Leu, and T. Nakagawa, “Progress in additive manufacturing and rapid prototyping,” *CIRP Ann. - Manuf. Technol.*, vol. 47, no. 2, pp. 525–540, 1998, doi: 10.1016/S0007-8506(07)63240-5.

[24] I. Yadroitsava, J. Els, G. Booysen, and I. Yadroitsev, “Peculiarities of single track formation from TI6AI4V alloy at different laser power densities by selective laser melting,” *South African J. Ind. Eng.*, vol. 26, no. 3, pp. 86–95, 2015, doi: 10.7166/26-3-1185.

[25] J. Brezinová, R. Hudák, A. Guzanová, D. Draganovská, G. Ižaríková, and J. Koncz, “Direct metal laser sintering of Ti6Al4V for biomedical applications: Microstructure, corrosion properties, and mechanical treatment of implants,” *Metals (Basel).*, vol. 6, no. 7, 2016, doi: 10.3390/met6070171.

[26] I. Yadroitsev, I. Yadroitsava, P. Bertrand, and I. Smurov, “Factor analysis of selective laser melting process parameters and geometrical characteristics of synthesized single tracks,” *Rapid Prototyp. J.*, vol. 18, no. 3, pp. 201–208, 2012, doi: 10.1108/13552541211218117.

[27] I. Yadroitsev, "*Selective laser melting: Direct manufacturing of 3D-objects by selective laser melting of metal powders*", vol. 75, no. 3–4. Saarbucken: Lambert Academic Publishing, 2009.

[28] N. W. Makoana, H. Moller, H. Burger, M. Tlotleng, and I. Yadroitsev, “Evaluation of single tracks of 17-4PH steel manufactured at different power densities and scanning speeds by selective laser melting,” *South African J. Ind. Eng.*, vol. 27, no. 3 Special Issue, pp. 210–218, 2016, doi: 10.7166/27-3-1668.

[29] M. Saunders, “X marks the spot - find ideal process parameters for your metal AM parts,” *Renishaw*, vol. 44, no. 1, Gloucestershire, pp. 1–13, Apr. 2017.

[30] J. Reijonen, A. Revuelta, T. Riipinen, K. Ruusuvuori, and P. Puukko, “On the effect of shielding gas flow on porosity and melt pool geometry in laser powder bed fusion additive manufacturing,” *Addit. Manuf.*, vol. 32, no. 2020, pp. 1–10, 2020, doi: 10.1016/j.addma.2019.101030.

[31] J. J. S. Dilip *et al.*, “Influence of processing parameters on the evolution of melt pool, porosity, and microstructures in Ti-6Al-4V alloy parts fabricated by selective laser melting,” *Prog. Addit. Manuf.*, vol. 2, no. 3, pp. 157–167, 2017, doi: 10.1007/s40964-017-0030-2.

[32] Y. Xiang *et al.*, “Forming and defect analysis for single track scanning in selective laser melting of Ti6Al4V,” *Appl. Phys. A Mater. Sci. Process.*, vol. 124, no. 10, pp. 1–12, 2018, doi: 10.1007/s00339-018-2056-9.

[33] J. A. Muñiz-lerma, A. Nommeots-nomm, K. E. Waters, and M. Brochu, “A Comprehensive Approach to Powder Feedstock Characterization for Powder Bed Fusion Additive Manufacturing : A Case Study on AlSi7Mg,” *Materials (Basel).*, vol. 11, no. 2386, pp. 1–15, 2018, doi: 10.3390/ma11122386.

[34] W. Zhang, W. Hou, L. Deike, and C. Arnold, “Understanding the Rayleigh instability in humping phenomenon during laser powder bed fusion process,” *Int. J. Extrem. Manuf.*, vol. 4, no. 1, 2022, doi: 10.1088/2631-7990/ac466d.

[35] B. Zhang, Y. Li, and Q. Bai, “Defect Formation Mechanisms in Selective Laser Melting: A Review,” *Chinese J. Mech. Eng. (English Ed.*, vol. 30, no. 3, pp. 515–527, 2017, doi: 10.1007/s10033-017-0121-5.

[36] J. Patalas-Maliszewska, E. Feldshtein, O. Devojno, M. Śliwa, M. Kardapolava, and N. Lutsko, “Single tracks as a key factor in additive manufacturing technology-analysis of research trends and metal deposition behavior,” *Materials (Basel).*, vol. 13, no. 5, pp. 1–22, 2020, doi: 10.3390/ma13051115.

[37] A. Aversa *et al.*, “Single scan track analyses on aluminium based powders,” *J. Mater. Process. Tech.*, vol. 255, no. 1, pp. 17–25, 2018, doi: 10.1016/j.jmatprotec.2017.11.055.

[38] Q. Zhong, K. Wei, Z. Lu, X. Yue, T. Ouyang, and X. Zeng, “High power laser powder bed fusion of Inconel 718 alloy: Effect of laser focus shift on formability, microstructure and mechanical properties,” *J. Mater. Process. Technol.*, vol. 311, no. 8, pp. 1-17, 2023, doi: 10.1016/j.jmatprotec.2022.117824.

[39] T. C. Dzogbewu, I. Yadroitsev, P. Krakhmalev, I. Yadroitsava, and A. Du Plessis, “Optimal Process Parameters for In-Situ Alloyed Ti15Mo Structures by Laser Powder Bed Fusion,” in *Proceedings of the 28th Annual International Solid Freeform Fabrication Symposium*, 2017, no. 2014, pp. 75–96.

[40] R. Fabbro, “Melt pool and keyhole behaviour analysis for deep penetration laser welding,” *J. Phys. D. Appl. Phys.*, vol. 43, no. 44, pp. 1–13, 2011.

[41] E. B. Newby, “Investigation of in-situ alloying grade 23 Titanium with Copper by Selective Laser Melting Process for biomedical applications,” Master’s degree, Dept. Mech. Eng., Central University of Technology, 2018.

[42] F. Calignano, M. Galati, and L. Iuliano, “A metal powder bed fusion process in industry: Qualification considerations,” *Machines*, vol. 7, no. 4, 2019, doi: 10.3390/machines7040072.

[43] T. C. Dzogbewu, D. J. de Beer, and W. B. du Preez, “Laser Powder Bed Fusion

of Ti15Mo Fused Tracks and Layers," *Jom*, vol. 75, no. 2023, pp. 3183–3196, 2023, doi: 10.1007/s11837-023-05842-2.

[44] Z. Hu, H. Zhu, C. Zhang, H. Zhang, T. Qi, and X. Zeng, "Contact angle evolution during selective laser melting," *Mater. Des.*, vol. 139, no. 2018, pp. 304–313, 2018, doi: 10.1016/j.matdes.2017.11.002.

[45] H. Y. Erbil, "The debate on the dependence of apparent contact angles on drop contact area or three-phase contact line: A review," *Surf. Sci. Rep.*, vol. 69, no. 4, pp. 325–365, 2014, doi: 10.1016/j.surfrep.2014.09.001.

[46] M. I. Pech-Canul, R. N. Katz, M. Makhlouf, and S. Pickard, "The role of silicon in wetting and pressureless infiltration of SiCp preforms by aluminum alloys," *J. Mater. Sci.*, vol. 103, no. 3, pp. 239–248, 2002, doi: 10.1023/A:1004758305801.

[47] I. Yadroitsev, P. Krakhmalev, I. Yadroitsava, S. Johansson, and I. Smurov, "Energy input effect on morphology and microstructure of selective laser melting single track from metallic powder," *J. Mater. Process. Technol.*, vol. 213, no. 4, pp. 606–613, 2013, doi: 10.1016/j.jmatprotec.2012.11.014.

[48] J. Volpp, "Powder particle movement during Powder Bed Fusion," *Procedia Manuf.*, vol. 36, no. 2019, pp. 26–32, 2019, doi: 10.1016/j.promfg.2019.08.005.

[49] M. J. Matthews, G. Guss, S. A. Khairallah, A. M. Rubenchik, P. J. Depond, and W. E. King, "Denudation of metal powder layers in laser powder bed fusion processes," *Acta Mater.*, vol. 114, no. 2016, pp. 33–42, 2016, doi: 10.1016/j.actamat.2016.05.017.

[50] S. Traore *et al.*, "Influence of gas atmosphere (Ar or He) on the laser powder bed fusion of a Ni-based alloy," *J. Mater. Process. Technol.*, vol. 288, no. 2021, pp. 1–18, 2021.

[51] J. Volpp, "Powder particle movement during Powder Bed Fusion," *Procedia Manuf.*, vol. 36, pp. 26–32, 2019, doi: 10.1016/j.promfg.2019.08.005.

[52] J. Wang, R. Zhu, Y. Liu, and L. Zhang, “Understanding melt pool characteristics in laser powder bed fusion: An overview of single- and multi-track melt pools for process optimization,” *Adv. Powder Mater.*, vol. 2, no. 4, 2023, doi: 10.1016/j.apmate.2023.100137.

[53] I. Belot *et al.*, “A 3D additive manufacturing approach for the validation of a numerical wall-scale model of catalytic particulate filters,” *Chem. Eng. J.*, vol. 405, no. 2020, pp. 1-15, 2021, doi: 10.1016/j.cej.2020.126653.

[54] S. A. Khairallah, A. T. Anderson, A. Rubenchik, and W. E. King, “Laser powder-bed fusion additive manufacturing: Physics of complex melt flow and formation mechanisms of pores, spatter, and denudation zones,” *Acta Mater.*, vol. 108, no. 2016, pp. 36–45, 2016, doi: 10.1016/j.actamat.2016.02.014.

[55] M. A. Buhairi *et al.*, “Review on volumetric energy density: influence on morphology and mechanical properties of Ti6Al4V manufactured via laser powder bed fusion,” *Prog. Addit. Manuf.*, vol. 8, no. 2, pp. 265–283, 2023, doi: 10.1007/s40964-022-00328-0.

[56] G. Del Greco, “Correlation between the productivity and mechanical performance of AISI 316L parts produced via Laser powder bed fusion process,” Master’s degree, Dept. Mech. Eng, Politecnico Di Torino, 2020.

[57] S. Liu and Y. C. Shin, “Additive manufacturing of Ti6Al4V alloy: A review,” *Mater. Des.*, vol. 164, no. 2019, pp. 1–23, 2019, doi: 10.1016/j.matdes.2018.107552.

[58] Ó. Teixeira, F. G. Silva, L. P. Ferreira, and E. Atzeni, “A review of heat treatments on improving the quality and residual stresses of the Ti–6Al–4V parts produced by additive manufacturing,” *Metals (Basel).*, vol. 10, no. 8, pp. 1–24, 2020, doi: 10.3390/met10081006.

[59] N. Dumontet, B. Malard, and B. Viguier, “Study on the origins of residual stresses in Ti-6Al-4V processed by additive manufacturing,” *MATEC Web Conf.*, vol. 321, no. 2020, pp. 1–4, 2020, doi:

10.1051/matecconf/202032103001.

[60] T. Vilaro, C. Colin, and J. D. Bartout, “As-fabricated and heat-treated microstructures of the Ti-6Al-4V alloy processed by selective laser melting,” *Metall. Mater. Trans. A*, vol. 42, no. 10, pp. 3190–3199, 2011, doi: 10.1007/s11661-011-0731-y.

[61] T. H. Becker, M. Beck, and C. Scheffer, “Microstructure and mechanical properties of direct metal laser sintered Ti-6Al-4V,” *South African J. Ind. Eng.*, vol. 26, no. 1, pp. 1–10, 2015, doi: 10.7166/26-1-1022.

[62] H. Jia, H. Sun, and H. Wang, “Scanning strategy in selective laser melting (SLM): a review,” *Int. J. Adv. Manuf. Technol.*, vol. 113, no. 2021, pp. 2413–2435, 2021, doi: 10.1007/s00170-021-06810-3.

[63] H. Ali, H. Ghadbeigi, and K. Mumtaz, “Effect of scanning strategies on residual stress and mechanical properties of Selective Laser Melted Ti6Al4V,” *Mater. Sci. Eng. A*, vol. 712, no. 4, pp. 175–187, 2018, doi: 10.1016/j.msea.2017.11.103.

[64] W. Zhang, M. Tong, and N. M. Harrison, “Scanning strategies effect on temperature, residual stress and deformation by multi-laser beam powder bed fusion manufacturing,” *Addit. Manuf.*, vol. 36, no. 2020, pp. 1–13, 2020, doi: 10.1016/j.addma.2020.101507.

[65] Z. Zheng *et al.*, “Microstructure and anisotropic mechanical properties of selective laser melted Ti6Al4V alloy under different scanning strategies,” *Mater. Sci. Eng. A*, vol. 831, no. 2022, pp. 1–19, 2022, doi: 10.1016/j.msea.2021.142236.

[66] N. T. Aboulkhair, N. M. Everitt, I. Ashcroft, and C. Tuck, “Reducing porosity in AlSi10Mg parts processed by selective laser melting,” *Addit. Manuf.*, vol. 1, pp. 77–86, 2014, doi: 10.1016/j.addma.2014.08.001.

[67] Y. Lu, S. Wu, Y. Gan, T. Huang, C. Yang, and L. Junjie, “Study on the

microstructure , mechanical property and residual stress of SLM Inconel-718 alloy manufactured by differing island scanning strategy Optics & Laser Technology Study on the microstructure , mechanical property and residual stress of SLM Incone," *Opt. Laser Technol.*, vol. 75, no. 2015, pp. 1–11, 2017, doi: 10.1016/j.optlastec.2015.07.009.

[68] S. Chowdhury, N. Yadaiah, and C. Prakash, "Laser powder bed fusion : a state-of-the-art review of the technology , materials , properties & defects , and numerical modelling," *J. Mater. Res. Technol.*, vol. 20, no. 2022, pp. 2109–2172, 2022, doi: 10.1016/j.jmrt.2022.07.121.

[69] T. Bhardwaj and M. Shukla, "Effect of laser scanning strategies on texture, physical and mechanical properties of laser sintered maraging steel," *Mater. Sci. Eng. A*, vol. 734, no. June, pp. 102–109, 2018, doi: 10.1016/j.msea.2018.07.089.

[70] S. P. Karlapudy, T. Nancharaiah, and V. V. S. Rao, "Influence of different build orientation and laser scan strategies on surface quality, Mechanical and Material Characteristics of 18 Ni-300 maraging steel processed through DMLS," *Aust. J. Mech. Eng.*, vol. 21, no. 4, pp. 1381–1395, 2023, doi: 10.1080/14484846.2021.2007620.

[71] T. DebRoy *et al.*, "Additive manufacturing of metallic components – Process, structure and properties," *Prog. Mater. Sci.*, vol. 92, pp. 112–224, 2018, doi: 10.1016/j.pmatsci.2017.10.001.

[72] G. M. Ter Haar and T. H. Becker, "Selective laser melting produced Ti-6Al-4V: Post-process heat treatments to achieve superior tensile properties," *Materials (Basel).*, vol. 11, no. 1, 2018, doi: 10.3390/ma11010146.

[73] I. S. Grech, J. H. Sullivan, R. J. Lancaster, J. Plummer, and N. P. Lavery, "The optimisation of hot isostatic pressing treatments for enhanced mechanical and corrosion performance of stainless steel 316L produced by laser powder bed fusion," *Addit. Manuf.*, vol. 58, no. July, p. 103072, 2022, doi: 10.1016/j.addma.2022.103072.

[74] T. J. Jeon, T. W. Hwang, H. J. Yun, C. J. VanTyne, and Y. H. Moon, “Control of porosity in parts produced by a direct laser melting process,” *Appl. Sci.*, vol. 8, no. 12, 2018, doi: 10.3390/app8122573.

[75] A. Guzanová, G. Ižaríková, J. Brezinová, J. Živčák, D. Draganovská, and R. Hudák, “Influence of build orientation, heat treatment, and laser power on the hardness of Ti6Al4V manufactured using the DMLS process,” *Metals (Basel).*, vol. 7, no. 8, 2017, doi: 10.3390/met7080318.

[76] A. B. Spierings, N. Herres, G. Levy, and C. Buchs, “Influence of the particle size distribution on surface quality and mechanical properties in additive manufactured stainless steel parts,” pp. 397–406, 2010.

[77] A. Kinnear, T. Dzogbewu, P. Krakhmalev, I. Yadroitsava, and I. Yadroitsev, “Manufacturing, microstructure and mechanical properties of selective laser melted Ti6Al4V alloy,” *IOP Conf. Ser. Mater. Sci. Eng.*, vol. 266, no. 1, pp. 1–11, Nov. 2017, doi: 10.1088/1757-899X/266/1/012009.

[78] P. Vora, K. Mumtaz, I. Todd, and N. Hopkinson, “AlSi12 in-situ alloy formation and residual stress reduction using anchorless selective laser melting,” *Addit. Manuf.*, vol. 7, no. 2015 pp. 12–19, 2015, doi: 10.1016/j.addma.2015.06.003.

[79] S. Qin, S. Herzog, and A. Kaletsch, “Effects of Pressure on Microstructure and Residual Stresses during Hot Isostatic Pressing Post Treatment of AISI M50 Produced by Laser Powder-Bed Fusion,” *Metals (Basel),* vol. 11, no. 2021, pp 1-14, 2021.

[80] Z. Lv, H. Li, L Che, and S Chen “Effects of HIP Process Parameters on Microstructure and Mechanical Properties of Ti-6Al-4V Fabricated by SLM,” pp. 1–14, 2023.

[81] D. D. Phuong, L. Van Duong, N. Van Luan, and N. N. Anh, “Microstructure and Mechanical Properties of Ti6Al4V,” *Metals (Basel)*, vol. 9, no 1033, pp 1- 11, 2019.

[82] W. E. King, A. T. Anderson, R. M. Ferencz, and N. E. Hodge, “Laser powder bed fusion additive manufacturing of metals ; physics , computational , and materials challenges,” *Applied Physics Reviews*, vol. 2, no. 2020, pp 1-28 2015, doi: 10.1063/1.4937809.

[83] W. D. Callister Jr and D. G. Rethwisch, *Materials Science and Engineering*. 2003.

[84] B. Vrancken, L. Thijs, J. P. Kruth, and J. Van Humbeeck, “Heat treatment of Ti6Al4V produced by Selective Laser Melting: Microstructure and mechanical properties,” *J. Alloys Compd.*, vol. 541, no. 0, pp. 177–185, 2012, doi: 10.1016/j.jallcom.2012.07.022.

[85] Z. A. Mierzejewska, R. Hudák, and J. Sidun, “Mechanical properties and microstructure of DMLS Ti6Al4V alloy dedicated to biomedical applications,” *Materials (Basel).*, vol. 12, no. 1, pp. 1–17, 2019, doi: 10.3390/ma12010176.

[86] E. Cerri, and E Ghio, “On Strain-Hardening Behavior and Ductility of Laser Powder Bed-Fused Ti6Al4V Alloy Heat-Treated above and below the β - Transus,” *Materials (Basel).,* vol. 17, no. 3401, pp 1-18, 2024.

[87] K. Thejane, “Characterisation and monitoring of Ti-6Al-4V ELI powder used for the qualification of medical implants produced through additive manufacturing,” Master’s degree, Dept. Mech. Eng, Central University of Technology, 2018.

[88] U. S. G. Survey, *MINERAL COMMODITY SUMMARIES 2024*. 2024.

[89] M. Qian and F. H. Sam Froes, *Titanium powder metallurgy: Science, technology and applications*. Amsterdam: Elsevier, 2015.

[90] Y. Song, Z. Dou, T. Zhang, and Y. Liu, “Research Progress on the Extractive Metallurgy of Titanium and Its Alloys,” *Miner. Process. Extr. Metall. Rev.*, vol. 42, no. 8, pp. 1–17, 2020, doi: 10.1080/08827508.2020.1793145.

[91] M. El Khalloufi, O. Drevelle, and G. Soucy, “Titanium: An overview of resources

and production methods," *Minerals*, vol. 11, no. 12, 2021, doi: 10.3390/min11121425.

[92] Y. A. Song, "Experimental study of the basic process mechanism for direct selective laser sintering of low-melting metallic powder," *CIRP Ann. - Manuf. Technol.*, vol. 46, no. 1, pp. 127–130, 1997, doi: 10.1016/s0007-8506(07)60790-2.

[93] D. S. Van Vuuren, "A critical evaluation of processes to produce primary titanium," *J. South. African Inst. Min. Metall.*, vol. 109, no. 8, pp. 455–461, 2009.

[94] C. Doblin, D. Freeman, and M. Richards, "The TiRO^{TM} process for the continuous direct production of titanium powder," *Key Eng. Mater.*, vol. 551, no. 2013, pp. 37–43, 2013, doi: 10.4028/www.scientific.net/KEM.551.37.

[95] "Coogee Titanium. (2024) ." Developing and commercializing a revolutionary titanium alloy powder technology [Online]. Available: https://www.coogeetitanium.com.au/#process .

[96] C. G. McCracken, C. Motchenbacher, and D. P. Barbis, "Review of Titanium Powder Production Methods," *Int. J. Powder Metall.*, vol. 46, no. 5, pp. 19–26, 2010.

[97] D. S. Van Vuuren, S. J. Oosthuizen, and M. D. Heydenrych, "Titanium production via metallothermic reduction of TiCl 4 in molten salt," vol. 111, no. 2010, pp. 27–29, 2011.

[98] J. Simpson, "Titanium Today," Eastlake, Colorado, 2018.

[99] B. E. Carroll, T. A. Palmer, and A. M. Beese, "Anisotropic tensile behavior of Ti6Al4V components fabricated with directed energy deposition additive manufacturing," *Acta Mater.*, vol. 87, no. 2015, pp. 309–320, 2015, doi: 10.1016/j.actamat.2014.12.054.

[100] B. Vrancken, L. Thijs, J. P. Kruth, and J. Van Humbeeck, "Microstructure and

mechanical properties of a novel β titanium metallic composite by selective laser melting," *Acta Mater.*, vol. 68, no. 2014, pp. 150–158, 2014, doi: 10.1016/j.actamat.2014.01.018.

[101] K. K. Wong, H. C. Hsu, S. C. Wu, and W. F. Ho, "A Review: Design from Beta Titanium Alloys to Medium-Entropy Alloys for Biomedical Applications," *Materials (Basel).*, vol. 16, no. 21, 2023, doi: 10.3390/ma16217046.

[102] J. Han *et al.*, "Evolution on the Microstructure and Mechanical Properties of a New Multicomponent Near-Alpha Titanium Alloy after Rolling and Heat Treatments," *Metals (Basel).*, vol. 13, no. 7, 2023, doi: 10.3390/met13071231.

[103] R. P. Kolli and A. Devaraj, "A review of metastable beta titanium alloys," *Metals (Basel).*, vol. 8, no. 7, pp. 1–41, 2018, doi: 10.3390/met8070506.

[104] L. Y. Chen, Y. W. Cui, and L. C. Zhang, "Recent development in beta titanium alloys for biomedical applications," *Metals (Basel).*, vol. 10, no. 9, pp. 1–29, 2020, doi: 10.3390/met10091139.

[105] M. G. Moletsane, P. Krakhmalev, N. Kazantseva, A. du Plessis, I. Yadroitsava, and I. Yadroitsev, "Tensile properties and microstructure of direct metal laser-sintered Ti6Al4V (ELI) alloy," *South African J. Ind. Eng.*, vol. 27, no. 3 Special Issue, pp. 110–121, 2016, doi: 10.7166/27-3-1667.

[106] W. Weng, A. Biesiekierski, Y. Li, and C. Wen, "Effects of selected metallic and interstitial elements on the microstructure and mechanical properties of beta titanium alloys for orthopedic applications," *Materialia*, vol. 6, no. 3, 2019, doi: 10.1016/j.mtla.2019.100323.

[107] ASTM Internatioonal, "F3001-14 - Standard Specification for Additive Manufacturing Titanium-6 Aluminum-4 Vanadium ELI (Extra Low Interstitial) with Powder Bed Fusion.," 2021. doi: 10.1520/F3001-14.

[108] T. Becker, M. van Rooyen, and D. Dimitrov, "Heat treatment of Ti-6Al-4V produced by lasercusing," *South African J. Ind. Eng.*, vol. 26, no. 2, pp. 93–

103, 2015, doi: 10.7166/26-2-1161.

[109] ASTM Internatioonal, “F2924-14 - Standard Specification for Additive Manufacturing Titanium-6 Aluminum-4 Vanadium ELI (Extra Low Interstitial) with Powder Bed Fusion,” 2014. doi: 10.1520/F2924-14.2.

[110] E. Hancock, W. Smith, R. Wilson, and A. Bors, “An automated visual inspection system for the classification of the phases of Ti-6Al-4V Titanium alloy,” *Lect. Notes Comput. Sci. (including Subser. Lect. Notes Artif. Intell. Lect. Notes Bioinformatics)*, vol. 8048, no. 2, pp. 1-9, 2013, doi: 10.1007/978-3-642-40246-3.

[111] M. Wojtaszek, K. Zyguła, A. Łukaszek-Sołek, M. Jabłońska, R. Stanik, and M. Gude, “Forging of PM Ti–6Al–4V alloy at the temperature above β-transus and high strain rate: modeling and trials in industrial conditions,” *Arch. Civ. Mech. Eng.*, vol. 23, no. 2, pp. 1–21, 2023, doi: 10.1007/s43452-023-00636-4.

[112] S. Mohammad, J. Razavi, and F. Berto, “Directed Energy Deposition versus Wrought Ti-6Al-4V: A Comparison of Microstructure, Fatigue Behavior, and Notch Sensitivity,” *Adv. Eng. Mater.*, vol. 21, no. 8, pp. 1–16, 2019, doi: 10.1002/adem.201900220.

[113] A. M. Muiruri, M. Maringa, W. B. du Preez, and L. M. Masu, “Variation of impact toughness of AB DMLS TI6AL4V (ELI) specimens with temperature,” *South African J. Ind. Eng.*, vol. 29, no. 3 Special Edition, pp. 284–298, 2018, doi: 10.7166/29-3-2076.

[114] G. M. ter Haar, T. H. Becker, and D. C. Blaine, “Influence of heat treatments on the microstructure and tensile behaviour of selective laser melting-produced TI-6AL-4V parts,” *South African J. Ind. Eng.*, vol. 27, no. 3 Special Issue, pp. 174–183, 2016, doi: 10.7166/27-3-1663.

[115] R. K. Nalla, B. L. Boyce, J. P. Campbell, J. O. Peters, and R. O. Ritchie, “Influence of microstructure on high-cycle fatigue of Ti-6Al-4V: Bimodal vs. lamellar structures,” *Metall. Mater. Trans. A Phys. Metall. Mater. Sci.*, vol. 33,

no. 3, pp. 899–918, 2002, doi: 10.1007/s11661-002-0160-z.

[116] P. Lekoadi, M. Tlotleng, K. Annan, N. Maledi, and B. Masina, “Evaluation of heat treatment parameters on microstructure and hardness properties of high-speed selective laser melted ti6al4v,” *Metals (Basel).*, vol. 11, no. 2, pp. 1–15, 2021, doi: 10.3390/met11020255.

[117] S. P. Mates, S. D. Ridder, F. S. Biancaniello, and T. Zahrah, “Vacuum-assisted gas atomization of liquid metal,” *At. Sprays*, vol. 22, no. 7, pp. 581–601, 2012, doi: 10.1615/AtomizSpr.2012005918.

[118] B. S. Parker, “Blending of powders for in-situ alloying of Ti-6Al-4V laser powder bed fusion,” Master’s dissertation, Dept. of Mech. Eng., Stellenbosch University, 2021.

[119] J. J. Dunkley, “Metal powder atomisation methods for modern manufacturing,” *Johnson Matthey Technol. Rev.*, vol. 63, no. 3, pp. 226–232, 2019, doi: 10.1595/205651319X15583434137356.

[120] Material Technology Innovations. 2024. *Rotating Electrode Process* [Online]. Available at: http://www.mt-innov.com/index.php?ac=article&at=list&tid=16,” .

[121] P. Sun, Z. Z. Fang, Y. Zhang, and Y. Xia, “Review of the Methods for Production of Spherical Ti and Ti Alloy Powder,” *JOM*, vol. 69, no. 10, pp. 1853–1860, 2017, doi: 10.1007/s11837-017-2513-5.

[122] M. Qian, “Cold Compaction and Sintering of Titanium and its Alloys for Near-Net-Shape or Preform Fabrication,” *Int. J. Powder Metall.*, vol. 11 no. 2010, pp. 1-12.

[123] H. Moheb-Alizadeh and R. Handfield, “The impact of raw materials price volatility on cost of goods sold (COGS) for product manufacturing,” *IEEE Trans. Eng. Manag.*, vol. 65, no. 3, pp. 460–473, 2018, doi: 10.1109/TEM.2018.2796447.

[124] P. Avrampos, “A Simulation Study on Sieving as a Powder Deposition Method,” *Materials (Basel),* vol. 17, no. 3382, pp. 1-7, 2024.

[125] J. A. Hersey, “Ordered Mixing: A New Concept in Powder Mixing Practice J.A.,” *Powder Technol.*, vol. 11, no. 1, pp. 1–4, 1974.

[126] T. A. Meyer, “Novel Determination of Powder Mixing Qualities and Study of Dry Coated Particles,” *Powder Technol.*, vol. 11, no. 3, pp. 133–185, 2008, [Online]. Available: http://edoc.unibas.ch/791/1/DissB_8366.pdf.

[127] K. Thejane, S. Chikosha, and W. du Preez, “Characterisation and Monitoring of Ti6Al4V (ELI) Powder Used in Different Selective Laser Melting Systems,” *South African J. Ind. Eng.*, vol. 28, no. 3, pp. 161–171, Nov. 2017, doi: 10.7166/28-3-1853.

[128] M. Simonelli *et al.*, “The Influence of Iron in Minimizing the Microstructural Anisotropy of Ti-6Al-4V Produced by Laser Powder-Bed Fusion,” *Metallurgical and Materials Transactions A: Physical Metallurgy and Materials Science*, vol. 51, no. 5. pp. 2444–2459, 2020, doi: 10.1007/s11661-020-05692-6.

[129] M. Jia, D. Zhang, and B. Gabbitas, “Comparison of blended elemental (BE) and mechanical alloyed (MA) powder compact forging into Ti-6Al-4V rocker arms,” *Key Eng. Mater.*, vol. 520, no. 2, pp. 82–88, 2012, doi: 10.4028/www.scientific.net/KEM.520.82.

[130] J. D. Paramore, Z. Z. Fang, P. Sun, M. Koopman, R. Chandran, and M. Dunstan, “A powder metallurgy method for manufacturing Ti-6Al-4V with wrought-like microstructures and mechanical properties via hydrogen sintering and phase transformation (HSPT),” *Scr. Mater.*, vol. 107, no. 2015, pp. 103–106, 2015, doi: 10.1016/j.scriptamat.2015.05.032.

[131] S. Kalpakjian and S. R. Schmid, *Manufacturing Engineering and Technology*, 8th ed. Chicago: Pearson Educationn, 2013.

[132] A. Averardi, C. Cola, S. E. Zeltmann, and N. Gupta, “Effect of particle size

distribution on the packing of powder beds: A critical discussion relevant to additive manufacturing," *Mater. Today Commun.*, vol. 24, no. 2020, pp. 1–17, 2020, doi: 10.1016/j.mtcomm.2020.100964.

[133] Y. P. Dong *et al.*, "Cost-affordable Ti-6Al-4V for additive manufacturing: Powder modification, compositional modulation and laser in-situ alloying," *Addit. Manuf.*, vol. 37, no. 2020, pp. 1–9, 2021, doi: 10.1016/j.addma.2020.101699.

[134] H. L. Karlsson, N. V. Vallabani and X. Wang, "Health hazards of particles in additive manufacturing : a cross - disciplinary study on reactivity , toxicity and occupational exposure to two nickel - based alloys," *Sci. Rep.*, vol. 13, no 20846, pp. 1–15, 2023, doi: 10.1038/s41598-023-47884-1.

[135] J. I. Arrizubieta, O. Ukar, M. Ostolaza and A. Mugica, "Study of the environmental implications of using metal powder in Additive Manufacturing and its handling," *Metals (Basel),* vol. 10, no. 261, pp. 1-25, 2020.

[136] B. Reiplinger, Y. Plevachuk, and J. Brillo, "Surface tension of liquid Ti, V and their binary alloys measured by electromagnetic levitation," *J. Mater. Sci.*, vol. 57, no. 47, pp. 21828–21840, 2022, doi: 10.1007/s10853-022-07995-y.

[137] J. Els, "Optimal Process Parameters for Direct Metal Laser Sintering of Ti64 for Medical Implant Production," Master's degree, Dept. Mech. Eng., Central University of Technology, 2016.

[138] W. Wen-hao and L. Xin-yu, "Effect of linear energy density on pores of 316L stainless steel by selective laser melting Effect of linear energy density on pores of 316L stainless steel by selective laser melting," *IOP Conf. Ser.: Earth Environ. Sci.*, vol 223, no. 2019, pp. 1-5, 2019, doi: 10.1088/1755-1315/233/3/032008.

[139] A. Zenani, W. B. du Preez, T. C. Dzogbewu, and I. Yadroitsev, "Metal Additive Manufacturing of Ti6Al from Blended Elemental Powders," in *International Conference on Competitive Manufacturing*, 2019, pp. 181–187, [Online].

Available: http://jpaus.jaranboston.org/?eid=957714.

[140] “Designation: E8/E8M − 15a Standard Test Methods for Tension Testing of Metallic Materials 1,” doi: 10.1520/E0008_E0008M-15A.

[141] Engineering Purdue. 2024. *Surface roughness* [Online]. Available: https://engineering.purdue.edu/ME556/Documents/Surface%20Roughness.pdf.” .

[142] S. Rott, A. Ladewig, K. Friedberger, J. Casper, M. Full, and J. H. Schleifenbaum, “Surface roughness in laser powder bed fusion – Interdependency of surface orientation and laser incidence,” *Addit. Manuf.*, vol. 36, no. 5, p. 101437, 2020, doi: 10.1016/j.addma.2020.101437.

[143] H. Johnson, “Surface roughness,” *Edn*, vol. 46, no. 27. p. 30, 2001, doi: 10.1142/9781860945434_0014.

[144] Plastixportal. 2024. Testing of Plastic Materials Laboratory Services [Online]. Available: https://www.plastixportal.co.za/testing-of-plastics-materials-laboratory-services.html

[145] A. Mohammed and A. Abdullah, “Scanning Electron Microscopy (Sem): a Review,” *Proc. 2018 Int. Conf. Hydraul. Pneum.*, vol. 12 no. 11 , pp. 77–85, 2018.

[146] M. Z. Anna, “Effect of laser energy density, internal porosity and heat treatment on mechanical behavior of biomedical Ti6Al4V alloy obtained with DMLS technology,” *Materials (Basel).*, vol. 12, no. 14, 2019, doi: 10.3390/ma12142331.

[147] Stellenbosch University. 2024. Computed Tomogrpahy [Online]. Available:http://www.sun.ac.za/english/research-innovation/caf/equipment-database-ct- scanner.

[148] S. Liu, J. Liu, J. Chen, and X. Liu, “Influence of surface tension on the molten

pool morphology in laser melting," *Int. J. Therm. Sci.*, vol. 146, no. 8, pp. 106075, 2019, doi: 10.1016/j.ijthermalsci.2019.106075.

[149] E. B. Newby, D. Kouprianoff, and I. Yadroitsava, "In-situ alloying of TI6AL4V-x%CU structures by Direct Metal Laser Sintering," in *International Conference on Competitive Manufacturing*, 2019, pp. 180–189, [Online]. Available: http://jpaus.jaranboston.org/?eid=957714.

[150] P. Krakhmalev, I. Yadroitsev, I. Yadroitsava, and O. de Smidt, "Functionalization of biomedical Ti6Al4V via in situ alloying by Cu during laser powder bed fusion manufacturing," *Materials (Basel).*, vol. 10, no. 10, pp. 1–14, 2017, doi: 10.3390/ma10101154.

[151] M. T. Andani, R. Dehghani, M. R. Karamooz-Ravari, R. Mirzaeifar, and J. Ni, "Spatter formation in selective laser melting process using multi-laser technology," *Mater. Des.*, vol. 131, no. 2017, pp. 460–469, 2017, doi: 10.1016/j.matdes.2017.06.040.

[152] I. Yadroitsev, P. Bertrand, G. Antonenkova, S. Grigoriev, and I. Smurov, "Use of track/layer morphology to develop functional parts by selective laser melting," *J. Laser Appl.*, vol. 25, no. 5, pp. 1–8, Nov. 2013, doi: 10.2351/1.4811838.

[153] L. A. Ramosena, B. S. Parker, T. C. Dzogbewu, W. B. du Preez, and D. C. Blaine, "Optimum Process Parameters for DMLS In-Situ Alloying of A Ti-10(60Al40V) Powder Blend," in *Pre-Conference Seminar on Design and Additive Manufacturing of Titanium Parts*, 2019, pp. 78–93.

[154] I. Yadroitsev and I. Smurov, "Surface morphology in selective laser melting of metal powders," *Phys. Procedia*, vol. 12, no. 2011, pp. 264–270, 2011, doi: 10.1016/j.phpro.2011.03.034.

[155] A. Majeed, A. Ahmed, A. Salam, and M. Z. Sheikh, "Surface quality improvement by parameters analysis, optimization and heat treatment of AlSi10Mg parts manufactured by SLM additive manufacturing," *Int. J. Light.*

Mater. Manuf., vol. 2, no. 4, pp. 288–295, 2019, doi: 10.1016/j.ijlmm.2019.08.001.

[156] C. L. Chan, J. Mazumder, and M. M. Chen, “Three-dimensional axisymmetric model for convection in laser-melted pools,” *Mater. Sci. Technol. (United Kingdom)*, vol. 3, no. 4, pp. 306–311, 1987, doi: 10.1179/mst.1987.3.4.306.

[157] F. I. Azam, A. Rani, K. Altaf, T. V. Rao, and H. A. Zaharin, “An In-Depth Review on Direct Additive Manufacturing of Metals,” *IOP Conf. Ser. Mater. Sci. Eng.*, vol. 328, no. 1, 2018, doi: 10.1088/1757-899X/328/1/012005.

[158] J. Yang, H. Yu, J. Yin, M. Gao, Z. Wang, and X. Zeng, “Formation and control of martensite in Ti-6Al-4V alloy produced by selective laser melting,” *Mater. Des.*, vol. 108, pp. 308–318, 2016, doi: 10.1016/j.matdes.2016.06.117.

[159] Z. Feng, Y. Yang, Z. Xu, and Q. Shi, “Effect of martensitic transformation on elastic modulus anisotropy of Ti-6Al-4V alloy,” *Mater. Res.*, vol. 21, no. 4, Jun. 2018, doi: 10.1590/1980-5373-mr-2018-0197.

[160] I. Polozov, V. Sufiiarov, and A. Popovich, “Investigation of Ti-6Al-4V alloy in situ manufactured using selective laser melting from elemental powder mixture,” *Solid State Phenom.*, vol. 299, no. 22, pp. 646–651, 2020, doi: 10.4028/www.scientific.net/SSP.299.646.

[161] L. Bolzoni, P. G. Esteban, E. M. Ruiz-Navas, and E. Gordo, “Mechanical behaviour of pressed and sintered titanium alloys obtained from master alloy addition powders,” *J. Mech. Behav. Biomed. Mater.*, vol. 15, no. 2012, pp. 33–45, Nov. 2012, doi: 10.1016/j.jmbbm.2012.05.019.

[162] P. Hartunian and M. Eshraghi, “Effect of build orientation on the microstructure and mechanical properties of selective laser-melted Ti-6Al-4V Alloy,” *J. Manuf. Mater. Process.*, vol. 2, no. 4, 2018, doi: 10.3390/jmmp2040069.

[163] N. Nkhasi, W. B. du Preez, and H. Bisset, “Plasma Spheroidisation of Irregular Ti6Al4V Powder for Powder Bed Fusion,” *Metals (Basel).*, vol. 11, no. 1763,

pp. 1–13, Jun. 2021, doi: 10.31399/asm.hb.v24.a0006563.

[164] I. Yadroitsava, I. Yadroitsev, I. Van Zyl, and D. Kouprianoff, “Laser Based Powder Bed Fusion of Pure Platinum,” in *International Conference on Competitive Manufacturing Laser*, Stellenbosch, 2019, pp. 6–11.

[165] J. Volpp, “Behavior of powder particles on melt pool surfaces,” *Int. J. Adv. Manuf. Technol.*, vol. 102, no. 5–8, pp. 2201–2210, 2019, doi: 10.1007/s00170-018-03261-1.

[166] D. Gu *et al.*, “Densification behavior, microstructure evolution, and wear performance of selective laser melting processed commercially pure titanium,” *Acta Mater.*, vol. 60, no. 9, pp. 3849–3860, 2012, doi: 10.1016/j.actamat.2012.04.006.

[167] V. Andronov, J. Šimota, L. Beránek, J. Blažek, and F. Rušar, “Optimization of process parameters for additively produced tool steel 1.2709 with a layer thickness of 100 µm,” *Materials (Basel).*, vol. 14, no. 11, 2021, doi: 10.3390/ma14112852.

[168] I. Yadroitsev, P. Krakhmalev, and I. Yadroitsava, “Selective laser melting of Ti6Al4V alloy for biomedical applications: Temperature monitoring and microstructural evolution,” *J. Alloys Compd.*, vol. 583, no. 2014, pp. 404–409, 2014, doi: 10.1016/j.jallcom.2013.08.183.

[169] I. Yadroitsev, P. Bertrand, and I. Smurov, “Parametric analysis of the selective laser melting process,” *Appl. Surf. Sci.*, vol. 253, no. 19, pp. 8064–8069, 2007, doi: 10.1016/j.apsusc.2007.02.088.

[170] O. M. Ivasishin, D. G. Savvakin, F. H. Froes, V. S. Mokson, and K. A. Bondareva, “Synthesis of the Ti-6Al-4V alloy having low residual porosity by powder metallurgy method,” *Powder Metall. Met. Ceram.*, vol. 41, no. 7–8, pp. 54–64, 2002.

[171] AZO Materials, “Grade 23 Ti-6Al-4V ELI (UNS R56401) data sheet.”

http://www.azom.com (accessed Jan. 14, 2019).

[172] P. D. Desai, “Thermodynamic properties of vanadium,” *Int. J. Thermophys.*, vol. 7, no. 1, pp. 213–228, 1986, doi: 10.1007/BF00503812.

[173] Engineering Toolbox, “Thermo-physical properties of Vanadium.” www.engineeringtoolbox.com (accessed Jul. 17, 2023).

[174] Material Properties, “Vanadium: Boiling, Melting Point, Thermal Conductivity & Expansion.” https://material-properties.org/vanadium-thermal-properties-melting-point-thermal-conductivity-expansion/ (accessed Jul. 18, 2023).

[175] I. Hatos, I. Fekete, D. Harangozó, and H. Hargitai, “Influence of local porosity on the mechanical properties of direct metal laser-sintered 1.2709 alloy,” *Stroj. Vestnik/Journal Mech. Eng.*, vol. 66, no. 6, pp. 351–357, 2020, doi: 10.5545/sv-jme.2020.6573.